MODELLING THE INFLUENCE OF CHARACTERISTICS, ORIENTATION AND POSITIONING OF BEACH BUILDINGS ON AIRFLOW AND AEOLIAN SEDIMENT TRANSPORT PATTERNS IN THE SURROUNDING AREA

Paran Pourteimouri

Graduation Committee:

prof. dr. ir. H. F. J. M. Koopman	University of Twente, chairman and secretary
prof. dr. S. J. M. H. Hulscher	University of Twente, supervisor
prof. dr. K. M. Wijnberg	University of Twente, supervisor
dr. ir. G. H. P. Campmans	University of Twente, co-supervisor
prof. dr. ir. H. Askes	University of Twente
dr. ir. J. J. Van Der Werf	University of Twente
prof. dr. A. Kroon	University of Copenhagen
prof. dr. ir. B. J. E. Blocken	KU Leuven
dr. ir. S. de Vries	Delft University of Technology

The presented research is carried out at the Water Engineering and Management (WEM) group, Civil Engineering, Faculty of Engineering Technology, University of Twente, The Netherlands.

This research is part of the ShoreScape project, which is a joint research project of the University of Twente and Delft University of Technology. This research was funded by Netherlands Organisation for Scientific Research (NWO) and co-funded by Rijkswaterstaat (RWS) and Hoogheemraadschap Hollands Noorderkwartier (HHNK).

ISBN (print) : 978-90-365-5634-7
ISBN (digital) : 978-90-365-5635-4
DOI : 10.3990/1.9789036556354
Cover design : Paran Pourteimouri
Printed by : Ipskamp Printing

MODELLING THE INFLUENCE OF CHARACTERISTICS, ORIENTATION AND POSITIONING OF BEACH BUILDINGS ON AIRFLOW AND AEOLIAN SEDIMENT TRANSPORT PATTERNS IN THE SURROUNDING AREA

DISSERTATION

to obtain

the degree of doctor at the University of Twente,

on the authority of the Rector Magnificus,

prof. dr. ir. A. Veldkamp,

on account of the decision of the Doctorate Board

to be publicly defended

on Friday 26 May 2023 at 14.45 hours

by

Paran Pourteimouri

born on the 31st of October, 1991
in Babol, Iran

This dissertation has been approved by:

prof. dr. S. J. M. H. Hulscher	University of Twente, supervisor
prof. dr. K. M. Wijnberg	University of Twente, supervisor
dr. ir. G. H. P. Campmans	University of Twente, co-supervisor

If we knew what we were doing, it would
not be called research, would it?

Albert Einstein

I dedicate this thesis to the courageous students who have been forced to flee their homelands due to invasions by domestic or foreign enemies. These students demonstrate remarkable bravery, leaving behind everything they know and love in pursuit of calmness and safety in foreign lands. As I reflect on their experiences, I am humbled by their sacrifices and the daily challenges they endure. Having experienced the hardships of migration myself, I know how a simple family dinner could become an unattainable dream, when they are thousands of miles away from their loved ones.

We are happy, free, confused, and lonely at the same time! Hope for a world where justice and human rights are fully respected, and where everyone can live in peace and dignity.

CONTENTS

PREFACE

IT went by in the blink of an eye! It feels like just yesterday when I found myself lost in the complex corridors of Horst, searching for Suzanne's office where we had our first meeting with Kathelijne and Geert also. It was only one day after my arrival in the Netherlands, and yet the memory is as vivid as ever.

Like many others, my PhD journey was filled with many ups and downs, from stressful and high-pressure moments, challenges of COVID and quarantine, working from home, traveling for conferences, waiting for journals to dealing with emotional challenges such as homesickness and tragic news from my homeland country, Iran. Despite these obstacles, I am proud that I never gave up. However, I could not have succeeded without the continuous support of many people, whom I would like to take this opportunity to thank.

I would like to thank my first promotor Suzanne Hulscher, second promotor Kathelijne Wijnberg and daily supervisor Geert Campmans. Suzanne, thank you for your constant support and trust in me. Our monthly meetings were the highlights of my PhD, giving me the energy to keep going. Your encouragement and feedback gave me the motivation and confidence I needed to tackle the next month's challenges. Despite your busy schedule, I appreciate how you always made time to promptly respond to my emails, review my works, and calm my worries. Thank you for being an exceptional promotor. Kathelijne, I would like to express my gratitude for your invaluable guidance and contributions to this research. We definitely missed you during the year and a half you were away. However, upon your return, we were grateful to have your feedback on the third paper and the writing of the thesis. Your insightful comments, critical and practical thinking, and the many fruitful discussions we had during my PhD played an instrumental role in the success of this project. Geert, I am grateful for your guidance and support throughout my PhD. You were not only a great supervisor but also a good friend. Your feedback on my research papers and progress was always valuable and appreciated. I particularly enjoyed your unique perspective on the physical aspects of my work, and our meetings were always nice brainstorming sessions for me. Your trust in my research made me more confident and motivated to tackle the challenges that came my way. Thank you also for always being there for me when I needed to chat or get some friendly advice.

I would like to express my sincere gratitude to the secretaries Anke, Dominique, and Dorette for their continuous support and contribution to a pleasant working environment. Furthermore, I would like to express my gratitude to my colleagues from the Water Engineering and Management Group, with whom I shared many good memories. Daan, thank you for all the amazing discussions we had over the ShoreScape project. I will never forget our first field work day, where the weather was stormy and sand everywhere, from my hair and shoes to my bag and even my sweater pockets! (That's why research on aeolian sediment transport is important. 😊) It was quite different from my initial expectations of a PhD program, which involved a well-organized office environment where I would be dressed in professional attire and working on a computer while sipping my coffee. 😊 You and Geert were so kind, patient, and supportive, especially in those early days when I was still finding my footing. Thanks to your help and guidance, the subsequent field work days went much more smoothly, and I learned so much through the experience.

I would like to express my sincere gratitude to my office mates Anouk, Xiuqi, and Lieke for making the work environment a fun and enjoyable place. Our conversations about culture differences, language, and personal experiences, shared laughs, deep discussions, and support during challenging times made our little corner of the department a warm and welcoming space. I am especially grateful to Xiuqi for her delicious home-made treats, Weique for her invaluable insights over her PhD experience, and Elham and Parisa for their wonderful company during lunch breaks.

I would like to express my sincere gratitude to my family - my parents, brother, and sister - for their constant love and support throughout my PhD. Despite living in three different countries and facing time zone differences, I always felt their constant presence and encouragement. Mom and dad, I wonder how you managed to keep track of my important deadlines and ensure that I took care of myself. I am blessed to have such a loving and supportive family.

A big, warm thank you to my husband, Mahyar. Darling, we have come a long way together, from our long-distance relationship to the challenges posed by COVID restrictions that prevented you from joining me in the Netherlands and starting your study program. Despite these obstacles, we persevered and were finally able to become partners and get married in the second year of my PhD. For almost a year, we worked together in a home office, and thanks to online meetings, I had the opportunity to learn a little bit about your major in business management. During our walks on the beach, you also shared your insights on erosion and deposition around buildings. I cannot thank you enough for your continuous support, your willingness to lend a helping hand, and your motivation during times when I felt frustrated. And let's not forget the delicious dishes you cooked for me, which resulted in

a 15-kilogram weight gain in just one year! 😊 Together, we have created beautiful memories that will last a lifetime. Thank you, Mahyar, for being my partner in every sense of the word.

SUMMARY

COASTAL zones worldwide have always been attractive to human populations because of their rich resources and recreational values. This leads to an increasing number of buildings at the beach-dune interface, such as hotels, restaurants, vacation houses and pavilions. Buildings at the beach locally change the airflow patterns in their surrounding area depending on their size, shape, orientation and positioning with respect to neighbouring buildings. These building-induced changes in wind flow field (speed and direction) alter aeolian sediment transport which, in turn, influence the morphologic patterns around buildings. For beach buildings placed in front of the dunes, these forced bedforms around buildings could negatively affect the dunes by e.g. trapping the sediments upwind of the buildings slowing down the dune growth. Furthermore, a large amount of sediment deposition or an intense erosion around buildings cause malfunctions in buildings. Coastal managers are responsible to define regulations for the design and placement of buildings at the beach. Understanding the airflow patterns and aeolian sediment transport around buildings could help to gain most benefits from buildings at the beach in regard to steering more sediments to dunes, or minimising their negative influence on dunes growth. To achieve this aim, a numerical model is developed using OpenFOAM and the influence of several parameters on airflow structures, aeolian sediment transport patterns and bedform development around buildings is investigated.

In Chapter 2, we quantified the influence of systematic changes in building dimensions, i.e. length, width and height, on airflow patterns around buildings. The divergence of the cubed horizontal wind velocity field was used as a proxy for wind-driven erosion and deposition patterns. Our results showed that the near-bed airflow structures and sediment transport patterns around buildings depend most on the building width perpendicular to the wind direction, whereas they are least dependent on the building length parallel to the wind direction. Numerical simulations showed sediment deposition at a small distance upwind of the buildings and two deposition tails starting from some distance away from the lateral sides of the building to downstream of the buildings. Strong scour occurs around the upwind corners of the buildings. However, less intense eroding regions have been found directly in front of the upwind face of the building and close to the lateral faces of the building. Our findings showed that relations exist between building characteristics and the size

and intensity of the erosion-deposition patterns around buildings.

In Chapter 3, the influence of buildings positioning at the beach relative to the neighbouring buildings, and the orientation of a row of buildings with respect to the wind direction on near-bed airflow patterns was examined. The wind-induced bed shear stress calculated via the OpenFOAM model was used in Bagnold's equation to evaluate the sediment transport flux around buildings. The Exner formulation was used to estimate the initial rate of changes in bed elevation around buildings. Results showed that there is a critical gap size between adjacent buildings of $2w$, where w is each building width, beyond which the airflow and sediment transport patterns form almost independently from patterns developed around neighbouring buildings. In that case, the adjacent buildings have minor impacts on each other and the resulting airflow and sediment transport patterns can be considered as more individual patterns around buildings. We also found that the orientation of buildings at the beach relative to the incident wind direction plays a key role in the formation of the vortices developing around buildings as well as their location, size and orientation. The characteristics of these vortices determine the sediment transport patterns in the vicinity of buildings. Next, the average sediment transport rates across along-shore lines downstream of the buildings were computed to gain insight on the influence of buildings on duneward sediment transport.

Finally, in Chapter 4, we investigated the influence of buildings placed on poles, and examined the systematic changes in building pole height on horizontal and vertical wind field as well as the sediment transport patterns. The Exner equation together with Bagnold's sediment transport formula were used to determine the initial bed level changes. Next, we developed a new model that couples the airflow model, OpenFOAM, with an existing sediment transport model, AeoLiS, to model the morphological evolution of the wind-driven bed patterns. The results of the average sediment transport rates across along-shore lines revealed that depending on pole height, the elevated buildings could both steer more sediments to the dunes hence enhancing the dunes growth, or they could block sediments upwind of the buildings therefore slow down the dunes growth.

Overall, this thesis provided new insights in the influence of buildings on potential duneward sediment transport and bed level changes in their surrounding. The guidance provided by this research could help coastal managers to decide on regulations in regards to beach buildings.

SAMENVATTING

KUSTGEBIEDEN over de hele wereld zijn altijd aantrekkelijk geweest voor de menselijke bevolking vanwege hun rijke hulpbronnen en recreatieve waarden. Dit leidt tot een toenemend aantal bebouwing op het strand en nabij het duin, zoals hotels, restaurants, vakantiehuizen en strandpaviljoens. Gebouwen op het strand veranderen plaatselijk de luchtstroompatronen, afhankelijk van hun grootte, vorm, oriëntatie en positionering ten opzichte van naburige gebouwen. Deze door gebouwen veroorzaakte veranderingen in het windstroomveld (snelheid en richting) veranderen het transport van eolisch sediment, wat op zijn beurt de morfologische patronen rond gebouwen beïnvloedt. Voor strandgebouwen die voor de duinen zijn geplaatst, kunnen deze geforceerde bodemvormen rond gebouwen de duinen negatief beïnvloeden door bijvoorbeeld het sediment bovenwinds vast te houden, wat er toe leid dat duingroei vertraagd. Verder kunnen grote hoeveelheden sediment depositie of een sterke erosie rond gebouwen voor problemen voor de gebouwen zorgen. Kustbeheerders zijn verantwoordelijk voor het opstellen van voorschriften voor het ontwerp en de plaatsing van gebouwen op het strand. Inzicht in de luchtstroompatronen en eolisch sedimenttransport rond gebouwen kan helpen om de meeste voordelen te halen uit gebouwen op het strand met betrekking tot het sturen van sediment naar duinen, of het minimaliseren van hun negatieve invloed op duinengroei. Om dit doel te bereiken, werd een numeriek model ontwikkeld met behulp van OpenFOAM en werd de invloed van verschillende parameters op luchtstroomstructuren, eolische sedimenttransportpatronen en bodemvorming rond gebouwen onderzocht.

In Hoofdstuk 2 kwantificeerden we de invloed van systematische veranderingen in de afmetingen van gebouwen, d.w.z. lengte, breedte en hoogte, op luchtstroompatronen rond gebouwen. De divergentie van het tot de derde macht verheven horizontale windsnelheidsveld werd gebruikt als een proxy voor door de wind aangedreven erosie- en sedimentatiepatronen. Onze resultaten toonden aan dat de luchtstroomstructuren nabij het bed en de sedimenttransportpatronen rond gebouwen het meest afhankelijk zijn van de gebouwbreedte loodrecht op de windrichting, terwijl ze het minst afhankelijk zijn van de gebouwlengte evenwijdig aan de windrichting. Numerieke simulaties toonden sedimentafzetting op kleine afstand bovenwinds van de gebouwen en twee afzettingstaarten vanaf enige afstand van de zijkanten van het gebouw tot stroomafwaarts van de gebouwen. Sterke erosie

treed op rond de bovenwindse hoeken van de gebouwen. Er zijn echter minder intense eroderende gebieden gevonden direct voor de bovenwindse zijde van het gebouw en dicht bij de zijvlakken van het gebouw. Onze bevindingen toonden aan dat er relaties bestaan tussen gebouwkenmerken en de grootte en intensiteit van de erosie-depositiepatronen rond gebouwen.

In Hoofdstuk 3 werd de invloed onderzocht van de positie van gebouwen op het strand ten opzichte van aangrenzende gebouwen, en de oriëntatie van een rij gebouwen ten opzichte van de windrichting op luchtstromingspatronen nabij het bed. De door de wind geïnduceerde bodemschuifspanning berekend via het OpenFOAM-model werd gebruikt in de vergelijking van Bagnold om de sedimenttransportflux rond gebouwen te evalueren. De Exnerformulering werd gebruikt om de initiële snelheid van veranderingen in bodemhoogte rond gebouwen te schatten. De resultaten toonden aan dat er een kritische opening is tussen aangrenzende gebouwen van 2w, waarbij w de breedte van elk gebouw is, waarboven de luchtstroom- en sedimenttransportpatronen zich vrijwel onafhankelijk vormen van patronen rond aangrenzende gebouwen. Daarom hebben de aangrenzende gebouwen weinig invloed op elkaar en kunnen de resulterende luchtstroom- en sedimenttransportpatronen worden beschouwd als meer individuele patronen rond individuele gebouwen. We ontdekten ook dat de oriëntatie van gebouwen op het strand ten opzichte van de invallende windrichting een sleutelrol speelt bij de vorming van de wervels die rond gebouwen ontstaan, evenals hun locatie, grootte en oriëntatie. De eigenschappen van deze wervels bepalen de sedimenttransportpatronen in de buurt van gebouwen. Vervolgens werden de gemiddelde sedimenttransportsnelheden over langs de kust lopende lijnen stroomafwaarts van de gebouwen berekend om inzicht te krijgen in de invloed van gebouwen op het duinwaarts sedimenttransport.

Ten slotte hebben we in hoofdstuk 4 de invloed onderzocht van gebouwen die op palen zijn geplaatst, en hebben we de systematische veranderingen in de hoogte van de palen van gebouwen op horizontaal en verticaal windveld onderzocht, evenals de transportpatronen van sediment. De Exner-vergelijking samen met de sedimenttransportflux van Bagnold werden gebruikt om de initiële bodemniveauveranderingen te bepalen. Vervolgens hebben we een nieuw model ontwikkeld dat het luchtstroommodel, OpenFOAM, koppelt aan een bestaand sedimenttransportmodel, AeoLiS, om de morfologische evolutie van de door de wind aangedreven bodempatronen te modelleren. De resultaten van de gemiddelde sedimenttransportsnelheden langs de kustlijn toonden aan dat, afhankelijk van de paalhoogte, de verhoogde gebouwen meer sediment naar de duinen konden sturen en zo de groei van de duinen versterken, of ze konden sediment bovenwinds van de gebouwen blokkeren en daardoor de duingroei afremmen.

Al met al heeft dit proefschrift nieuwe inzichten opgeleverd over de invloed van gebouwen op potentieel duinwaarts sedimenttransport en bodemveranderingen in hun omgeving. De richtlijnen die dit onderzoek biedt, zou kustbeheerders kunnen helpen bij het nemen van beslissingen over regelgeving met betrekking tot strandgebouwen.

1

Introduction

1

1.1. BACKGROUND

SANDY beaches have always been attractive to people worldwide. The immense value of beaches for recreation, tourism and economy has led to an increased number of buildings at the beach-dune interface. These buildings include hotels, restaurants, vacation houses, surfing clubs, lifeguard towers and pavilions (Figure 1.1). Coastal dunes are mobile and dynamic sand systems, providing natural flood defence for the hinterland. Although coastal sand dunes are vulnerable landforms, they can restore themselves under natural processes. The eroded sand from the most seaward dune of a coastal dune field is generally redistributed onto either the foredunes or beach, at the location where the dune erosion occurred or further along the coast (Van der Meulen and Salman, 1996). Where there is sufficiently strong wind, the available sand budget at the beach could be carried to the dune foot and even further landward along the stoss slope of the dune, over and behind the dune slip face. This leads to the dune growth and/or dune migration. The presence of any obstructions, i.e. buildings, in front of the dunes might disrupt the natural processes in a way that the sand dunes could not be naturally restored, thereby also losing their value as the natural barrier against storm surges. On the other hand, some believe that these hard structures in front of the dunes could enhance aeolian sediment transport and help the growth of dunes (Nordstrom et al., 2000).

Buildings at the beach influence the local near-bed wind field depending on their characteristics (such as dimension, geometry, pole height and construction material) as well as positioning (relative to the dominant wind direction, neighbouring buildings and the dune foot) (Jackson and Nordstrom, 2011) at the beach. These building-induced near-bed flow patterns determine the aeolian sediment transport, therefore bed morphology around buildings (Nordstrom and McCluskey, 1985; Nordstrom, 2000; Walker and Nickling, 2002). The resultant erosion and deposition patterns around buildings might become problematic for beach buildings owners (Figure 1.2). Furthermore, sand trapping by buildings could hamper sediments from moving to the dunes.

An understanding of the airflow and wind-blown sediment transport patterns around buildings on sandy substrate, e.g. beaches, can be used by coastal managers to create guidance for designing beach buildings. Adhering to this guidance helps to enhance nature-based flood defence solutions by enhancing sediment transport to the dunes or limiting potentially negative impacts of buildings on dunes. In addition, they help beach buildings owners to increase the lifetime of their properties without the frequent need for sand removal measures.

This thesis studies the effects of buildings at the beach on their sandy surroundings. Our

(a) (b)

(c) (d)

Figure 1.1: Examples of buildings at the beach-dune interface; a) beach restaurants and pavilions at Scheveningen beach, the Netherlands, b) a row of vacation houses in front of the dune at Katwijk beach, the Netherlands, c) two rows of small-size beach huts with staggered configuration at Katwijk beach, the Netherlands, and d) a row of vacation houses on poles in front of the dune at Kijkduin beach, the Netherlands.

field observations on Dutch coast showed that buildings at the beach are mainly placed in a group of cuboid buildings with/without poles next to each other. The size of the buildings ranges between small-size beach huts that are used as storage or for changing clothes, and larger buildings such as vacation houses or restaurants. The beach buildings are placed close to each other or far apart from each other depending on the empty space at the beach. Besides, the wind direction and speed constantly vary at the beach. Therefore, this study is focused on the examination of the influence of parameters such as building dimensions, pole height, gap size between neighbouring buildings and the wind direction relative to the row of buildings on airflow and wind-driven sediment transport patterns. Examination is done by developing numerical models and performing a wide range of systematic simulations.

(a) (b)

(c) (d)

Figure 1.2: Wind-induced morphological patterns around buildings at the beach; a) a restaurant that was buried in sand at Noordwijk beach, the Netherlands, b) a row of small-size beach huts with erosion around at Katwijk beach, the Netherlands, c and d) a container with erosion in front and sand accumulation behind just a few days after it was placed at Noordwijk beach, the Netherlands.

1.2. AIRFLOW PATTERNS OF PERPENDICULAR WIND AROUND A CUBIC BUILDING

BUILDINGS influence the airflow in their surroundings. The wind approaching a cubic building is deflected from the so-called stagnation point downwards to the ground, around the sides and over the top of the building (see Figure 1.3a). The deflected flow to the ground moves away from the windward face of the building, and in the reverse direction compared to the dominant wind direction. The reverse flow undercuts the approaching wind, detaches it from the bed surface and forms a standing horseshoe-shape vortex wrapping around the windward and lateral faces of the building. These corner flows encompass high wind speeds (Peterka et al., 1985; Blocken et al., 2011; Oke et al., 2017). As the upward and sideward flows encounter sharp windward edges of the building, they detach from the building surface and form small circulation regions tangential to the building top and sides. These separation bubbles are characterised by highly turbulent and low-speed flow. The detached flows may reattach onto the building surface, depending on the turbulence

of the approaching wind and the dimensions of the building (Blocken et al., 2011). A large separation bubble, so-called cavity region, forms in the low-pressure region immediately behind the building containing vertically and horizontally oriented recirculating vortices (near-wake region). The separated flow re-attaches the bed surface, and the re-attachment line remarks the outer boundary of the cavity region (see Figure 1.3b). Beyond this line, the wind flow resumes parallel to the dominant wind direction, but the decelerated flow remains for longer distances downstream of the building (wake region). Figure 1.3 shows the mean airflow patterns around an isolated cubic building.

The flow mechanisms explained above form around an isolated cubic building under perpendicular wind direction. However, the influence of actual beach buildings scale, row of closely-spaced buildings at the beach, and elevated buildings on poles under perpendicular or oblique wind directions is not fully known yet.

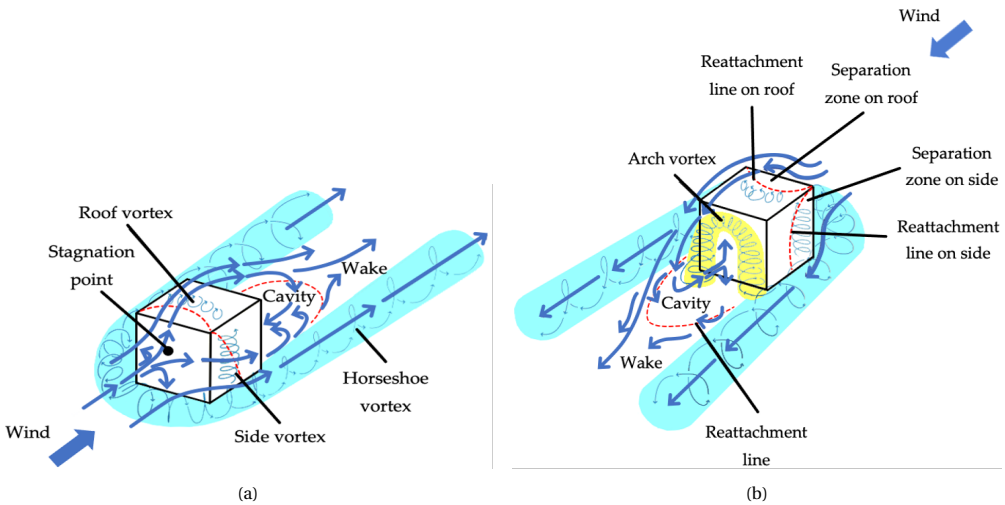

Figure 1.3: Schematic illustration of the mean wind flow patterns in the vicinity of a single sharp-edged building, with two different a) windward and b) leeward views (modified from Oke et al., 2017).

1.3. AEOLIAN SEDIMENT TRANSPORT PATTERNS AROUND A BUILDING

THE aeolian sediment transport and resultant erosion-deposition patterns developing around a building on an erodible sandy bed result from bed shear stress perturbations due to the presence of building-induced coherent vortex structures. The windward horseshoe shape vortex causes strong scour in front of the windward face, around the windward corners and along the sides of the building (Iversen et al., 1990; Iversen et al., 1991; McKenna

Neuman et al., 2013; Tominaga et al., 2018). Deposition occurs at a small distance in front of the building. This is induced by the reverse vortex flow upwind of the building that carries sands opposite to the incident wind direction and deposits them at the decelerated flow region where the reverse and approaching flows meet. Besides, the sand particles carried by the upwind flow are deposited when flow decelerates close to the building. The upwind deposition gradually grows, and eventually forms the so-called echo dune shape (Bagnold, 1941; Tsoar, 1983; Cooke et al., 1993; Qian et al., 2011; Jackson and Nordstrom, 2011). In addition, deposition occurs along the lateral faces of the building and continues somewhat downstream, approximately following the shape of the horseshoe vortex shown in Figure 1.3 (Poppema et al., 2021). Sand accumulation, known as sand shadow/tail, forms in the sheltered area (wind shadow) in the lee of the building (Livingstone and Warren, 1996; Luo et al., 2012; McKenna Neuman et al., 2013). The approximate erosion and deposition patterns around an isolated cubic building with perpendicular wind direction, based on the field experiments conducted by Poppema (2022), is shown in Figure 1.4. A series of one-day experiments were performed at a wide moist sandy beach to address the extent to which scaled buildings influence the wind-induced sediment transport at the beach. Also, he tested how the erosion and deposition patterns around buildings depend on the building characteristics and positioning relative to neighbouring buildings and dominant wind direction at the beach.

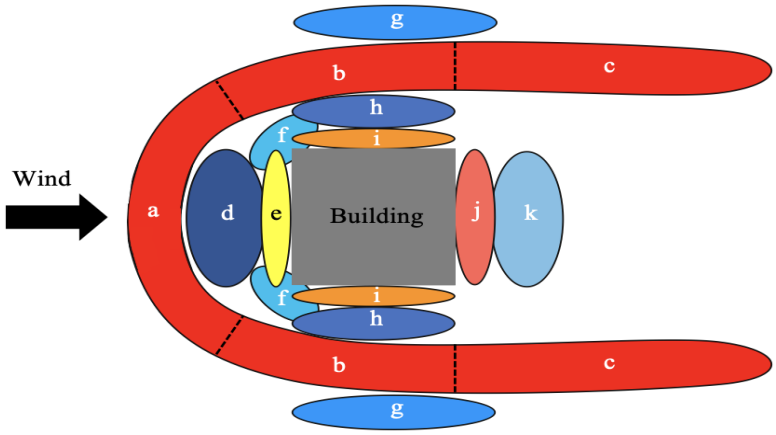

Figure 1.4: Schematization of observed topographic patterns around a cubic building, with a) upwind horse-shoe deposition, b) lateral horse-shoe deposition, c) downwind horse-shoe deposition, d) upwind inner erosion, e) upwind inner deposition, f) upwind corner inner erosion, g) lateral outer erosion, h) lateral inner erosion, i) lateral inner deposition, j) downwind inner deposition, and k) downwind inner erosion (modified from Poppema, 2022). Overall, the red, orange, and yellow shaded colours show the locations where the deposition occur, while the blue shaded colours show the eroding regions.

1.4. MODELLING OF THE AEOLIAN PROCESSES

EXISTING approaches to investigate the aeolian processes around buildings/obstacles mainly consist of wind-tunnel experiments, field measurements and numerical models. The possible advantages and disadvantages of each method are explained in this section.

Wind-tunnel experiments have been widely used to examine the airflow and sediment transport patterns around obstacles (similar to buildings) with various shapes, sizes, orientations and group configurations (Hunt et al., 1978; Fackrell, 1984; Beranek, 1984; Peterka et al., 1985; Iversen et al., 1990; Iversen et al., 1991; Meinders et al., 1999; Sutton and McKenna Neuman, 2008; Luo et al., 2012; Luo et al., 2014; Tominaga et al., 2018; Zhao et al., 2022). In-situ flow and sediment transport measurements are used to quantify the phenomena that occur in reality (Richards and Hoxey, 2012; Smyth and Hesp, 2015; Poppema, 2022; Vos et al., 2022). Unlike field tests, the wind-tunnel experiments allow for precise control of the experiment conditions such as time of the experiment, duration, weather conditions (e.g. snowfall, rainfall) and boundary conditions (e.g. wind speed, wind direction). However, the limited wind-tunnel size may lead to scaling issues, and the restrictions of the experimental materials make it difficult to accurately replicate the in-situ conditions (e.g. surface roughness, geometric details of the buildings or model domain). Furthermore, the measurement instruments in both wind-tunnel experiments and field tests might interfere with the flow field, affecting the measurements (Zhao et al., 2022).

Computational fluid dynamics (CFD) is a numerical technique to solve the flow field. In CFD, the Navier-Stokes equations are often used that consist of the conservation of mass and momentum. CFD is becoming increasingly popular in aeolian research due to the benefits it provides and the growing number of open-source CFD solvers. CFD provides a number of advantages compared to wind-tunnel experiments and field measurements. The main advantage of CFD is the high resolution at which the airflow properties can be solved. However, it is noteworthy that the more detailed computations, the more computationally expensive simulations. In addition, CFD is relatively easy to adapt to various applications using different geometries and boundary conditions. Unlike wind-tunnel experiments, CFD simulations can reproduce the exact wind conditions and scales of the buildings and domain similar to those of in the field. This allows for straightforward validations with field measurements of airflow and avoids potential scaling issues.

Many CFD software packages have been developed that are able to model airflow around buildings or aeolian bedforms. The non-commercial softwares are Stanford University Unstructured (SU2), OVERFLOW, OpenFOAM, Mfix and Nek5000, while commercial softwares

consist of COMSOL, Aerosoft, ANSYS and BARRACUDA VR. Among these softwares, the OpenFOAM has been widely used to model aeolian processes (Jackson et al., 2011; Joubert et al., 2012; D. W. Jackson et al., 2013; Smyth and Hesp, 2015; Bruno and Fransos, 2015; Enteria, 2016; M. F. King et al., 2017; Okafor et al., 2018). OpenFOAM is an open-source CFD software that is able to use the Reynolds-averaged Navier-Stokes (RANS) equations to solve the flow motion. In RANS equations, the instantaneous quantities are decomposed into their mean (time-averaged) and fluctuating components. The open access to OpenFOAM source codes allows users to contribute various useful libraries and toolboxes, that could be used in public to develop customized models for different applications. OpenFOAM can be used for a wide range of applications making use of existing compressible or incompressible flow solvers under steady or unsteady (transient) flow conditions. In addition, it can solve single phase or multiphase flows using one to three dimensional models.

1.5. KNOWLEDGE GAPS

THE wind flow around either an isolated obstacle/building or a group of obstacles/buildings has been well addressed in previous literature (Hunt et al., 1978; Fackrell, 1984; Beranek, 1984; Peterka et al., 1985; Martinuzzi and Tropea, 1993; Coceal et al., 2006; Shah and Ferziger, 1997; Lakehal and Rodi, 1997; Chou and Chao, 2000; Iaccarino et al., 2003; Gao and Chow, 2005; Yakhot et al., 2006). The influence of obstacles/buildings on their sandy environment has been of interest in many studies. The local morphologic patterns that develop around an isolated obstacle has been studied by Bagnold (1941), Pye and Tsoar (2008), McKenna Neuman and Bédard (2015) and Tominaga et al. (2018). Wind-tunnel and field experiments have been conducted to investigate the extent to which these erosion and deposition patterns around obstacles/scaled buildings depend on buildings geometry and dimensions (Iversen et al., 1990; Iversen et al., 1991; McKenna Neuman et al., 2013 and Poppema et al., 2021). Sutton and McKenna Neuman (2008), Luo et al. (2012), Luo et al. (2014), Luo et al. (2016) and Poppema et al. (2022b) evaluated the impacts of obstacles/scaled buildings positioning on a sandy substrate, using wind-tunnel tests or field measurements at the beach. In their impact of obstacles/buildings studies, these researchers focused mainly on orientation relative to the dominant wind direction and the distance from neighbouring obstacles/scaled buildings.

The aforementioned studies used mainly small-scale obstacles that are appropriate for wind-tunnel experiments. Poppema (2022) used larger-sized models in the field that could be considered as scaled models of vacation houses at the beach. However, in his studies only three models were placed at the beach to examine the aeolian morphologic changes around buildings with different sizes and configurations at the beach. On actual beaches with

plenty of space in the along-shore direction, periodically repeated rows of beach houses are placed in front of the dunes (e.g. Figure 1.1d). In addition, due to experimental constraints he could only assess a limited range of changes for the parameter under consideration. Besides the limitations discussed above, the flow field was not studied in his work. Luo et al. (2012) and Luo et al. (2014) respectively, studied the impacts of systematic changes in the orientation of a single cuboid obstacle and the gap size between two adjacent cuboid obstacles on bedform development. In their studies they used wind field measurements as a proxy to predict wind-blown sediment transport and thereby the resultant local erosion and deposition mechanisms. Only in their latest study, Luo et al. (2016), they conducted experiments with erodible substrate where they reported implications on the formation of sand shadows in the lee of a single building or the sand drift that develops behind the gap between two neighbouring buildings. The experimental study by Poppema et al. (2022b) examined the influence of orientation and gap size over the whole area around a group of buildings. Furthermore, first attempts to model wind-blown morphologic changes around buildings over longer time period, i.e. years to decades, were presented in a recent study by Poppema et al. (2022a). They used the results obtained from field measurements to develop the cellular automaton model rules for erosion and deposition patterns around buildings. Although the model rules used in their study provide insight in how buildings change the bed evolution in their surroundings over longer time period in relation to specific time-varying wind conditions, they cannot provide detailed quantitative sediment transport fluxes around buildings.

Therefore, examining the aeolian sediment transport around periodic rows of full-scale beach buildings with various characteristics (dimension and pole height) and positioning (relative to each other and the incident wind direction) are still not fully known. It is also noteworthy that no previous studies quantitatively investigated the impact of buildings at the beach on sediment supply from the beach to the dunes. Moreover, understanding the detailed projections of the wind-blown morphologic changes over short to long time scales, i.e. hours to years, is still lacking so far. The previous studies also cannot describe the airflow patterns around a group of buildings with varying characteristics and configurations, so they cannot study the full system.

1.6. RESEARCH GOAL AND QUESTIONS

THE goal of this thesis is *to gain insight in the influence of beach buildings on aeolian sediment transport and resultant morphologic patterns in their surroundings. The influence of building characteristics (dimensions and pole height) and positioning (relative to the neighbouring buildings) and the orientation (with respect to the dominant wind direc-*

tion) at the beach is examined. We are also interested in understanding the flow mechanisms responsible for the evolution of the morphologic patterns only those forced by the buildings (not natural bedforms). To achieve this goal, the following research questions are formulated:

Q1 How do building dimensions (i.e. length, width, and height) influence the airflow and initial aeolian erosion-deposition patterns around an isolated building at the beach?

Q2 How do wind direction and gap size between adjacent buildings affect the airflow, duneward sediment transport and the initial aeolian morphologic patterns around a row of buildings at the beach?

Q3 What are the impacts of buildings pole height on airflow, duneward sediment transport and both the initial and further developed aeolian morphologic patterns?

1.7. RESEARCH METHODS

To quantify the impacts of buildings at the beach on airflow and wind-blown sediment transport, numerical models were developed. We specifically focused on building characteristics such as dimensions and pole height, as well as positioning at the beach relative to the dominant wind direction and the distance from neighbouring buildings. The research methods used for each research question are presented below (Figure 1.5):

To answer **Q1**, firstly a three-dimensional numerical model was developed using OpenFOAM, which is an open-source CFD solver, to simulate airflow around an isolated building. A small-scale building with the length, width, and height of $0.100 \times 0.150 \times 0.125$ m under perpendicular wind condition was modelled. To validate the airflow model, the computed horizontal and vertical wind velocity fields in the vicinity of building were compared with the wind-tunnel measurements by Leitl and Schatzmann (2010). Secondly, the building dimensions (i.e. length, width, and height) were systematically varied in order to quantify the wind speed and flow patterns around the building. Thirdly, the convergence of the third-order horizontal near-bed velocity field was computed and used as a proxy for sand transport convergence to predict initial erosion and deposition patterns around the building.

To answer **Q2**, the 3D OpenFOAM model used for Q1 was used to simulate the airflow around a row of full-scale buildings with the length, width and height approximately similar to the real vacation houses at the beach, $6.0 \times 2.5 \times 2.5$ m. Firstly, the influence of sixteen different gap sizes on near-bed wind velocity field, the flow structures developed around buildings and the bed shear stress were studied. Secondly, to quantify the influence of dominant wind direction relative to the buildings on airflow patterns developed in their surround-

ings, five different wind directions were applied to each tested gap size. Thirdly, a sediment transport model was developed that computes the sediment transport fluxes using the empirical formulation proposed by Bagnold (1941) and the bed shear stress derived from the OpenFOAM model. Fourthly, to quantify the cross-shore (duneward) sediment transport, the net average duneward fluxes across along-shore lines downwind of the buildings were computed. Lastly, the Exner equation was used to derive the initial morphologic patterns around a row of buildings. The modelled bed elevations were then compared to those measured around scaled buildings at the beach by Poppema et al. (2022b).

To answer **Q3**, the model used for Q2 was applied to simulate airflow around and underneath full-scale buildings on poles. Firstly, the impact of elevated buildings on near-bed wind field, bed shear stress and duneward sediment transport based on Bagnold's formulation was studied. Secondly, the net average duneward sediment transport fluxes passing along-shore lines, which were located behind the buildings, were compared for twenty-six tested pole heights. Thirdly, to predict morphologic patterns around buildings over longer time periods, the OpenFOAM model was coupled with an existing sediment transport model, AeoLiS, which was developed by Hoonhout and De Vries (2016). The coupled model benefits from both the detailed bed shear stress computed by the OpenFOAM model, and the complicated sediment transport by AeoLiS. Lastly, both the Exner equation together with the Bagnold's formulation, and the coupled model were used to respectively predict the initial and further developed bed level changes for different pole heights.

1.8. THESIS OUTLINE

THE research questions presented in Section **??** are answered in Chapters 2 to 4. The thesis structure is as follows: **Chapter 2** addresses the development of the model using OpenFOAM and the model validation. The influence of changes in the dimensions of an isolated small-scale building on the airflow and wind-driven erosion and deposition patterns around the building is studied in this chapter (Q1). **Chapter 3** develops a sediment transport model using an empirical formulation, and investigates the impacts of wind direction and the gap size on wind field, duneward sediment transport and the initial bed morphology when full-scale buildings are placed in a row (Q2). The influence of a row of full-scale elevated buildings placed on poles with varying heights on airflow, duneward sediment transport and the bed level changes is studied in **Chapter 4**. Furthermore, a new coupled model is developed that enables the prediction of morphologic patterns around buildings over longer time periods considering the spatiotemporal changes in bed features (Q3). **Chapter 5** further discusses the results, compares them with previous studies and provides the applications and limitations of this study. **Chapter 6** presents the conclusions reflecting

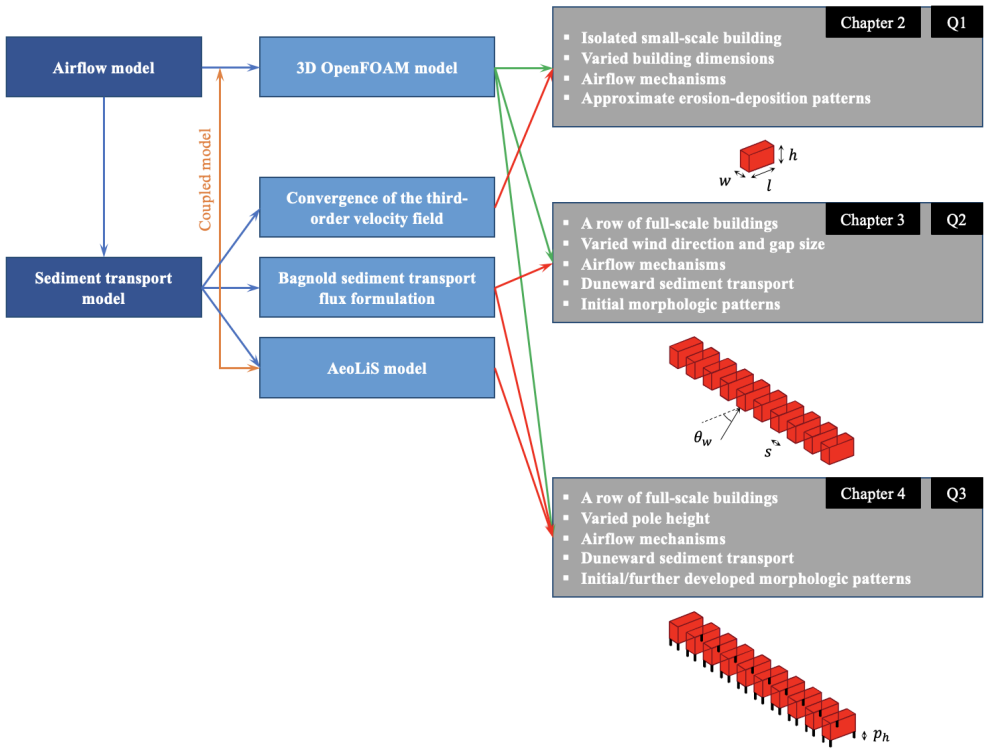

Figure 1.5: An overview of methodologies used to answer each research question.

on what has been achieved with respect to the goal of the thesis, and the recommendations for further research.

2

THE INFLUENCE OF BUILDING DIMENSIONS ON AIRFLOW PATTERNS AND INITIAL BED MORPHOLOGY

This chapter is published as Pourteimouri, P., Campmans, G. H. P., Wijnberg, K. M. and Hulscher, S. J. M. H. (2022). A Numerical Study on the Impact of Building Dimensions on Airflow Patterns and Bed Morphology around Buildings at the Beach. *Journal of Marine Science and Engineering*, 10(1), 13. DOI: 10.3390/jmse10010013

ABSTRACT: The attractiveness of beaches to people has led, in many places, to the construction of buildings at the beach-dune interface. Buildings change the local airflow patterns which, in turn, alter the sediment transport pathways and magnitudes. This induces erosion and deposition patterns around the structures. In this study, a numerical model is developed using the open-source computational fluid dynamics solver OpenFOAM. First, the model is used to predict the airflow patterns around a single rectangular building. The model predictions are validated with wind-tunnel data, which show good agreements. Second, a reference beach building is introduced and then the building dimensions are increased in length, width and height, each up to three times the reference building dimension. The impact of each dimensional extent on the near-surface airflow patterns is investigated. The results show that the near-surface airflow patterns are least dependent on the length of the building in the wind direction and they depend most on the width of the building perpendicular to the wind direction. Third, the convergence of the third-order horizontal near-surface velocity field is calculated to interpret the impact of changes in airflow patterns on potential erosion and deposition patterns around the building. The numerical predictions are compared with the observed erosion and sedimentation patterns around scale models in the field. The comparisons show satisfactory agreements between numerical results and field measurements.

2.1. INTRODUCTION

COASTAL zones worldwide have always been attractive to humans, since they provide a wide variety of valuable resources and recreational activities. Population growth near coastlines leads to an increased demand for construction of restaurants, sailing clubs, holiday cottages and pavilions at the beach-dune interface. Figure 2.1 shows some typical example of these structures.

(a) (b)

Figure 2.1: Buildings at beach-dune interface on the a) Egmond beach, and b) Zandvoort beach (www.hollandluchtfoto.nl), the Netherlands.

A considerable number of studies indicated that the coastlines worldwide have been modified over millennia by human interventions, and this development is continuously growing (Marsh, 1874; H. J. Walker, 1984; Nordstrom, 1994; Jackson and Nordstrom, 2011). There are complex interactions between airflow patterns, sediment transport and bed morphology on the beach. These interactions vary over a wide range of spatial and temporal scales and determine the shape, size, spacing and alignment of beaches and aeolian sand dunes (Walker and Nickling, 2002). The impact of buildings at the beach can be schematized by a loop as in Figure 2.

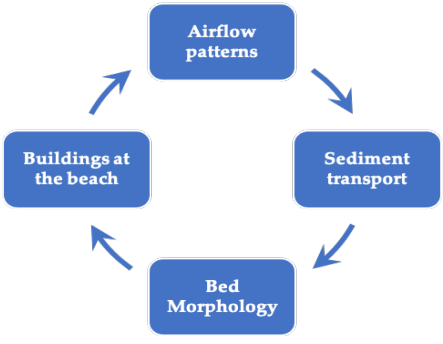

Figure 2.2: Morphological loop indicating the interactions between buildings at the beach, airflow patterns, sediment transport and bed morphology.

Buildings at the beach affect local airflow patterns and as a result aeolian sediment transport. These airflow patterns depend on building dimension, geometry, orientation, elevation from ground level, surface roughness and the positioning and distance in a row of buildings on the beach (Nordstrom, 2000). According to Jackson and Nordstrom (2011), the dimensions of a building affect the degree to which a structure acts as an obstacle against wind flow and sediment migration. This affects the ability of airflow or sediment particles to move across the top of the structure or around the lateral sides of the structure. Therefore, buildings at the beach-dune interface locally alter wind flow patterns and change the location of erosion and accretion on the beach (Nordstrom and McCluskey, 1985; Nordstrom et al., 1986). At longer time scales, the buildings could potentially change the dynamic state of the adjacent dune system, as they may modify the amount and spatial distribution of aeolian sand supply from the beach to the dune. Dunes provide natural flood protections against storm surges. Therefore, the coastal safety might be affected as dunes become more mobile and variability in height increases. Furthermore, a building could locally increase deposition or cause intensive erosion around the structure. These morphological changes affect the buildings at the beach. They might result in the need for sediment removal or even cause the tilting of the structure that affects the building functionality. Therefore, people move their houses elsewhere due to the excessive erosion and deposition, or change the shape of their houses by constructing on poles, for example, to prevent the buildings' dysfunctions. The impacts of buildings on wind flow and impacts of wind flow on buildings have been well addressed in the literature, focusing on applications such as pedestrian wind comfort, air pollutant dispersion, heat transfer, natural ventilation and wind-driven snow or rain around buildings. However, only a few studies have been conducted on the effects of building characteristics, specifically the impacts of building dimensions, on near-surface wind flow patterns and bed morphology at the beach. Fackrell (1984) and Beranek (1984) conducted wind-tunnel studies to investigate wind flow around buildings with various dimensions. Fackrell (1984) found that the length of the recirculation region behind the building, which was defined as the distance between the leeward face of the structure and the reattachment point of the separated flow, increases with increasing building width normal to the flow direction as well as with decreasing building length parallel to the flow direction. Martinuzzi and Tropea (1993) performed experiments to study the impact of width-to-height aspect ratio, W/H, of surface mounted obstacles on the flow patterns and parameters including windward separation and leeward reattachment lengths. They found that the separation length in front of the obstacle increases with increasing width up to about $W/H \approx 6$ and then decreases slightly for higher ratios. The indications showed that the reattachment length behind the obstacle increases linearly with increasing width up to about $W/H \approx 4$ and then asymptotically approaches a constant value. Considering the impact of roughness elements, similar to buildings, on bed topography, Iversen et al.

(1990) and Iversen et al. (1991) conducted wind-tunnel tests on the sand bed to determine the impacts of obstacles with different dimensions on local aeolian erosion and deposition patterns. They found that the flow patterns and therefore the sand transport, depend considerably on the obstacle aspect ratio which was defined as the ratio of obstacle height to lateral width. Their studies showed that the observed erosion on the windward side of the rectangular object was caused by the formation of a horseshoe-type vortex. In a more detailed study performed by Tominaga et al. (2018), sand erosion and deposition patterns around a surface-mounted cube was investigated using a wind-tunnel experiment. The results showed a considerable erosion at the upwind edges of the cube extended downwind along the lateral faces, and a small amount of sand accumulation at the leeward face of the cube. They found that the largest amount of erosion in the streamwise direction, x, occurs at $x/H = -0.75$ in front of the windward face of the cube, while the largest amount of erosion in the spanwise direction, z, occurs at $z/H = 0.85$ from the lateral sides of the cube, where H was defined as the cube height. Luo et al. (2012) performed wind-tunnel tests to improve the understanding of the airflow patterns downwind of cuboid obstacles and to interpret the formation of the sand shadows observed behind obstacles in arid regions. In their studies, they investigated the impact of obstacle shape ratio on both horizontal and vertical airflow patterns around the structures. The shape ratio was defined as the ratio of the top area of the obstacle to its frontal area normal to the wind direction. Considering H as the height of the obstacle, the measurements showed that the flow begins to reattach and move along the bed surface at some distance between $2.5H$ to $3H$ from the separation point. They concluded that the formation of the low-velocity bubble downwind the obstacle causes sediment deposition behind the leeward face. Sutton and McKenna Neuman (2008) studied the impact of vortical structures formed in the vicinity and in the wake of the cylindrical objects on the initiation of sediment transport. Their results show that the two counter-rotating vortices in the lee of the cylindrical objects allow the sediment entrainment to occur at lower wind speeds than that of required far away from the objects and in their wakes. The spacing between the cylindrical objects influences the strength of the two counter-rotating vortices, therefore may cause an increase in the sediment activity around cylindrical objects.

Beyers and Waechter (2008) developed a CFD model to investigate the development of wind-driven snowdrifts around buildings. As they noted in their study, it is necessary to take the impacts of flow divergence into account in order to predict the development of snowdrifts realistically, while the commonly used models only rely on the threshold wind shear velocities to derive the snow erosion and deposition patterns around buildings.

The aforementioned studies show that the previous research mainly focused on the general airflow patterns around the buildings. However, the detailed quantitative impacts of

building dimensions on near-surface airflow patterns have remained poorly understood, despite their important role in near-surface aeolian sediment transport. In addition, first attempts to find a relation between near-surface airflow patterns and near-surface erosion and deposition patterns around the buildings go back to the experimental work by Luo et al. (2012). However, their study was limited to the airflow patterns behind the obstacles that cause the evolution of sand shadows in arid regions over time. Furthermore, Poppema et al. (2021) studied the size of deposition patterns around single buildings of different dimensions. However, their study does lack the detailed information on airflow patterns inducing those patterns.

Therefore, in the present study we systematically investigate the impact of building dimensions on the nature and extent of near-surface airflow patterns and the potential morphological changes induced by those flow fields when buildings are placed at a sand surface. We consider a wide area around the buildings to also capture the deposition patterns like those observed by Poppema et al. (2021). The building dimensions considered are length, width and height. The systematic study means that the building dimension is increased in each direction, while the other two dimensions remain unchanged. The two main research questions this study addresses are: Q1) What are the detailed quantitative impacts of building length, width and height on near-surface airflow patterns which drive wind-driven sediment transport around buildings?; Q2) What are the qualitative impacts of building length, width and height, on initial morphologic changes driven by wind around buildings at the beach?

In this paper, first a general description of airflow patterns and complex flow structures around an isolated building or a cube are presented in Section 2.1.1. In Section 2.2, the numerical modelling approach is explained. The detailed explanation of the numerical model itself and the validation of the model are provided in Appendix 2.A and 2.B, respectively. Results related to Question 1, on near-surface airflow patterns around buildings with different length, width and height, are presented in Section 2.3.1. Results related to Question 2, on the impact of building dimensions on wind-driven erosion and deposition patterns, are presented in Section 2.3.2. The paper ends with the discussion in Section 2.4, and conclusions that are presented in Section 2.5.

2.1.1. WIND FLOW AROUND AN ISOLATED BUILDING

THE wind flow pattern in the vicinity of an isolated building is highly complex. The intrusion of a building, that acts as an impermeable obstacle, into the atmospheric boundary layer causes strong perturbations and complex flow structures in its vicinity. This perturbation is characterized by converting mean kinetic energy to turbulent kinetic energy

due to the formation of eddies that are rotating faster or slower than the eddies in the mean flow (Oke et al., 2017). Figure 2.3 shows flow features around an isolated cubical building with an orientation normal to the incident wind flow.

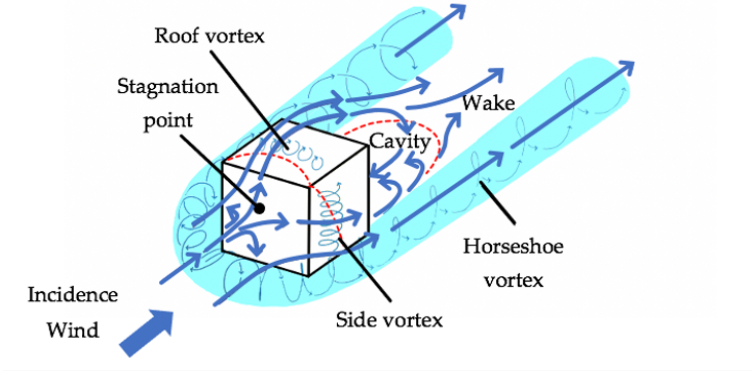

(a)

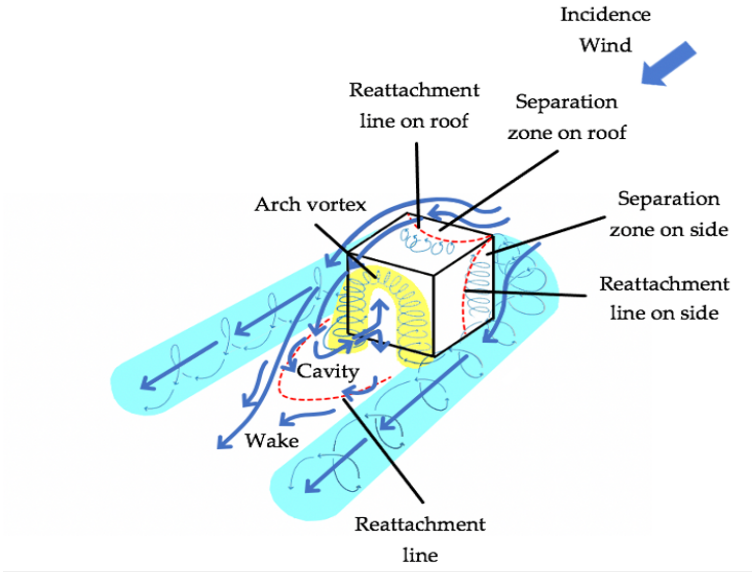

(b)

Figure 2.3: Schematic airflow patterns around an isolated cubical building with wind incidence angle perpendicular to the building a) windward view, and b) leeward view (modified from Oke et al. (2017) and Blocken et al. (2011)).

As wind approaches a building, the flow streamlines are deflected over and around the structure which is due to the formation of high pressure gradients on the windward face. A stagnation point with the highest pressure is formed on the windward face of the building at an elevation approximately two thirds of the building height (Peterka et al., 1985; Blocken

et al., 2011). The location of the stagnation point depends on the building frontal aspect ratio, the height of the building in comparison with the height of the atmospheric boundary layer and the surface roughness upwind of the building (Peterka et al., 1985). The approaching flow diverges from the stagnation point to the zones with lower pressure including up over the roof, around the lateral sides and down the windward face towards the surface. When the upward and sideward flows encounter the windward edges of the building, they are detached from the surface and flow separation takes place. The separation bubbles on both the roof and the lateral sides of the building are characterized by the reverse flows, low velocity distributions and relatively high turbulence intensities (Blocken et al., 2011). This happens due to the air suction induced by low-pressure zones on the roof and lateral sides of the building. The detached flow might reattach to the roof or side walls of the building depending on the top and lateral aspect ratios, and upstream surface roughness that determines the turbulence intensity of the incidence flow (Peterka et al., 1985; Hunt, 1971). As mentioned earlier, some of the flow approaching the windward face of the building is deflected downwards to the ground and moves in the reverse direction compared to the incident wind direction. The reversed flow undercuts the incident wind flow and causes it to be detached from the ground level and creates a standing vortex near the bed surface just upstream the windward face of the building (Oke et al., 2017). This primary roll-like vortex induces formation of additional vortices that are smaller in size and weaker than the main vortex structure and are eventually connected to the primary vortex around the lateral sides of the building. This vortex is then stretched around the side walls and is extended downwind the building creating a so-called horseshoe-shape vortex, shaded blue in Figure 2.3 (Peterka et al., 1985).

The flow structures formed behind the building are very complex. The low-pressure zone at the leeward face of the building creates air suction in a so-called cavity region. In this region, the along-wind flow passing over the roof of the building and two horizontally-oriented flows around the lateral sides of the building move in the reverse direction compared to the incidence wind flow, creating a recirculating zone just downstream of the leeward face of the building. The dashed line downstream of the building in Figure 2.3b shows the end of the cavity region where the streamlines are reattached to the ground surface (Oke et al., 2017; Blocken et al., 2011). For a wind incidence angle perpendicular to the upwind face of a cubical building, the height of the cavity region is about $1.5H$, where H is the building height and the length of the cavity region extends to about 2.5 to $3H$, measured from the upstream face of the building. The flow interference increases with increasing building width normal to the wind direction, therefore the cavity region height increases to some extent and its length reaches $12H$ for wide buildings with small height-to-width aspect ratios (Meroney, 1982). The horizontal flow patterns behind the rear face of the building show

the formation of two counter-rotating vortices that join their extensions at the vertical symmetry plane (yellow shaded vortex in Figure 2.3b). These spiral vortices entrain some air from the horseshoe-shape vortex, created near the ground level, and whirl it upwards to create a vertically-oriented arch-shape vortex just downstream of the building (Peterka et al., 1985; Martinuzzi and Tropea, 1993; Meinders et al., 1999). Beyond the cavity region, the reattached flow moving in the direction of approaching flow requires some distance to recover the features of incidence wind flow and release all perturbations, separation impacts and secondary flow structures induced by the presence of building. This occurs in the so-called wake region that is characterized by velocity deficits, higher turbulence intensities and smaller scale eddies compared to the eddies in the incidence wind flow (Meroney, 1982; Peterka et al., 1985). The wake region typically persists to about 5 to 30H downwind of the building and its height reaches to about 3 to 4H at a distance of 10H downstream of the building (Meroney, 1982; Oke et al., 2017).

2.2. METHODS

2.2.1. COMPUTATIONAL FLUID DYNAMICS (CFD)

IN the past few decades, the advances in computing power have led to a significant progress in the application of two and three-dimensional computational fluid dynamics models in wind engineering and aeolian geomorphology (Bitsuamlak et al., 2004; Blocken et al., 2011; Smyth, 2016). In CFD models, the flow motion is solved numerically using the Navier-Stokes equations that are a set of partial differential equations including the conservation of mass, conservation of momentum in three dimensions and the conservation of energy. Considering the finite volume method, the computational domain is discretized into a finite number of control volumes and using numerical algorithms, the governing Navier-Stokes equations are integrated over all control volumes. This results in the conversion of partial differential equations into a set of algebraic equations before solving them (Versteeg and Malalasekera, 1995). For a systematic study of the effect of building dimensions on airflow, application of computational fluid dynamics offers considerable advantages over field measurements and wind-tunnel experiments. The main advantage is that the geometrical design and boundary conditions such as wind speed, incidence angle and shear velocity as well as surface roughness can be changed relatively quickly to systematically analyze the influence of an individual parameter on results. Moreover, the flow field can be solved in very small control volumes that enables the observation of detailed flow features. In addition, CFD simulations avoid scaling issues that might happen in wind-tunnel experiments as the geometrical design can be modelled exactly at the dimensions of interest. This facilitates the validation procedure, since the flow features at the same spatial scales can be com-

pared in both numerical model and experimental results. Furthermore, CFD models avoid the impacts of walls in wind-tunnel experiments, using appropriate boundary conditions. This permits wind flow to leave the computational domain from the lateral sides and the outlet of the domain, and avoids the reflective impacts of walls (Versteeg and Malalasekera, 1995; Blocken et al., 2011; Smyth, 2016). A main disadvantage of CFD is that it can be computationally expensive when increasing the resolution of the computational mesh and/or the size of the computational domain. In practice, the required level of detail and the minimum required three-dimensional space to be simulated, put a limit to the number of cases that are feasible to simulate in a given study. In this study, a numerical model is developed using OpenFOAM, which is an open-source CFD software. The details of the numerical model including governing equations, turbulence modelling, boundary conditions and initial internal fields are presented in Appendix 2A of this paper. The model validation is presented in Appendix 2B of this paper, which shows the capability of the numerical model in predicting the airflow patterns around an isolated building.

2.2.2. COMPUTATIONAL DOMAIN

A three-dimensional rectangular computational domain, shown in Figure 2.4, is considered for modelling airflow patterns around an isolated building. The definition of the geometric parameters shown in Figure 2.4, are given in Table 2.1. Essentially, the scale models of buildings in a numerical wind-tunnel without side wall effects are simulated. We study the impact of relative increases in each dimension, using scale model sized buildings. The dimensions of both the computational domain and the building are selected based on the wind-tunnel experiments performed by Leitl and Schatzmann (2010), and their measurements are used in Appendix 2B of this paper for the model validation. It should be noted that using such a small-scale model in comparison with real buildings at the beach shows the capability of CFD in simulating scaled models. The computational domain inlet is located at $x = 0$ m, and the domain length, width and height are $(L_u^{"} + L_d^{"}) \times 2W^{"} \times H^{"}$, respectively. A rectangular surface-mounted building with the length of $l^{"}$, width of $w^{"}$ and height of $h^{"}$ is specified within the computational domain, where the building center is located at $x = 1$ m. The computational domain and the building dimensions are symmetric in the spanwise direction, z. The so-called blockMesh and refineMesh utilities in OpenFOAM are used to create structured hexahedral mesh over the computational domain.

In this study, a computational domain with the length of 3 m, width of 2 m and height of 1.5 m is used. The reference building with the length of $l_0^{"}$, width of $w_0^{"}$, and height of $h_0^{"}$, is considered within the domain. The atmospheric boundary layer parameters are chosen based on the wind-tunnel experiments performed by Leitl and Schatzmann (2010) that are presented in Appendix 2A.3. Considering computational grids with a size almost equal to

0.0125 m and a height of the ground adjacent cells of 0.03 m, the total number of cells in the mesh is approximately 4.57 million. In order to systematically study the impacts of building length, width and height, the reference building is increased in each direction up to three times the reference quantity, while the other two dimensions remain constant. This results in thirteen different simulations as specified in Table 2.2. It should be noted that the building center in all simulations is located at $x = 1$ m.

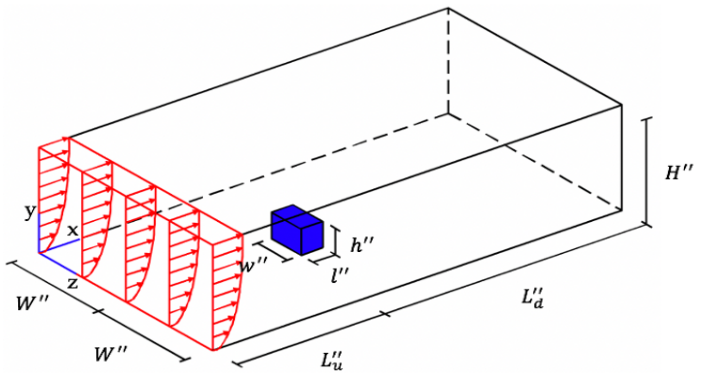

Figure 2.4: Schematic configuration of the computational domain and the surface-mounted building.

Table 2.1: Definition and values of the geometric parameters of the computational domain and the surface-mounted building.

Parameter	**Definition**
$L_u^{"}$	Upstream distance between the domain inlet and the building centerline
$L_d^{"}$	Downstream distance between the domain outlet and the building centerline
$W^{"}$	Lateral distance between the lateral sides of the domain and the building centerline
$H^{"}$	Height of the domain
$l^{"}$	Length of the building
$w^{"}$	Width of the building
$h^{"}$	Height of the building

Table 2.2: An overview of the conducted simulations and the building dimensions in each case. The length, width and height of the computational domain is 3 m, 2 m and 1.5 m, respectively.

Simulation ID	**Building length** ($l^{"}$) **[m]**	**Building width** ($w^{"}$) **[m]**	**Building height** ($h^{"}$) **[m]**
		Reference building	
$l_0^{"} \times w_0^{"} \times h_0^{"}$	0.1000	0.1500	0.1250
		Impact of building length	
$1.5l_0^{"} \times w_0^{"} \times h_0^{"}$	0.1500	0.1500	0.1250
$2l_0^{"} \times w_0^{"} \times h_0^{"}$	0.2000	0.1500	0.1250
$2.5l_0^{"} \times w_0^{"} \times h_0^{"}$	0.2500	0.1500	0.1250
$3l_0^{"} \times w_0^{"} \times h_0^{"}$	0.3000	0.1500	0.1250
		Impact of building width	
$l_0^{"} \times 1.5w_0^{"} \times h_0^{"}$	0.1000	0.2250	0.1250
$l_0^{"} \times 2w_0^{"} \times h_0^{"}$	0.1000	0.3000	0.1250
$l_0^{"} \times 2.5w_0^{"} \times h_0^{"}$	0.1000	0.3750	0.1250
$l_0^{"} \times 3w_0^{"} \times h_0^{"}$	0.1000	0.4500	0.1250
		Impact of building height	
$l_0^{"} \times w_0^{"} \times 1.5h_0^{"}$	0.1000	0.1500	0.1875
$l_0^{"} \times w_0^{"} \times 2h_0^{"}$	0.1000	0.1500	0.2500
$l_0^{"} \times w_0^{"} \times 2.5h_0^{"}$	0.1000	0.1500	0.3125
$l_0^{"} \times w_0^{"} \times 3h_0^{"}$	0.1000	0.1500	0.3750

2.2.3. METHODOLOGY FOR DERIVING BED LEVEL CHANGE FROM AIRFLOW PATTERNS

IN this study, we are interested in predicting the potential impact of airflow patterns around buildings on the bed level changes of the surrounding area when that area consists of moveable substrate. Commonly used sediment transport models show that the sediment transport rate, q, is proportional to the third-order velocity field ($q \propto \vec{U}^3$) (Bagnold, 1936; O'brien and Rindlaub, 1936; Kawamura, 1951; Zingg, 1953; Owen, 1964; Hsu, 1971; Iversen et al., 1976; Maegley, 1976; Lettau and Lettau, 1977; B. R. White, 1979). In this study, it is assumed that the sediment will transport at the near-bed wind speed, and it will stay close to the bed. Therefore, as a first step, the vertical component of the velocity field can be neglected and the sediment transport rate can be written in the following form:

$$q \propto (|\overrightarrow{U_H}|^2 \overrightarrow{U_H}) \tag{2.1}$$

where the index H denotes the horizontal near-surface velocity field. The Exner equation states that the temporal rate of change in bed elevation is proportional to the convergence of sediment transport rate:

$$\frac{\partial z_b}{\partial t} \propto -\nabla \cdot q \tag{2.2}$$

where z_b [m] is the bed elevation, t [s] is the time, and q [kg/m/s] is the sediment transport rate. Substituting Eq. 2.1 into Eq. 4.2 gives:

$$\frac{\partial z_b}{\partial t} \propto -\nabla \cdot (|\overrightarrow{U_H}|^2 \overrightarrow{U_H}) \tag{2.3}$$

Considering Eq. 2.3, a positive convergence of the third-order horizontal wind velocity field in a near-surface plane implies a decrease in sand transport rate hence deposition. Similarly, a negative convergence of the third-order horizontal wind velocity field in a near-surface plane implies an increase in sand transport rate hence erosion:

$$\begin{cases} -\nabla \cdot (|\overrightarrow{U_H}|^2 \overrightarrow{U_H}) > 0 & \rightarrow \quad Deposition \\ -\nabla \cdot (|\overrightarrow{U_H}|^2 \overrightarrow{U_H}) < 0 & \rightarrow \quad Erosion \end{cases} \tag{2.4}$$

2.3. RESULTS

2.3.1. NEAR-SURFACE AIRFLOW PATTERN

THE impacts of building dimensions on airflow patterns near the beach surface and the potential implications for bed morphology are investigated. We focus on investigating the impacts of building length, width and height on near-surface airflow patterns, as our main motivation for this work is its implication for sediment transport. Therefore, we show the results of wind velocity magnitude at a horizontal plane close to the bed, i.e. $y = 0.0125$ m, which is located at an elevation equal to ten percent of the reference building height.

The impact of building length parallel to the incidence wind direction on near-surface wind velocity magnitude is presented in Figures 2.5a-e. The first glance into the results shows that the building length does not have significant impact on the near-surface airflow patterns adjacent to the building. In order to take a deeper look into results, the effect of building length on the length of the downwind recirculation region just behind the building, L_d, which is defined as the distance between the reattachment point of the separated flow and

the leeward face of the building, is shown in Figure 2.5f. It should be noted that the reattachment point at a near-surface plane, $y = 0.0125$ m, is located on the centreline of the computational domain, where the horizontal component of the velocity, u, changes in sign.

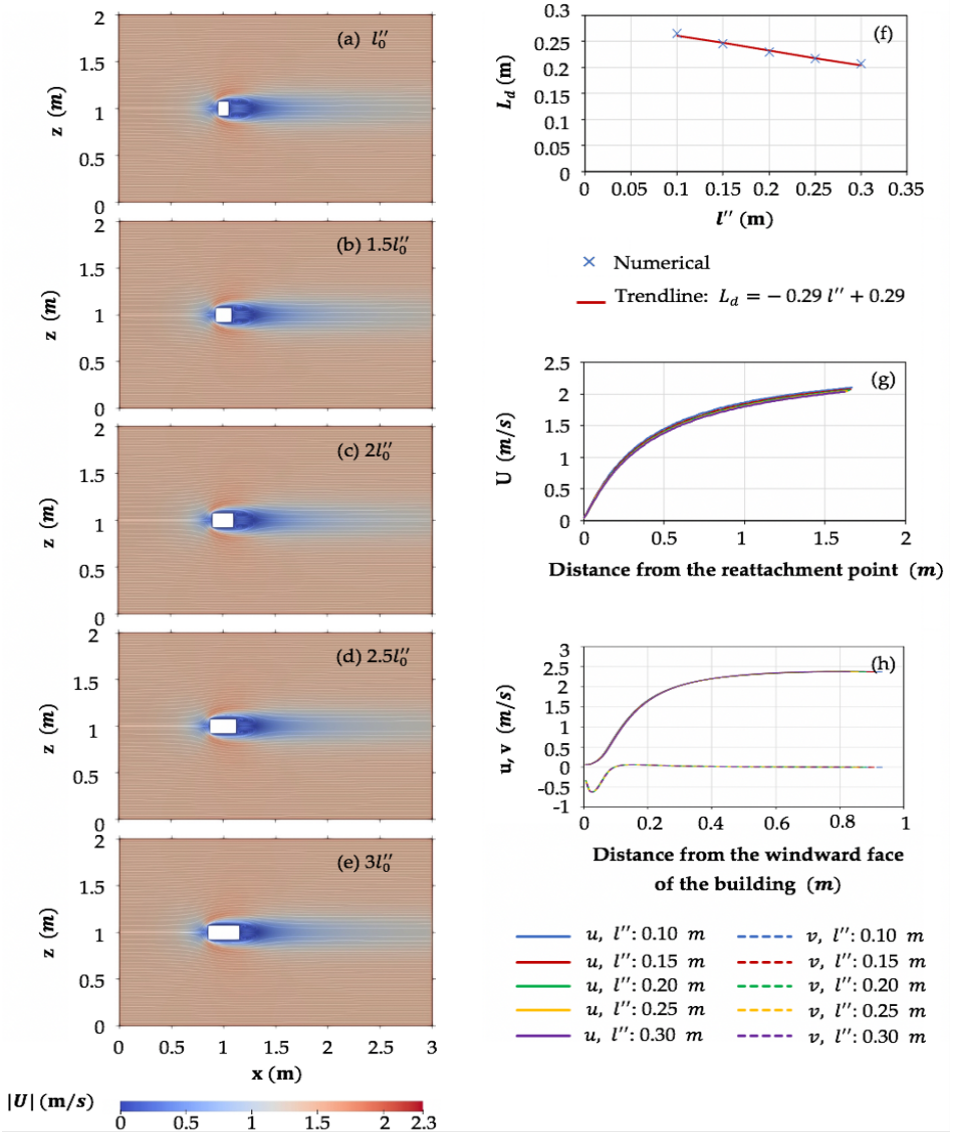

Figure 2.5: The impact of building length on a-e) wind velocity magnitude (color) and direction (streamlines), f) length of the downwind recirculation region, L_d, just behind the leeward face of the building along the centerline, g) wind velocity magnitude downstream of the building after flow reattachment along the centerline, and h) streamwise, u, and vertical wind velocity components, v, upstream of the building along the centerline. Results are derived for a horizontal near-surface plane, $y = 0.0125$ m. The building width and height are $w_0^{"}$ and $h_0^{"}$, respectively. The building length, $l^{"}$, is varied as $l_0^{"}$, $1.5l_0^{"}$, $2l_0^{"}$, $2.5l_0^{"}$, and $3l_0^{"}$.

As shown in Figure 2.5f, the length of the recirculation zone just downstream of the building rear face decreases with increasing building length. This happened due to the reattachment of the detached flow on the roof of the longer building. In order to understand to what extent the velocity deficits due to the presence of the buildings with different lengths continue downwind of the reattachment point, Figure 2.5g shows the changes in wind velocity magnitude along the domain centreline with respect to the distance from the reattachment point. According to Figure 2.5g, the wind velocity magnitude increases gradually with increasing distance from the reattachment point until it eventually reaches the undisturbed wind velocity magnitude. Furthermore, the results show that it takes a bit longer distance for the wind to reach a certain speed for the longer building.

Figure 2.5h shows how streamwise and vertical velocity components change along the domain centreline as the wind approaches the windward face of the building. Figure 2.5h shows that the near-surface streamwise wind velocity generally decreases with decreasing distance from the windward face of the building, where it changes more rapidly when the distance from the building front face is smaller. The vertical wind velocity is approximately zero until the wind is close the building's windward face, where a local peak occurs due to the small recirculation region that forms in front of the building and close to the surface. This recirculation develops due to downward deflection of the flow along the front face of the building to the ground, where it deflects again leading to near-bed flow in the opposite direction of the incident wind direction. The results further show that building length has no influence on the length of the upstream area with reduced streamwise wind velocities.

The impact of building width on near-surface wind velocity magnitude is presented in Figures 2.6a-e. The general flow patterns show that the wider building disturbs a longer and wider area both in front of the windward face and behind the leeward face of the building. Furthermore, the wind velocity magnitude of the flow passing around the windward edges and the lateral sides of the building increases with increasing building width. The reason is that the wind flow approaching the front face of the building is separated into two flow branches in the horizontal plane, passing around the sidewalls of the building. The pressure gradient between the point of separation, in the middle of the building width, and the upwind edges of the wider building is greater, causing the higher wind velocity magnitude values around the windward edges and the lateral sides of the building. Figure 2.6f shows the effect of building width on the length of the recirculation region just behind the leeward face of the building, L_d. The comparisons between the five different building widths show that the wider building causes the formation of a longer recirculation region just downstream of the building. It can be seen that there is a linear relation between the width of the building and the length of the downwind recirculation zone. The steep slope of the trendline shows that the length of the recirculation zone is highly sensitive to the building width. The results

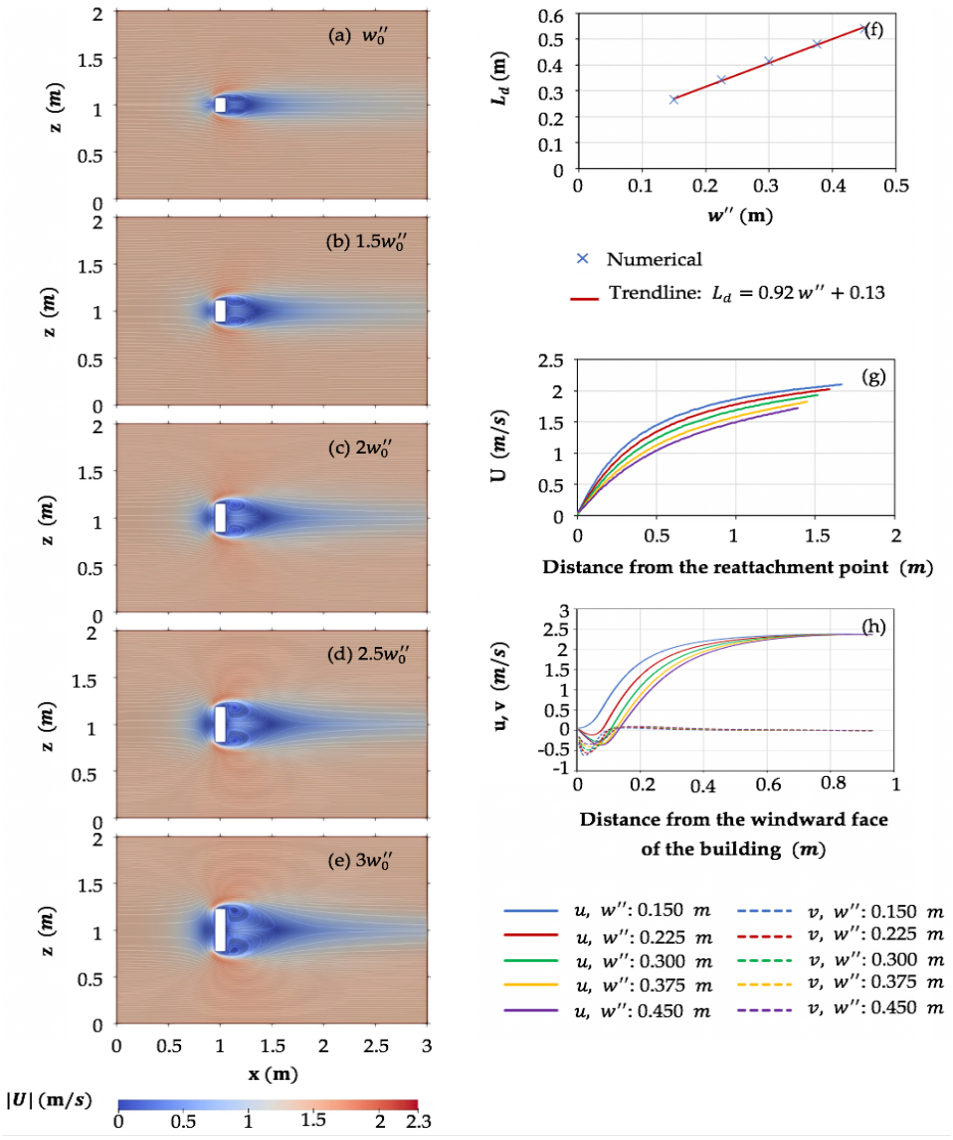

Figure 2.6: The impact of building width on a-e) wind velocity magnitude (color) and direction (streamlines), f) length of the downwind recirculation region, L_d, just behind the leeward face of the building along the centerline, g) wind velocity magnitude downstream of the building after flow reattachment along the centerline, and h) streamwise, u, and vertical wind velocity components, v, upstream of the building along the centerline. Results are derived for a horizontal near-surface plane, $y = 0.0125$ m. The building length and height are $l_0^{"}$ and $h_0^{"}$, respectively. The building width, $w^{"}$, is varied as $w_0^{"}$, $1.5w_0^{"}$, $2w_0^{"}$, $2.5w_0^{"}$, and $3w_0^{"}$.

of wind velocity magnitude downstream of the flow reattachment point presented in Figure 2.6g show that behind a wider building the near surface wind velocity magnitude recovers

more slowly over distance from the velocity deficit at the flow reattachment point, where near surface wind velocity magnitude is almost zero.

The changes in streamwise and vertical wind velocities upstream of the windward face of the building are presented in Figure 2.6h. The results show that the wider the building, the further upwind of the building the minimums of the wind velocity components occur, meaning that the size of the near-bed recirculation region in front of the building increases with increasing building width. Furthermore, it can be concluded from the figure that the streamwise wind velocity deficit for the wider building continue for a longer distance upstream of the building. However, the rate of change decreases with increasing building width. The streamwise wind velocity reaches the undisturbed wind field far away from the building. The negative streamwise wind velocity shows the reversed flow, which depends on the size of the recirculation region in front of the building, and the elevation at which the results were plotted ($y = 0.0125$ m in this study).

The impact of building height on near-surface wind velocity magnitude is presented in Figures 2.7a-e. The overall flow patterns show more substantial disturbance downstream of the building than upstream of the building. Furthermore, the wind velocity magnitude around the upwind edges and the lateral sides of the building increase considerably with increasing building height. It is obvious that the increase in the near-surface wind velocity magnitude is greater when the building is getting higher in comparison to getting wider. This can be explained by both the pressure gradient and the friction effects that dissipate higher amounts of kinetic energy of the wind flow when passing around the wider buildings. For the wider building, the near-surface flow approaching the building and deflecting towards the lateral sides, travels a longer distance towards the flow detachment at the windward corners of the building compared to the higher building. Therefore, frictional effects act over a longer distance and dissipate higher amounts of kinetic energy of the airflow which, in turn, result in lower wind velocity magnitude around the lateral sides of the wider building. Figure 2.7f shows that the taller building creates two longer counter-rotating vortices, therefore a longer recirculation region downstream of the building, L_d.

The comparisons between five buildings with different heights (Figure 2.7f) show the high sensitivity of the length of the downwind recirculation zone to building height, however the slope of the trendline shows that the impact of building height on the length of the downwind recirculation zone is smaller than that of building width. As shown in Figure 2.7g, the influence of building height on the extension of the velocity deficits downwind of the flow reattachment point follows the same pattern as the building width, meaning that the velocity deficits continue for a longer distance from the reattachment point for the taller building. However, the rate of wind velocity magnitude increase over distance is smaller

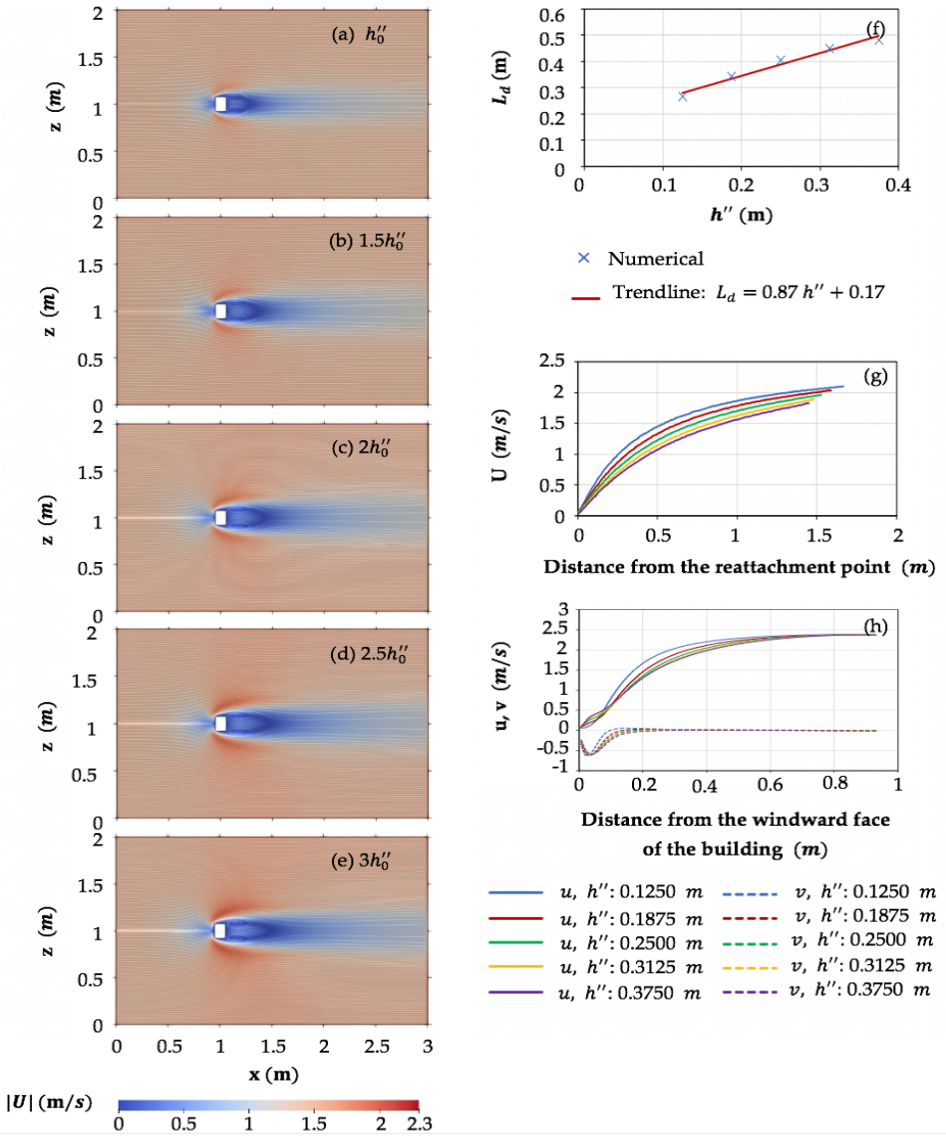

Figure 2.7: The impact of building height on a-e) wind velocity magnitude (color) and direction (streamlines), f) length of the downwind recirculation region, L_d, just behind the leeward face of the building along the centerline, g) wind velocity magnitude downstream of the building after flow reattachment along the centerline, and h) wind velocity magnitude, streamwise, u, and vertical velocity components, v, upstream of the building along the centerline. Results are derived for a horizontal near-surface plane, $y = 0.0125$ m. The building length and width are $l_0^{"}$ and $w_0^{"}$, respectively. The building height, $h^{"}$, is varied as $h_0^{"}$, $1.5h_0^{"}$, $2h_0^{"}$, $2.5h_0^{"}$, and $3h_0^{"}$.

than that for buildings with different widths.

An effect of building height on the streamwise and vertical wind velocities upwind of the

building is that a taller building creates the local wind velocity magnitude peak at a larger distance from the windward face of the building (Figure 2.7h). In addition, Figure 7h shows that the wind velocity magnitude at the center of the recirculation region formed in front of the windward face of the taller building is highest. For the taller building, the wind flow can be less easily released over the building. Therefore, a larger portion of the wind flow moves downwards along the windward face of the building and towards the lateral sides of the building. This implies winds at higher elevation, with higher amount of kinetic energy, move downward. The high-speed downward directed airflow causes the formation of the recirculation region with high-speed magnitudes in front of the taller building. It can be understood from the figure that the length of the low-speed region in front of the building increases with increasing building height, however the rate of change decreases when the building height increases. It is also noteworthy that the magnitude of the local minimum in near-surface windspeed increases with building height to such an extent that there is hardly a difference for the tallest building. The reason is that the flow can move over the smaller building, while more flow blockage happens when the building height increases. This might increase the size of the circulation region in front of the building, and the local minimum in near-surface windspeed.

2.3.2. IMPACTS OF BUILDING DIMENSIONS ON INITIAL BED LEVEL CHANGE

2.3.2.1. CONVERGENCE OF THE THIRD-ORDER HORIZONTAL NEAR-SURFACE FLOW FIELD AS A PROXY FOR INITIAL BED LEVEL CHANGE

IN order to validate the assumption that the convergence of the third-order horizontal near-surface flow field is a good proxy for initial bed level change, and to study the impact of scaling on erosion and deposition patterns around buildings, two new airflow simulations were made. The first simulation is a full-scale building with the length, width and height of 12 m, 2.5 m and 2.5 m, respectively, that is exactly with the same dimension as the full-scale building tested at the Noordwijk beach. It should be noted that he inflow boundary condition for the large-scale simulation are the same as the smaller scale simulations (Appendix 2A.3). The second simulation is a small-scale building with the length, width and height of 0.72 m, 0.15 m and 0.15 m, respectively. It should be noted that these dimensions were selected in a way to reproduce the same frontal and lateral aspect ratios as the full-scale building tested at the Noordwijk beach. Both full-scale and small-scale numerical model results for the bed level rate of change derived from the convergence of the third-order horizontal wind velocity field at near-surface planes are compared qualitatively to field observations of erosion and deposition patterns around experimental models at the beach (Figure 2.8 and Figure 2.9). The full-scale model at the beach near Noordwijk in the Netherlands consists of two shipping containers that were placed besides each other with

the total size of 12×2.5×2.5 m in length, width and height, respectively. The containers were placed alongshore and parallel to the dunes with a distance of 20 m from the dune foot. The dominant wind direction was parallel or in a small angle with model's centerline. A more extensive description of the experimental models at the beach can be found in Poppema et al. (2021).

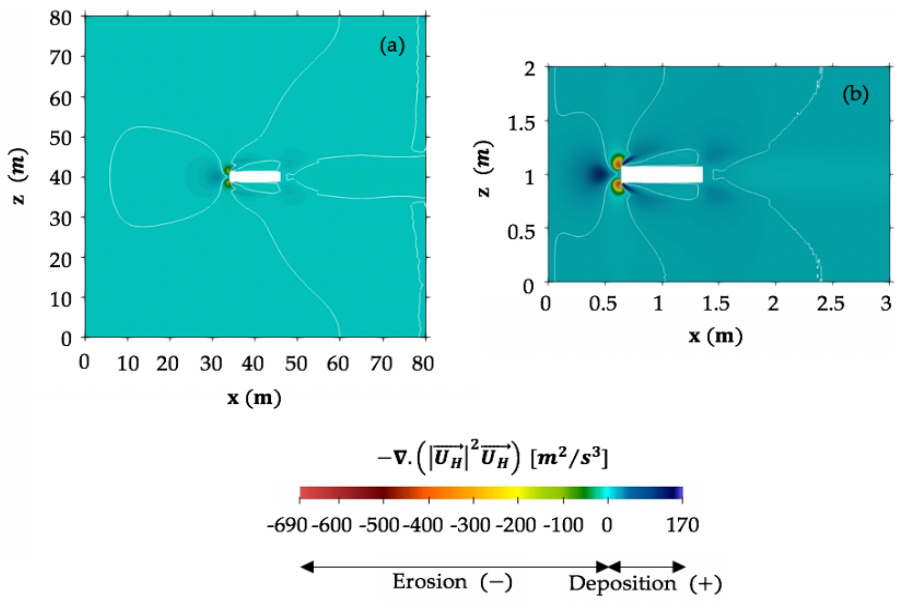

Figure 2.8: Numerical model predictions of the erosion and deposition patterns inferred from the convergence of the third-order horizontal wind velocity field at a horizontal near-surface plane, a) $y = 0.25$ m for the full-scale building, and b) $y = 0.015$ m for the small-scale building. The wind direction is from the left and perpendicular to the front face of the buildings. The white lines are zero contours.

As shown by the yellow to red shaded colors in Figure 2.8 (both small-scale and full-scale buildings), the highest negative values of the convergence of the third-order horizontal near-surface velocity field occur in a small area around the upwind corners of the building, indicating this location is prone to erosion in case of a moveable bed and the most intensive amount of erosion is expected to happen there. Figures 2.9a-d show erosion undercutting around the upwind edges of the full-scale container at beach, which is the same pattern as what is predicted based on the numerical model results. Note that the upwind scour zone in front of the building is more strongly developed in the field observations than in the calculated patterns. This might be an effect of topographic feedback, which is absent in the calculations of initial bed level change. The numerical results predict a deposition region upstream of the building (blue shaded colors). Furthermore, two deposition tails starting from some distance away from the lateral sides of the building to downstream of the building form. The field observations given in Figures 2.9c-f show the same deposition region

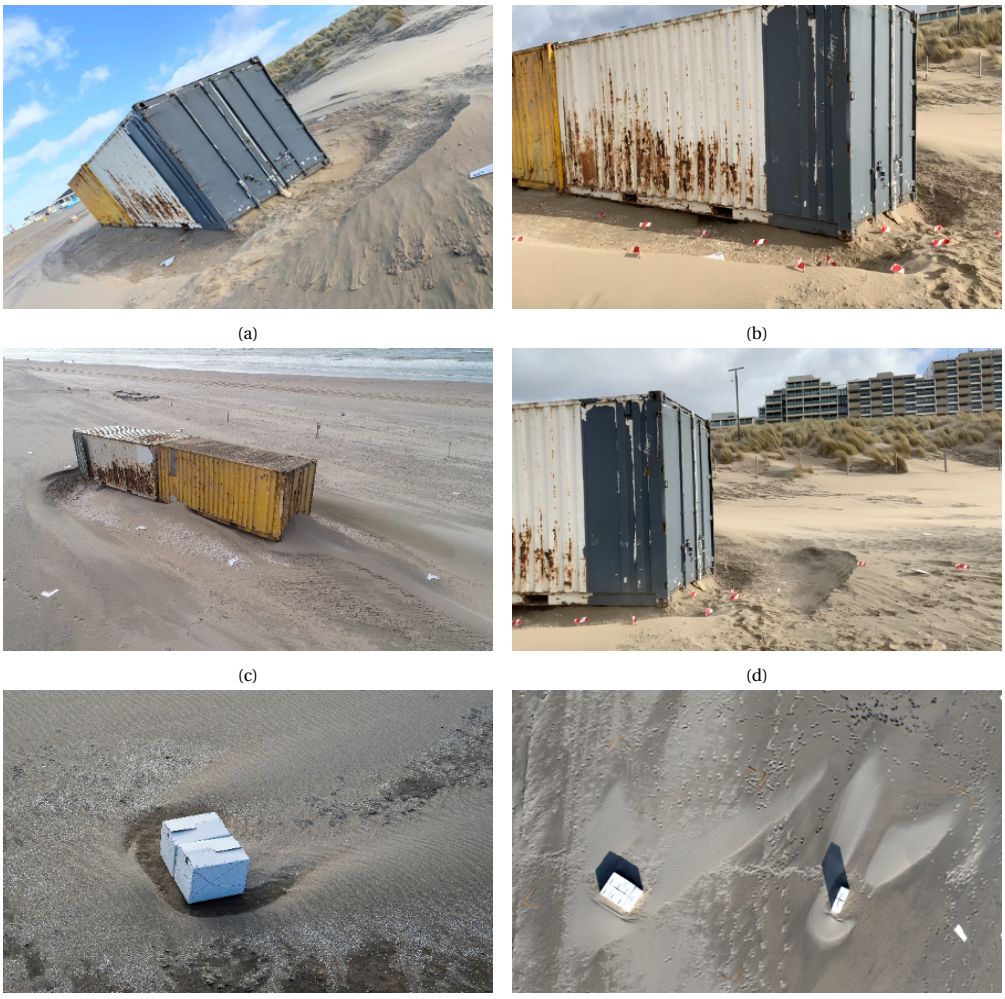

(a) (b) (c) (d) (e) (f)

Figure 2.9: Field observations of erosion and deposition patterns around a a-d) full-scale model at Noordwijk beach, and e, f) small-scale models at De Zandmotor beach, the Netherlands. The arrows show the wind directions. (Figures c, e and f were obtained from Poppema et al. (2021)).

with lighter colored sand upwind of buildings, which is accompanied with two tails that are formed at some distance from the sidewalls of the building and extended to some extent downstream of the building. It is also seen in both numerical model results and field observations, that erosion happens directly along the lateral sides of the building, bounded on the outside by the inner edges of the deposition tails. The above comparisons show that there is a quite good qualitative agreement between observed and modeled erosion and deposition patterns. This provides support for our assumption that the convergence of the third-order

horizontal wind velocity field at a near-surface plane is a suitable proxy for predicting bed level change. Furthermore, the small-scale and large-scale numerical simulations qualitatively show the same patterns of bed morphology, indicating that the overall erosion and deposition patterns are not affected by the scale of the simulation. Therefore, the results of this study are applicable for full-scale buildings at the beach. It is also noteworthy that the erosion and deposition patterns both in the model as well as in the field develop slower for the larger scale buildings. Furthermore, the actual rates of erosion and deposition around buildings depend on the proportionality coefficient in Eq. 2.1. It should be noted that the shape and the dimension of the erosion and deposition patterns around buildings do not depend on the proportionality coefficient.

2.3.2.2. RELATION BETWEEN BUILDING DIMENSIONS AND PATTERNS OF WIND-DRIVEN BED LEVEL CHANGE

THE results of the convergence of the third-order horizontal wind velocity field at a near-surface plane are derived for the previously mentioned simulations specified in Table 2.2. The impact of building length on bed morphology is investigated using Figure 2.10. The two deposition tails that form at some distance from the lateral sides of the building to downstream increase in length, while the deposition rate decreases with increasing building length (see the blue-shaded colors with positive convergence). Furthermore, the eroding regions that occur between the lateral sides of the building and the inner boundary of the deposition tails increase in size when the building length increases (see the zero contour lines). The overall results show that the impact of building length on the convergence pattern of the third-order horizontal near-surface velocity field around the building is small. Therefore, it is expected that the magnitude of the building length does not have a large effect on the bed morphology that develops around the building.

Figure 2.11 shows the impact of building width on bed morphology. The figure shows that for all five tested building widths, the most intensive erosion is expected to happen around the upwind edges of the building. The results show that when the building width increases, the spatial extent of the deposition region in front of the upwind face of the building increases too, and the two deposition tails become slightly longer and wider. The rate of deposition however slightly decreases as the building becomes broader, both in front of the building and in the deposition tails. In addition, the deposition rate just behind the leeward face of the building slightly increases as the building width increases (see the small areas with darker blue-shaded colors just behind the building). It is also noteworthy that, initially the erosion is maximum at the centerline behind the building. However, as the building gets wider, the maximum erosion splits and the erosion rate at the centerline reduces in magnitude and regions of deposition start to form.

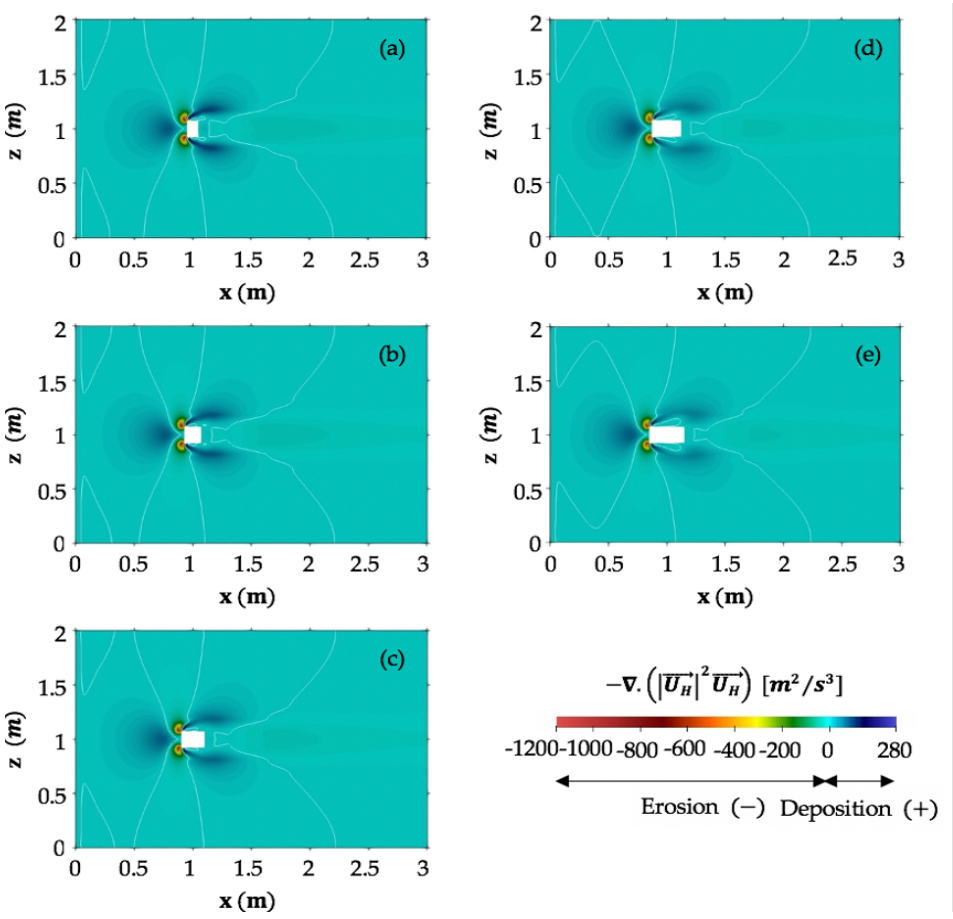

Figure 2.10: The Impact of building length on erosion and deposition patterns inferred from the convergence of the third-order horizontal wind velocity field at a near-surface plane, $y = 0.0125$ m. The building width and height are $w_0^{"}$ and $h_0^{"}$, respectively. The building length, $l^{"}$, is varied as a) $l_0^{"}$, b) $1.5l_0^{"}$, c) $2l_0^{"}$, d) $2.5l_0^{"}$, and e) $3l_0^{"}$.

The impact of building height on bed morphology is investigated using Figure 2.12. Results show that the areal extent of the upwind erosion around the windward edges of the building increases with increasing building height. Furthermore, it is revealed that an increase in building height leads to a substantial reduction in the deposition rate upwind of the building. However, the area with deposition (darker blue-shaded colors) in front of the building increases in spatial extent with increasing building height. The downstream and lateral extension of the two deposition tails increases when the building becomes taller. These implications can be explained by Figures 2.7a-e, where the higher wind velocity magnitudes occur around the upwind edges and lateral sides of the taller building. This higher-speed wind flow erodes more sediment particles upwind the building and carries them for a longer

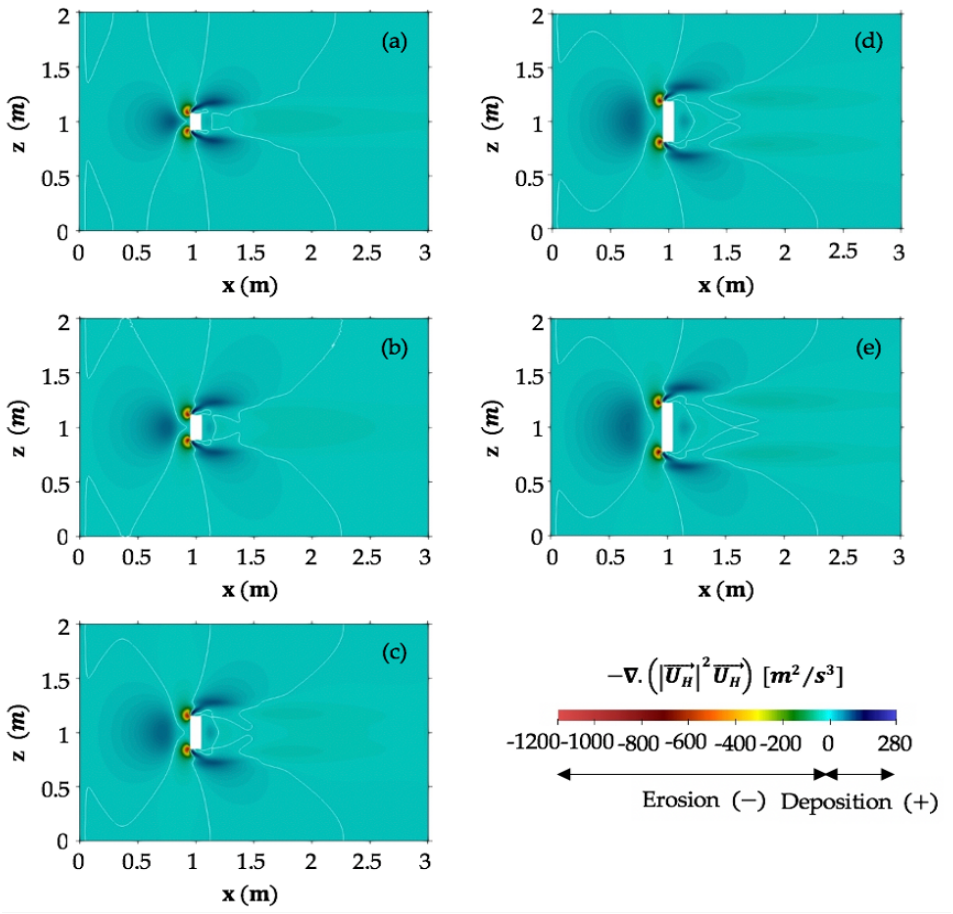

Figure 2.11: The Impact of building width on erosion and deposition patterns inferred from the convergence of the third-order horizontal wind velocity field at a near-surface plane, $y = 0.0125$ m. The building length and height are $l_0^{"}$ and $h_0^{"}$, respectively. The building width, $w^{"}$, is varied as a) $w_0^{"}$, b) $1.5w_0^{"}$, c) $2w_0^{"}$, d) $2.5w_0^{"}$, and e) $3w_0^{"}$.

distance downstream of the building. Therefore, it is probable that when the building increases in height, a shift occurs from mainly sedimentation in front of the building to mainly sedimentation in the tails. In addition, Figure 2.12 shows that the rate of sand accumulation in a small area just behind the leeward face of the building slightly increases when the building height increases.

2.4. DISCUSSION

IN the present study, a CFD model using OpenFOAM was developed to investigate the impacts of building dimensions, specifically building length, width and height on near-

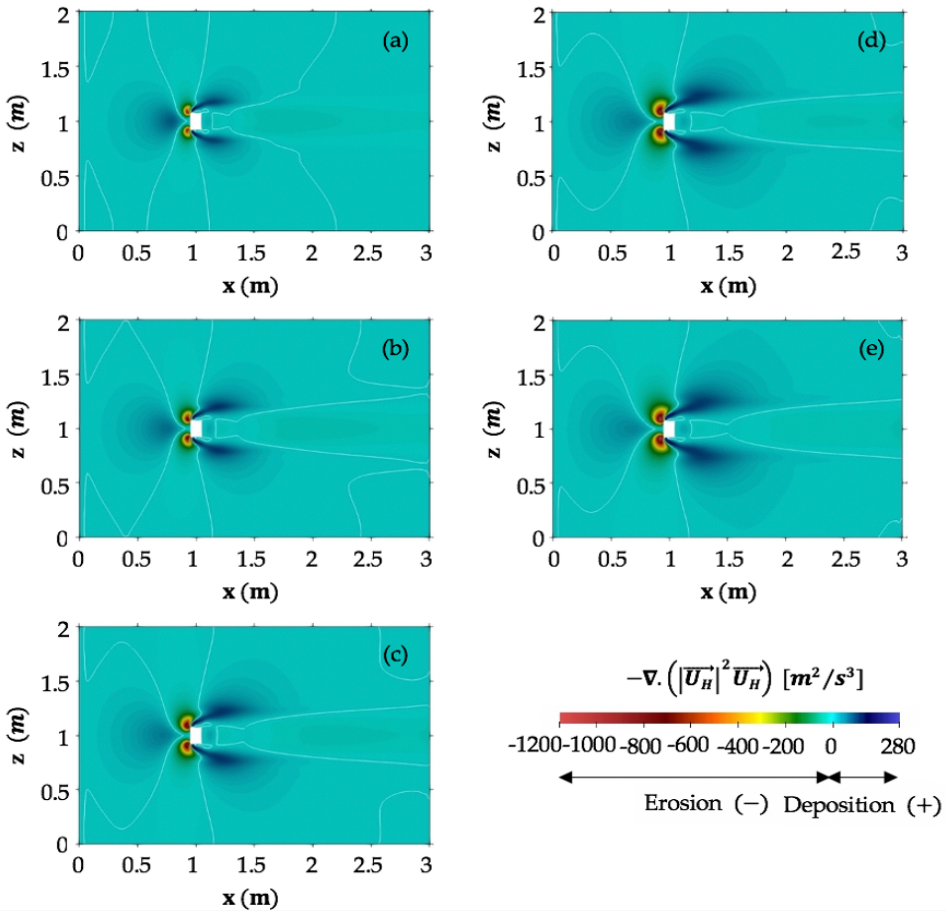

Figure 2.12: The Impact of building height on erosion and deposition patterns inferred from the convergence of the third-order horizontal wind velocity field at a near-surface plane, $y = 0.0125$ m. The building length and width are $l_0^"$ and $w_0^"$, respectively. The building height, $h^"$, is varied as $h_0^"$, $1.5h_0^"$, $2h_0^"$, $2.5h_0^"$, and $3h_0^"$.

surface airflow patterns and bed morphology. The numerical results of the flow field around the building were consistent with the observed flow patterns by Martinuzzi and Tropea (1993) and Leitl and Schatzmann (2010). Similar to the observations by Martinuzzi and Tropea (1993), we found that the size of the near-bed recirculation region in front of the building increases with increasing building width. This can be realized by comparing the length of the local peaks shown in Figure 2.6h. Furthermore, the results of the present study shown in Figure 2.6f, indicates that the downstream reattachment length increases linearly with building width, which is consistent with the findings by Fackrell (1984) and Martinuzzi and Tropea (1993). It should be noted that these findings are based on tested simulations with certain range of width-to-height aspect ratio up to about four, $w^" / h^" \approx 4$.

For the bed surface of the numerical domain, representing a sandy bed, a uniform aerodynamic roughness length, y_0, was assumed based on the wind-tunnel experiments performed by Leitl and Schatzmann (2010). This assumption leads to some inconsistencies with the real condition on the beach that can be considered as the model limitations. On dry enough parts of the beach, sand ripples can form over time under windy conditions, changing the bed roughness and therefore the near-surface airflow changes. However, the good agreements between the model predictions of the erosion and deposition patterns with field observations indicate that ripples do not affect the overall patterns, but they might only modify the spatial extents.

The convergence of the third-order horizontal near-surface wind velocity field was used in this study as a proxy for initial bed level change, because in commonly used sediment transport models the sediment transport rate is assumed to be proportional to the third-order velocity field. Strictly speaking, this assumption is only valid for a situation with transport limited conditions, however on the beach also supply limited conditions occur due to effects of moisture (Delgado-Fernandez, 2010; Nolet et al., 2014; Hoonhout and De Vries, 2019) which may affect the rate at which bed level changes develop. Moisture may affect the amount of sediment in transport approaching the building. This may specifically affect the rate at which deposition patterns around a building develop. In the extreme condition, if no sediment is in transport at all due to very wet condition, no deposition patterns can develop because there is no sediment in the airflow. Furthermore, moist beach surface around the building itself may affect the rate at which building induced erosion occurs, hence it takes more time for erosive features to develop. In addition, in this study, the threshold wind speed was not taken into account. It should be noted that if the wind speed becomes less than the threshold wind speed at which the sediment particles start moving, no sediment transport will happen. Figure 2.13 shows the results of the convergence of the third-order horizontal wind velocity field at a near-surface plane when the wind approaches the building at higher wind velocity magnitude, u_{ref} = 17 m/s (compared to u_{ref} = 6 m/s in Figure 2.8a). The results show that at higher wind speeds where the majority of the domain is well above the threshold wind speed, the similar erosion and deposition patterns develop. It should be noted that the rate of development of patterns increases with increasing the wind velocity magnitude (compared to Figure 2.8a).

McKenna Neuman and Bédard (2015) showed that the fluid perturbation and the system of vortices that develop around buildings depend on the integration between both buildings and the bed surface. In the present study, we used steady airflow patterns around buildings to infer initial effects on bed morphology, hence morphological feedback was not taken into account in this approach. Nevertheless, the erosion and deposition patterns predicted by the numerical model showed good agreement with field observations around the full-scale

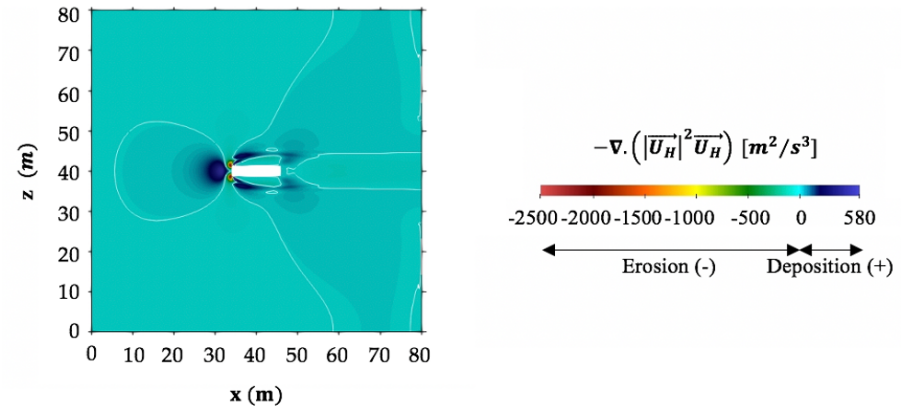

Figure 2.13: Numerical model predictions of the erosion and deposition patterns inferred from the convergence of the third-order horizontal wind velocity field at a horizontal near-surface plane, $y = 0.25$ m, around the full-scale building. The reference wind velocity magnitude is 17 m/s at a reference height of 1.8 m. The wind direction is from the left and perpendicular to the front face of the building. The white lines are zero contours.

model and the small-scale model at the beach. The model results showed a considerable erosion around the windward edges of the building, extending less intensively than at the edges along the lateral sides. In addition, the deposition region in front of the upwind face of the building and two deposition tails starting away from the lateral sides of the building and extending downstream of the building occur in all simulations. These findings are similar to the observations by Iversen et al. (1990), Iversen et al. (1991), Tominaga et al. (2018) and Poppema et al. (2021).

To consider the impact of scaling on numerical results shown in this study, the erosion and deposition patterns between a full-scale model and a small-scale model at the beach were compared qualitatively. The comparisons showed that the erosion and deposition patterns that develop around the buildings are not influenced when the scale of the simulation increases. However, the rate of growth of the patterns decreases with increasing the scale of the simulation. This is also valid for small-scale and full-scale experimental models at the beach.

The initial morphological changes predicted by the model show a central downwind deposition just behind the leeward face of the building starts to appear when the building width increases (see Figure 2.11). The reason is that, two horizontal counter-rotating vortices become stronger as the building width increases (see Figures 2.6a-e). These two vortices push the air towards the centerline behind the building. The air gets pushed upward resulting in an upward component of the wind. On the other hand, the vertical recirculation just behind the building generates a downward motion at the position above the deposition region. For

wider building, the upward effect of the two horizontal vortices becomes stronger than the downward effect of the vertical vortex which leads to a net upward flow. The net upward flow results in positive convergence of third-order horizontal velocity field at a near-surface plane. Therefore, the erosion and deposition patterns show the formation of a deposition region just behind the leeward face of the wider building.

In this paper we studied buildings on a flat sand surface, whereas on an actual beach buildings are often built in front of a dune. Although dune topography was not included in the simulations, some preliminary implications of building dimensions for sand supply from the beach to the dunes may be formulated from the presented results. The convergence patterns in the near-surface flow field induced by the building demonstrate that ambient sand transport will be captured by the building, both upwind and in two downwind tails. The rate of deposition in the two tails varies with building dimension. If we assume these trends prevail also in the presence of dune topography downwind of the building, such higher rate of deposition would mean an increasingly higher deposition on the dune front at the tail location. From our results of the deposition patterns downstream of the buildings, it can then be derived that the highest building is expected to give the strongest local increase in deposition at the dune front and the longest building the least. Note this holds for situations with predominantly onshore wind. The ridge-like deposition in front of the wider building increases in size as the building becomes broader. In ad-dition, the eroding region around the windward edges of the building increases substantially with increasing the building height. These might lead to building's miss-functioning and probably tilting that forces the owners of the beach buildings to consider measures to smoothen the surface or prevent the development of these patterns.

2.5. CONCLUSIONS

IN this study, the impacts of building dimensions on near-surface airflow patterns were investigated as well as the implications for bed morphology in case of a surrounding sandy bed. Specifically, three building characteristics were studied: the building length parallel to the incident wind direction, building width perpendicular to the incidence wind direction and building height. For this purpose, a CFD model using OpenFOAM was developed. The numerical model predictions showed satisfactory agreement with wind-tunnel data of vertical and horizontal wind velocity profiles in the vicinity of the scale model of buildings, providing confidence in the capability of the model to predict the detailed airflow patterns around an isolated building at the beach.

Using this model, a systematic investigation revealed the effects of building length, width and height on airflow patterns at a horizontal plane close to the bed. The results on the

relation between building dimensions and near-surface airflow patterns were consistent with those found in Iversen et al. (1990), Iversen et al. (1991) and Martinuzzi and Tropea (1993), where width and height of the building were most influential in the extent and nature of near-surface airflow patterns around the building and downwind length least. Only the length of the recirculation region just behind the leeward face of the building decreases slightly when the building increases in length. This was consistent with findings in Fackrell (1984). By focusing on near-surface flows both in front of the building and down-stream of the building, our simulations further revealed that a wider building disturbs a longer and wider region both in front of the building and downstream of the building. The distance at which the upwind deceleration of the airflow starts as it approaches the building increases with building width. The numerical results presented in this study highlighted that with increasing building height, the length of the two counter-rotating vortices just behind the leeward face of the building increases considerably, and with it the length of the recirculation region. Furthermore, with taller buildings it takes a longer distance for the near-surface wind leeward of the building to increase its speed back to the undisturbed wind velocity magnitude.

The convergence of the third-order horizontal near-surface wind velocity field was used as a proxy for sediment transport rate. Although inferred erosion and deposition patterns technically only relate to initial bed level changes, it was found that these compared well to those observed around a full-scale model and a small-scale model at Noordwijk beach and De Zandmotor beach in the Netherlands (Poppema et al., 2021).

As for the near-surface airflow patterns, also the initial bed morphology was most dependent on the building width normal to the incidence wind direction as well as the building height, and least on the length of the building parallel to the incidence wind direction. In addition, it was found that for all studied building dimensions, the most intensive erosion is expected to happen around the upwind edges of the building, where the undercutting was observed in the field experiments. The initial bed morphology revealed that the areal extent of these eroding regions directly adjacent to the windward edges of the building increases when the building becomes taller. By focusing on the initial deposition patterns around buildings, the numerical simulations highlighted that the deposition tails downstream of the buildings develop more slowly as the building length increases. Furthermore, sediment deposition that occurs in front of the upwind face of the building becomes larger in spatial extent, and the length of the two deposition tails downstream of the building slightly increases as the building becomes broader. The deposition rate both in the ridge-like deposition in front of the building and in the deposition tails slightly decreases with increasing building width. This implies that the wider the building, the broader and shallower the deposition region in front of the windward face of the building. A small area of sand accumu-

lation appears just behind the leeward face of the building as the building width increases. The numerical results further revealed that with increasing building height the sedimentation rate further upwind of the building decreases, while it increases in the downwind tails.

ACKNOWLEDGMENTS

This research is part of the ShoreScape project, which is a joint research project of the University of Twente and Delft University of Technology. ShoreScape focuses on sustainable co-evolution of the natural and built environment along sandy shores.

We would like to thank Dr. Sander Vos for inviting us in the Noordwijk experiments and Ir. Daan Poppema for discussions and the photo of his scale model experiments at the Zandmotor.

2.A. APPENDIX: DEVELOPMENT OF THE NUMERICAL MODEL

2.A.1. GOVERNING EQUATIONS

IN this study, a three-dimensional numerical model is developed using OpenFOAM. The wind flow in this model is considered as incompressible, since for the flow with Mach numbers less than 0.3, the change in flow density is negligible and the divergence of flow velocity can be considered zero (Ferziger and Peric, 2002). The Mach number is a dimensionless parameter, defined as the ratio of the speed of flow to the speed of sound in the surrounding flow (Hoonhout and De Vries, 2019). The Mach number of 0.3 corresponds to the airflow with the speed of about 100 m/s in its normal condition, which is typically greater than the wind speed (Shapiro, 1953). In addition, considering the Reynolds number criteria, the wind flow in this study is assumed fully turbulent. Therefore, among all available OpenFOAM solvers for incompressible flows, the so-called simpleFoam solver is selected, which is recommended for steady state simulation of turbulent flows.

The simpleFoam algorithm solves the Reynolds-averaged Navier-Stokes (RANS) equations for turbulent flows using the finite volume method (FVM). The RANS method employs the Reynolds decomposition of flow variables into mean and fluctuating parts, and solves the additional Reynolds stresses that appear in the momentum equations of flow using a turbulence model (Versteeg and Malalasekera, 1995; Ferziger and Peric, 2002; Moukalled et al., 2016). Considering that the conservation of energy is only applied for compressible flows, the governing equations of the three-dimensional flow field can be expressed by continuity and momentum equations that can be written in their steady states as follows:

$$\vec{\nabla} \cdot \vec{U} = 0 \tag{2.A.1}$$

$$\vec{\nabla} \cdot (\vec{U} \otimes \vec{U}) = -\vec{\nabla} p_k + \vec{\nabla} \cdot (\nu_{eff} \vec{\nabla} \vec{U}) \tag{2.A.2}$$

where $\vec{U} = (u, v, w)$ [m/s] is the three-dimensional flow velocity vector; p_k [m^2/s^2] is the kinematic pressure, defined as the ratio of the static pressure, p_s [Pa], to the flow density, ρ [kg/m^3]; ν_{eff} [m^2/s] is the effective kinematic viscosity, defined as the sum of the kinematic viscosity of the flow, ν [m^2/s], and the turbulent (eddy) kinematic viscosity, ν_t [m^2/s], which is calculated from the turbulence model. In the present study, the kinematic viscosity of the air, ν, is considered as 1.4×10^{-5} m^2/s.

Although Eqs. 2.A.1 and 2.A.2 introduce 4 equations and 4 unknowns (u, v, w, p_k), they are difficult to be solved numerically. The main reason is that there is an equation for each com-

ponent of the flow velocity, but there is no equation for the pressure. It should be noted that the continuity equation plays a role of restriction for velocity components, meaning that the computed velocity components from Eq. 2.A.2 must satisfy the Eq. 2.A.1. In addition, the wind flow in this study is considered as incompressible, therefore the equation of state cannot be used to compute the pressure, as the flow density and temperature are assumed constant. The next reason is that the convective term in the momentum equation, $\vec{\nabla} \cdot (\vec{U} \otimes \vec{U})$, is non-linear which makes the solution of abovementioned equations more complex. The simpleFoam solver uses the SIMPLE (semi-implicit method for pressure-linked equations) algorithm to solve the continuity and momentum equations.

2.A.1.1. SIMPLE ALGORITHM

THE SIMPLE algorithm uses an iterative procedure, where the intermediate velocity field is first calculated by solving the momentum equation for an initial guessed pressure field. The intermediate velocity field does not satisfy the continuity restriction. Deriving and solving the pressure equation, the so-called Poisson equation, from the continuity and momentum equations result in a pressure corrector that is used for adjusting the inter-mediate velocity field and obtaining a new velocity field, that satisfies the continuity restriction after doing several iterations (Caretto et al., 1973; Versteeg and Malalasekera, 1995; Moukalled et al., 2016). The first step to initiate the SIMPLE approach is to express the momentum equation, Eq. 2.A.2, in the matrix form as follows:

$$A\vec{U} = -\vec{\nabla} p_k \tag{2.A.3}$$

where A is the known matrix of coefficients that its components are calculated using the discretization of the partial differential terms in the momentum equation. Note that the nonlinearity of the advection terms will involve some kind of linearization method. The above equation includes $3n$ equations, where n is the total number of control volumes and each equation is written for the centroid of each control volume. The second step is to decompose the matrix of coefficients, A, into diagonal and non-diagonal components:

$$A\vec{U} = B\vec{U} - C \tag{2.A.4}$$

where B and C are the known diagonal and non-diagonal components of matrix A, respectively. Substituting Eq. 2.A.4 into Eq. 2.A.3 and rearranging the momentum equation in terms of the flow velocity yields the following equation:

$$\vec{U} = B^{-1}C - B^{-1}\vec{\nabla} p_k \tag{2.A.5}$$

The third step is to derive the pressure equation, Poisson equation, by substituting the above equation into the continuity equation, Eq. 2.A.1, that can be written in the following form:

$$\vec{\nabla} \cdot (B^{-1} \vec{\nabla} p_k) = \vec{\nabla} \cdot (B^{-1} C) \tag{2.A.6}$$

In the next step, the iterative procedure starts with an initial guess for the pressure field, p_k^*. Using the guessed pressure field, the momentum equation is solved to compute the intermediate velocity field, $(\overrightarrow{U^*}) = (u^*, v^*, w^*)$. This intermediate velocity field does not satisfy the continuity restriction until the solution has been converged. The correct pressure field, p_k^n, is then obtained by solving the Poisson equation. Subsequently, the pressure corrector, $p_k^{'}$, is calculated by subtracting the guessed pressure field from the correct pressure field, $p_k^{'} = p_k^n - p_k^*$. Then, the velocity field is updated, $\overrightarrow{U^n} = (u^n, v^n, w^n)$, using the momentum equation and is checked for the continuity restriction. If the updated velocity field does not satisfy the continuity restriction, a new iteration cycle will start, using $p_k^{'}$ as the initial guess and $\overrightarrow{U^n}$ for the calculation of the matrix of coefficient. The iteration continues until convergence occurs. In this case, the continuity restriction is satisfied in each control volume of the computational domain and the pressure corrector becomes zero (Caretto et al., 1973).

2.A.2. TURBULENCE MODELLING

USING the RANS method to solve the Navier-Stokes equations introduces additional unknowns, so-called Reynolds stresses, into the main equations. To close the set of equations, a turbulence closure model must be applied. In this study, the well-known standard $k-\varepsilon$ model proposed by Launder and Spalding (1974) is used. The standard $k-\varepsilon$ model is a two-equation model based on the Boussinesq approximation. It assumes that the impacts of turbulence on flow can be expressed by an increased kinematic viscosity, and the additional Reynolds stresses can be related to the mean velocity gradients of flow by the turbulent (eddy) kinematic viscosity, ν_t (Ferziger and Peric, 2002). This turbulent kinematic viscosity can be formulated by the turbulence kinetic energy, k [m^2/s^2], and its rate of dissipation, ε [m^2/s^3], as follows (Richards and Hoxey, 1993):

$$\nu_t = C_\mu \frac{k^2}{\varepsilon} \tag{2.A.7}$$

where C_μ [-] is a dimensionless constant.

In the standard $k-\varepsilon$ model, the k and ε are computed from their transport equations that can be written in their steady states as follows (Versteeg and Malalasekera, 1995; Moukalled

et al., 2016):

$$\vec{\nabla} \cdot (k\vec{U}) = \vec{\nabla} \cdot (\nu_{eff,k} \vec{\nabla} k) + \frac{P_k}{\rho} - \varepsilon \tag{2.A.8}$$

$$\vec{\nabla} \cdot (\varepsilon\vec{U}) = \vec{\nabla} \cdot (\nu_{eff,\varepsilon} \vec{\nabla} \varepsilon) + C_{\varepsilon 1} P_k \frac{\varepsilon}{\rho k} - C_{\varepsilon 2} \frac{\varepsilon^2}{k} \tag{2.A.9}$$

where $C_{\varepsilon 1}$ [-] and $C_{\varepsilon 2}$ [-] are dimensionless constants; P_k [kg/m/s^3] is the production of turbulent kinetic energy; and $\nu_{eff,k}$ [m^2/s] and $\nu_{eff,\varepsilon}$ [m^2/s] are defined as below:

$$\nu_{eff,k} = \nu + \frac{\nu_t}{\sigma_k} \tag{2.A.10}$$

$$\nu_{eff,\varepsilon} = \nu + \frac{\nu_t}{\sigma_\varepsilon} \tag{2.A.11}$$

where σ_k [-] and σ_ε [-] are dimensionless constants. The first and second terms in Eqs. 2.A.8 and 2.A.9 represent the transport of k or ε by advection and diffusion, respectively; while the last two terms show the rate of production and the destruction of k or ε, respectively. The empirical model coefficients for the standard $k-\varepsilon$ model are given in Table 2.A.1 (Launder and Spalding, 1974; Launder and Sharma, 1974). It should be noted, in the SIMPLE algorithm, the transport equations of k and ε are solved just after computing the updated velocities and the check for the continuity restriction. The turbulent (eddy) kinematic viscosity, ν_t, is then updated and be used in the momentum equation for the next iteration cycle.

Table 2.A.1: Values of the empirical constants in the standard $k-\varepsilon$ model (Launder and Spalding, 1974; Launder and Sharma, 1974).

Parameter [-]	**Value**
C_μ	0.09
$C_{\varepsilon 1}$	1.44
$C_{\varepsilon 2}$	1.92
σ_k	1.00
σ_ε	1.30

2.A.3. BOUNDARY CONDITIONS AND INITIAL INTERNAL FIELDS

CONSIDERING neutral stratification conditions, fully-developed profiles of mean wind speed, U, and turbulence quantities including turbulence kinetic energy, k, and turbulence dissipation rate, ε, are applied at the inlet of the computational domain shown in Figure A1, using the following equations proposed by Richards and Hoxey (1993):

$$U(x=0,y,z) = \frac{u^*}{\kappa}\ln(\frac{y-y_g+y_0}{y_0}) \tag{2.A.12}$$

$$k(x=0,y,z) = \frac{{u^*}^2}{\sqrt{C_\mu}} \tag{2.A.13}$$

$$\varepsilon(x=0,y,z) = \frac{{u^*}^3}{\kappa(y-y_g+y_0)} \tag{2.A.14}$$

where u^* [m/s] is the friction velocity; κ [-] is the von Karman constant defined as 0.41 in OpenFOAM; y [m] is the vertical coordinate; y_g [m] is the minimum y-coordinate or the ground level; y_0 [m] is the aerodynamic roughness length; and C_μ is the dimensionless constant in the standard $k-\varepsilon$ model defined as 0.09.

The height of the computational domain is significantly smaller than the atmospheric boundary layer (ABL) height, therefore the friction velocity in Eqs. 2.A.12-2.A.14 can be assumed constant with height (Blocken et al., 2007), and is calculated using the following equation proposed by Richards and Hoxey (1993):

$$u^* = \frac{\kappa u_{ref}}{\ln(\frac{y_{ref}+y_0}{y_0})} \tag{2.A.15}$$

where u_{ref} [m/s] is the reference velocity at a reference height, y_{ref} [m].

In the present study, the values of the ABL parameters used in inlet profiles are selected based on the wind-tunnel experiments performed by Leitl and Schatzmann (2010). These values are given in Table 2.A.2.

The analytical inlet profiles of mean wind speed, U, turbulence kinetic energy, k, and turbulence dissipation rate, ε, proposed by Richards and Hoxey (1993) are shown in Figure 2.A.1.

A zero-gauge pressure boundary condition is applied at the outlet of the computational domain. The no-slip boundary condition for the velocity is used for the bottom of the com-

Table 2.A.2: Values of the atmospheric boundary layer parameters used in inlet profiles (Leitl and Schatzmann, 2010).

Parameter	Value
y_g [m]	0.0000
y_0 [m]	0.0007
u_{ref} [m/s]	6.0000
y_{ref} [m]	0.5000

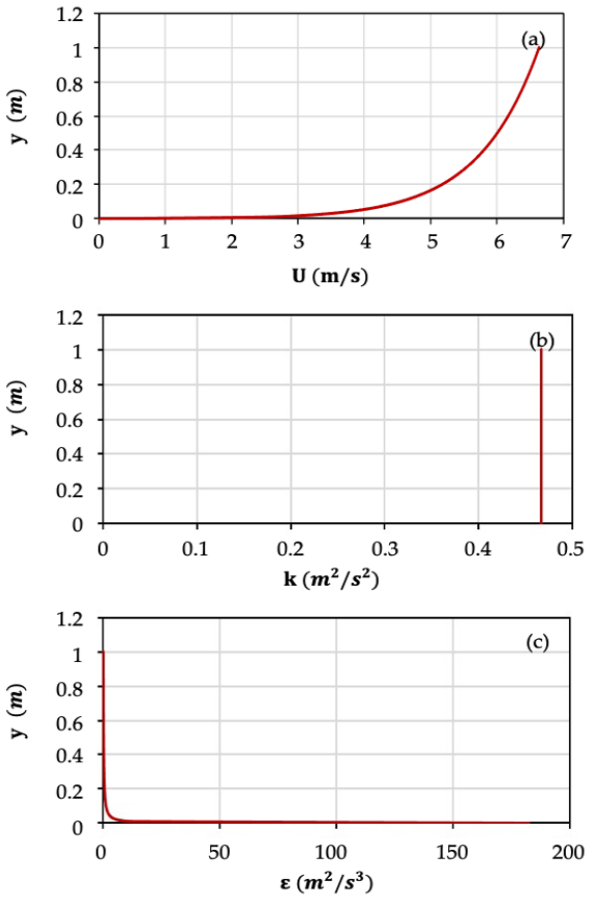

Figure 2.A.1: The analytical inflow conditions of a) mean wind speed, b) turbulence kinetic energy, k, and c) turbulence dissipation rate, ε.

putational domain and the building walls. It assumes that the speed of the wind flow in direct contact with the bottom of the domain and the walls of the building is identical to the

speed of movement of these boundaries, which is equal to zero. Furthermore, the free-slip boundary condition is used for the top and lateral boundary surfaces of the computational domain for all scalar and vector quantities.

The initial internal fields for pressure and velocity are chosen zero, while the initial internal fields for turbulence kinetic energy and turbulence dissipation rate are calculated using the following equations (Launder and Spalding, 1974; Richards and Hoxey, 1993; Versteeg and Malalasekera, 1995):

$$k = \frac{1}{2}(u'^2 + v'^2 + w'^2) \tag{2.A.16}$$

$$\varepsilon = \frac{C_\mu^{0.75} k^{1.5}}{l} \tag{2.A.17}$$

where u' [m/s], v' [m/s] and w' [m/s] are fluctuating components of velocity in the x, y and z directions, respectively; C_μ is the dimensionless constant in the standard $k-\varepsilon$ model defined as 0.09; and l [m] is the turbulence length scale or the characteristic length for the macroscale of turbulence.

Assuming an isotropic inlet turbulence, $u' = v' = w'$, and estimating the fluctuations to be 5 percent of the reference velocity at the inlet of the computational domain, and selecting $l = 0.32$ m for the turbulence length scale based on the wind-tunnel experiments performed by Leitl and Schatzmann (2010), the initial internal values of the turbulence kinetic energy, k, and the turbulence dissipation rate, ε, are calculated as 0.135 m^2/s^2 and 0.0255 m^2/s^3, respectively.

2.A.4. WALL FUNCTIONS

AS mentioned in Appendix 2.A.3, the vertical wind velocity profile changes from zero at the bottom of the computational domain, due to the no-slip boundary condition, to its free stream value far away from the wall (see Figure 2.A.2a). The largest gradients of the velocity occur in the near-wall region, where the velocity profile becomes quite steep. To accurately simulate the flow behavior close to the wall, it is important to precisely capture the velocity variations in the near-wall region. Using a second-order accurate finite volume discretization method in the OpenFOAM model, the flow features are calculated for the cell centers and the variation of variables is linear between the cell centroids. Therefore, the standard method to accurately simulate the flow in the near-wall region is to gradually decrease the mesh size when approaching the wall boundary (Bredberg, 2000; Fluent, 2013) (see Figure 2.A.2b). Applying a very fine mesh close to the wall significantly increases the

number of cells, that increases the computational time considerably. Furthermore, increasing the mesh resolution normal to the wall results in the formation of cells with high aspect ratios. The skewness of the cells causes poor cell qualities that increases the instabilities of the CFD solution.

An alternative way to accurately resolve the high velocity gradients close to the wall is to replace a single large cell instead of those thin cells in the near-wall region and introduce a function, so-called wall function, to reproduce the high velocity variations between the cell centroid and the wall boundary (Bredberg, 2000) (see Figure 2.A.2c). Using the wall function approach, the number of cells and therefore the computational time decreases considerably. In addition, the stability of the CFD solution increases significantly.

Considering the universal law of the wall based on the experimental measurements of fully developed turbulent channel flows, the variation of dimensionless tangential velocity close to the wall, $U^+ = U/u_\tau$, with the dimensionless distance normal to the wall, $y^+ = yu_\tau/\nu$, is derived. The u_τ [m/s] is the wall friction velocity or the characteristic velocity based on the wall shear stress as the velocity at wall is zero. It can be different from u^*, and is calculated using the following equation (Schlichting, 1961; Blocken et al., 2007):

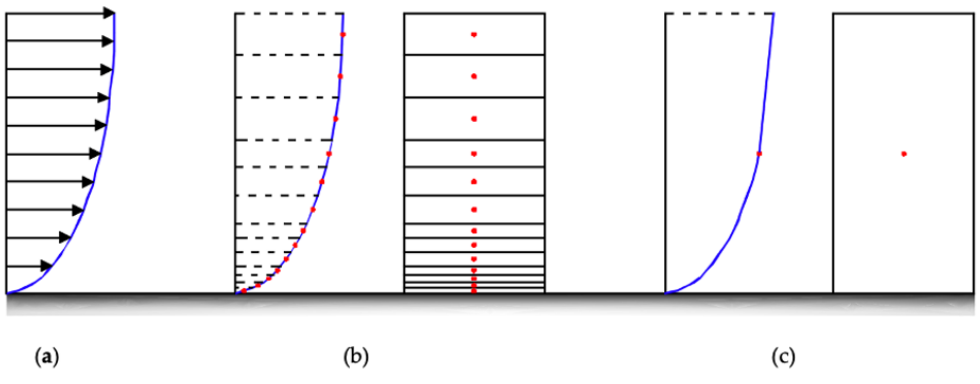

Figure 2.A.2: Methods of simulating wind flow velocity in the near-wall region a) The typical vertical wind velocity profile with high velocity gradients close to the wall, b) Standard linear method, and c) Wall function approach.

$$u_\tau = \sqrt{\frac{\tau_w}{\rho}} \tag{2.A.18}$$

where τ_w [N/m^2] is the wall shear stress; and ρ is the flow density. The near-wall region is then subdivided into three distinct layers as follows (Tennekes and Lumley, 1972; F. M. White, 1991):

- Viscous layer for $0 < y^+ < 5$

- Buffer layer for $5 < y^+ < 30$
- Inertial layer for $30 < y^+ < 200$

Wall functions are empirical functions that are best fitted to the observed flow behavior close to the wall. The standard wall functions are a linear and a logarithmic function that precisely reproduce the flow behavior in the viscous layer and the inertial layer, respectively. These wall functions can be expressed by the following equations (Fluent, 2013; F. Liu, 2016):

$$U^+ = y^+ \tag{2.A.19}$$

$$U^+ = \frac{1}{\kappa}\ln(Ey^+) \tag{2.A.20}$$

where κ is the von Karman constant defined as 0.41 in OpenFOAM; and E [-] is an empirical wall roughness coefficient defined as 9.8 in OpenFOAM. The abovementioned wall functions for viscous and inertial layers intersect in the buffer layer at approximately $y^+ = 11.225$, so-called y^+_{lam} in OpenFOAM. The following conditional statement is then applied in the OpenFOAM model to predict the flow behavior in the near-wall region:

$$U^+ = \begin{cases} y^+ & if\, y^+ \leq y^+_{lam} \\ \frac{1}{\kappa}\ln(Ey^+) & if\, y^+ > y^+_{lam} \end{cases} \tag{2.A.21}$$

It should be noted, the Eq. 2.A.21 cannot precisely predict the flow behavior in the buffer layer, therefore it is not recommended to placing cells in this region.

2.B. APPENDIX: MODEL VALIDATION

IN order to validate the numerical model, the wind-tunnel measurements performed by Leitl and Schatzmann (2010) in the meteorological institute of Hamburg university are compared with the numerical model predictions of the vertical and horizontal wind speed profiles in the vicinity of the building. The atmospheric boundary layer and geometric parameters are selected based on the values presented in Table 2.A.2 and Table 2.2, respectively. The total number of cells in the mesh is approximately 1.64 million, consisting of cells with the length, width and height almost equal to 0.0125 m. The results are then derived from sixteen different sections from which eight are located on the symmetry plane, $z = 0.325$ m, and the other eight a near-surface plane, $y = 0.035$ m, as shown in Figure 2.B.1. The comparisons and RMSE values presented in Figure 2.B.2 and Figure 2.B.3 show satisfactory agreements between the experimental data and the numerical model results. This

shows the capability of the numerical model to predict both vertical and horizontal airflow patterns around the building.

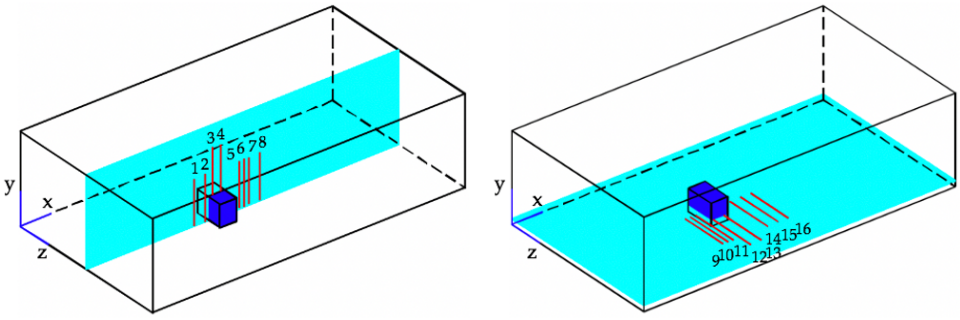

(a) (b)

Figure 2.B.1: Schematic representation of the vertical and horizontal measurement sections locating on the a) symmetry plane, $z = 0.325$ m, and b) a near-surface plane, $y = 0.035$ m.

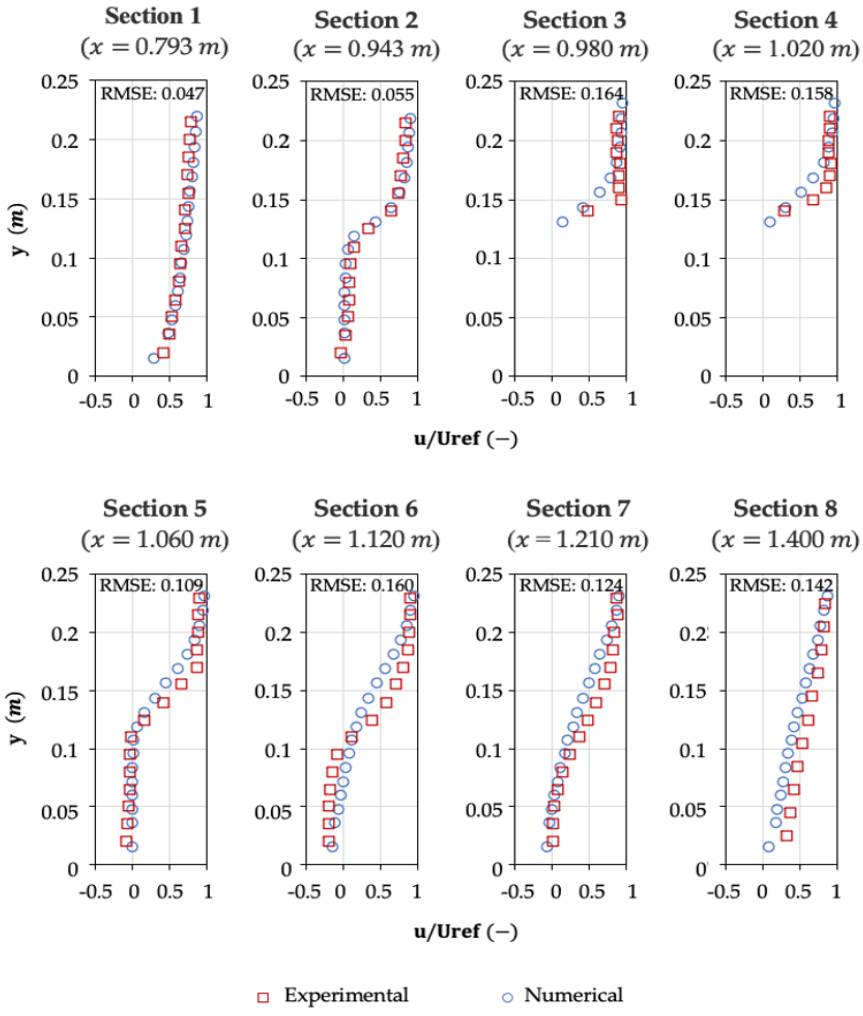

Figure 2.B.2: Comparisons between the wind-tunnel measurements performed by Leitl and Schatzmann (2010) and the numerical model predictions of the vertical velocity profiles derived from eight different sections locating on the symmetry plane, $z = 0.325$ m.

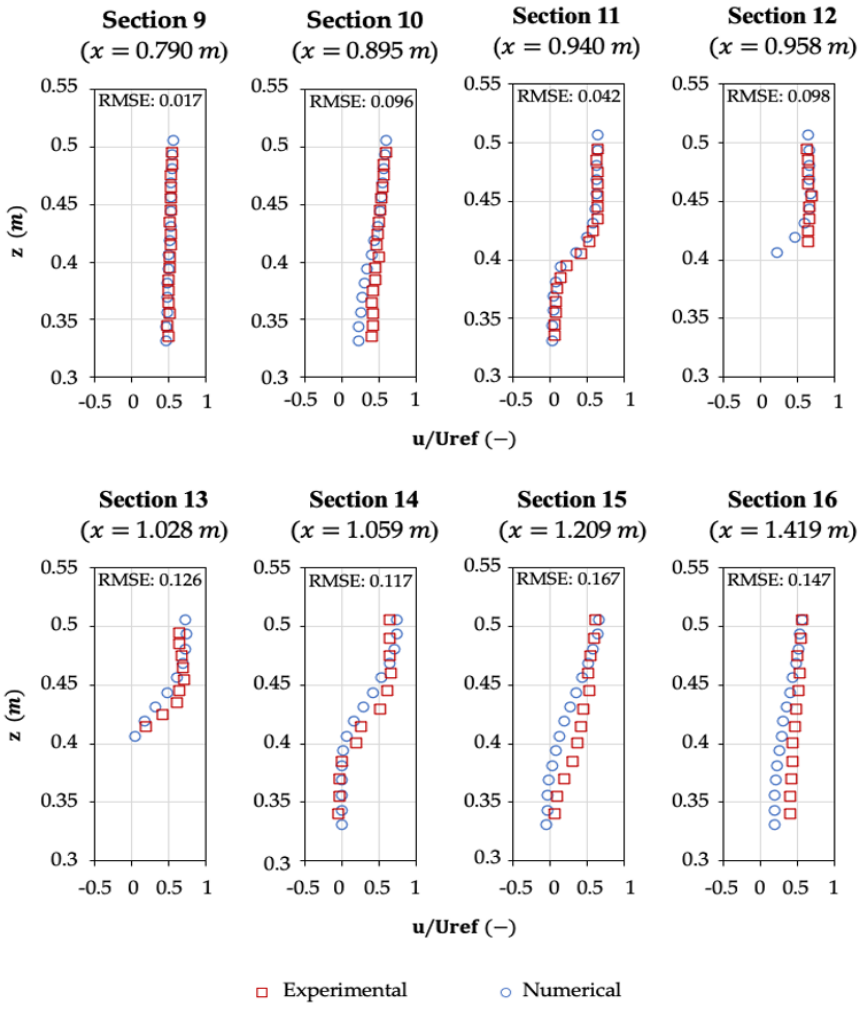

Figure 2.B.3: Comparisons between the wind-tunnel measurements performed by Leitl and Schatzmann (2010) and the numerical model predictions of the horizontal velocity profiles derived from eight different sections locating on a near-surface plane, $y = 0.035$ m. The comparisons are performed for the right half side of the domain, where the building centreline and the lateral face of the building are located at $z = 0.325$ m and $z = 0.400$ m, respectively.

3

THE INFLUENCE OF WIND DIRECTION AND BUILDINGS SPACING ON AIRFLOW PATTERNS, SEDIMENT TRANSPORT PATTERNS AND INITIAL BED MORPHOLOGY

This chapter is published as Pourteimouri, P., Campmans, G. H. P., Wijnberg, K. M. and Hulscher, S. J. M. H. (2023). How wind direction and building spacing influences airflow patterns and sediment transport patterns around a row of beach buildings: A numerical study. *Aeolian Research*, 61, 100867. DOI: 10.1016/j.aeolia.2023.100867

ABSTRACT: Buildings at the beach change the near-bed airflow patterns in the surrounding area. This induces alterations in wind-induced bed shear stress and wind-induced sediment transport which, in turn, affect the bed topography in the vicinity of buildings. Three-dimensional computational fluid dynamics simulations using OpenFOAM have been performed to understand how and to what extent the buildings at the beach influence the sediment transport from the beach to the dunes. Herein, we explicitly account for the positioning of the buildings with respect to each other and the dominant wind direction. Also discussed are the airflow mechanisms that are responsible for sediment transport, and how they alter due to systematic changes in the gap spacing between buildings and the wind incidence angle. Simulations were performed, in which we model flow and initial sediment transport around a repeating row of ten parallel full-scale beach buildings when the gap spacings and wind incidence angles were systematically varied. The horizontal near-bed streamline patterns showed that there is a critical gap spacing, below which the neighboring buildings significantly affect each other. Furthermore, the airflow in the near-wake region behind the row of buildings is quite complex. The shape and the extent to which the sand drifts develop behind the gaps between buildings are largely influenced by the wind direction, relative to the buildings. We also computed the average sediment transport flux along different lines downstream of the buildings. Our findings showed that, depending on the buildings' positioning at the beach, they could have negative effects on dune growth by obstructing the sediment particles from moving downstream, or they could have positive effects on dune growth by steering the airflow and supplying more sediment downstream.

3.1. INTRODUCTION

THE recreational value and attractiveness of sandy beaches worldwide, makes the understanding of the influence that buildings might have in the surrounding area vital. Buildings by the beach such as hotels, holiday cottages, restaurants, sailing and surfing clubs, lifeguard rescue towers and pavilions (Figure 3.1) affect the near-bed wind field due to their size, shape, elevation from the bed, construction materials and their location on the beach (Nordstrom and McCluskey, 1985; Nordstrom, 2000; Jackson and Nordstrom, 2011). The sediment mass transport in sandy environments, such as beaches, depends on complex interactions between near-bed wind field, sediment transport and instantaneous changes in bed morphology (Walker and Nickling, 2002). Therefore, in response to the spatial variations in near-bed flow dynamics due to the protrusion of buildings into the near-bed boundary layer, erosion and deposition patterns develop. These building-induced erosion and deposition patterns might become problematic over a longer time-scale. Buildings change the wind-blown sediment supply moving from the beach towards the dunes and might affect the flood safety functioning of the dunes (Nordstrom and McCluskey, 1984; Nordstrom and Jackson, 1998).

Furthermore, the scouring and sediment trapping around buildings could cause structural malfunction (Jackson and Nordstrom, 2011). A quantitative study on the impact of building spacing in rows of beach houses, and the prevailing wind direction on near-bed wind field as well as erosion and deposition patterns would be of interest for coastal engineers, morphologists, and owners of the buildings. The findings of such a study could provide scientific support for coastal managers to mitigate threats to both buildings and dunes, in addition to minimizing the need for additional preservation measures.

The airflow patterns around cuboid structures, such as buildings, have been studied extensively through experimental measurements and numerical simulations (Hunt et al., 1978; Beranek, 1984; Peterka et al., 1985; Martinuzzi and Tropea, 1993; Shah and Ferziger, 1997; Lakehal and Rodi, 1997; Chou and Chao, 2000; Iaccarino et al., 2003; Gao and Chow, 2005; Yakhot et al., 2006; Pourteimouri et al., 2022). Understanding the aeolian sediment transport and morphological changes around cuboid buildings that are located on movable substrate, e.g. sandy beaches, has been of great interest in previous studies. In case of a sufficiently strong wind, the sediment particles are entrained by the airflow. They strike the windward face of the building, rebound back, and settle in the decelerated flow region at some distance in front of the building where the approaching wind and the reversed flow meet (Bagnold, 1941). The upwind deposition is similar to the so-called echo dunes that also develop in front of the vertical natural obstructions, e.g. cliffs, in sandy environments (Tsoar, 1983; Cooke et al., 1993; Jackson and Nordstrom, 2011; Qian et al., 2011). The sedi-

(a) (b)

(c)

(d) (e)

Figure 3.1: Examples of some buildings at the a, b) Kijkduin, and c, d, e) Katwijk beach, the Netherlands.

ment accumulation in front of the building grows in size until its slope stands at the angle of repose of dry sand, approximately 34° (Bagnold, 1941). When the equilibrium is reached, additional sediment particles moving towards the windward face of the building slide down the slope of the upwind deposition and join the sediment streams passing around the lateral walls of the building. They are then deposited in two tails starting at a small distance from the lateral walls of the building, and apparently follow the horseshoe-shape vortex downstream of the building (Bagnold, 1941; Pye and Tsoar, 2008; Poppema et al., 2021; Pourteimouri et al., 2022). These two deposition tails gradually merge as the two opposed reversing vortices in the low-speed cavity region carry the sediment particles from the depo-

sition tails towards the middle of the leeward face of the building and create the so-called sand shadow immediately behind the building (Bagnold, 1941; Pye and Tsoar, 2008; Livingstone and Warren, 1996; Luo et al., 2012). Furthermore, previous studies showed that the most intensive erosion occurs around the windward edge and corners of the building (Iversen et al., 1991; Tominaga et al., 2018; Pourteimouri et al., 2022).

Previous studies have examined morphological changes around buildings, while little attention has been paid to how and to what extent these changes depend on the positioning of buildings at the beach. The incident wind direction with respect to the buildings strongly influences the characteristics of the secondary flow patterns in the near-wake region which, in turn, determine the generation and development of sand shadows in the lee of buildings (Cooke et al., 1993; Becker et al., 2002; Luo et al., 2012; Unnikrishnan et al., 2017). In real beach conditions, buildings are mainly positioned close to each other due to the growth of beach tourism and high demand for centralized facilities on the limited land space at the beach. The wind is slightly accelerated through the gap spacing between adjacent buildings due to the funneling effect. This increases the sediment-entraining capacity of the air. In the lee of the gap, the air decelerates as it flows in a larger space and joins the undisturbed flow sufficiently downstream of the buildings. As a result, the sediment will deposit and form the so-called sand drift at a small distance downstream of the gap (Bagnold, 1941; Pye and Tsoar, 2008; Cooke et al., 1993; Luo et al., 2014; Luo et al., 2016; Poppema et al., 2022b). First attempts to systematically study the impact of building positioning with respect to neighboring buildings and the prevailing wind on flow characteristics and the implications for sediment transport go back to the wind-tunnel studies by Luo et al. (2012), Luo et al. (2014) and Luo et al. (2016). However, they only focused on the near-wake flow region, and mainly on the airflow mechanisms responsible for the formation and evolution of sand shadow and sand drift that develop just behind the building, and in the lee of the gap spacing between neighboring buildings, respectively. In a recent study by Poppema et al. (2022b); a series of field experiments was performed to study how the initial morphological changes around scaled buildings at the beach are influenced by buildings positioning. An analysis considering real beach conditions, a systematic study around full-scale buildings in a row when the gap spacing between neighboring buildings and the angle of wind incidence are changed over a wide range is lacking so far.

This study aims to answer the following research questions: Q1) How do the flow mechanisms that are responsible for sediment transport around a row of full-scale buildings at the beach change when the gap spacing between neighboring buildings increases?; Q2) How do the flow mechanisms that are responsible for sediment transport around a row of full-scale buildings at the beach change when the wind incidence angle relative to the buildings changes?; Q3) How and to what extent is the potential sediment supply from beach to down-

stream (towards dunes in real beach) influenced by the buildings positioning at the beach? For the latter research question, we will only study the combined impacts of the buildings spacing in the row and their orientation with respect to the dominant wind.

The present study investigates how the flow mechanisms and the initial morphological patterns around a row of full-scale buildings at the beach, are affected by the gap spacing between neighboring buildings and the wind direction. For this purpose, the OpenFOAM software that makes use of mainstream CFD approaches is used. The choice of methods and model specifications were extensively elaborated by Pourteimouri et al. (2022).

This paper is organized as follows. In Section 3.2, the model descriptions and methods used in this study are presented. Results on the impact of gap spacing and wind incidence angle on near-bed horizontal flow patterns are presented in Section 3.3.1. In Section 3.3.2, the wind-induced bed shear stress due to variations in gap spacing and wind incidence angle are presented. The sediment transport flux is then computed and the duneward component (in x direction) for variations in gap spacing and wind incidence angle is presented in Section 3.3.3. In Section 3.3.4, the initial changes in bed elevation are presented. The paper ends with discussion and conclusions that are presented in Section 3.4 and Section 3.5, respectively.

3.2. METHODOLOGY

3.2.1. MODEL SPECIFICATIONS

IN this study, the three-dimensional OpenFOAM model used by Pourteimouri et al. (2022) is further modified to simulate the flow mechanisms around a row of ten full-scale beach buildings. The gap spacing between adjacent buildings and the prevailing wind direction with respect to the buildings is systematically changed. The simpleFOAM solver is selected, which solves the steady Reynolds-averaged Navier-Stokes (RANS) equations for incompressible turbulent flows, using the finite volume method (FVM). The SIMPLE (Semi-Implicit Method for Pressure-Linked Equations) algorithm is used to solve the model equations. The standard $k-\varepsilon$ turbulence closure model is used to solve the turbulence in the vicinity of buildings. The configuration of the computational domain with a row of ten full-scale beach buildings is shown in Figure 3.2. Dimensions of the computational domain and beach buildings used in this study are summarized in Table 3.1. The blockMesh utility of OpenFOAM is used to generate grids with the size of $\Delta x = \Delta y = \Delta z = 1$ m within the entire computational domain. The snappyHexMesh utility is then used to refine the mesh in a bounding box with the height of 9 m from the bed surface. The grid cells in the refinement region are refined four times as they get closer to the buildings. This ends to the cells with

the size of $\Delta x = \Delta y = \Delta z = 0.0625$ m close to the buildings. The blockMesh and snappyHexMesh utilities in OpenFOAM are used to generate mesh grids within the computational domain. The total number of computational grids in the domain is approximately 3.5 million that mainly consists of hexahedra cells and some polyhedra cells connecting the coarse to fine cells together.

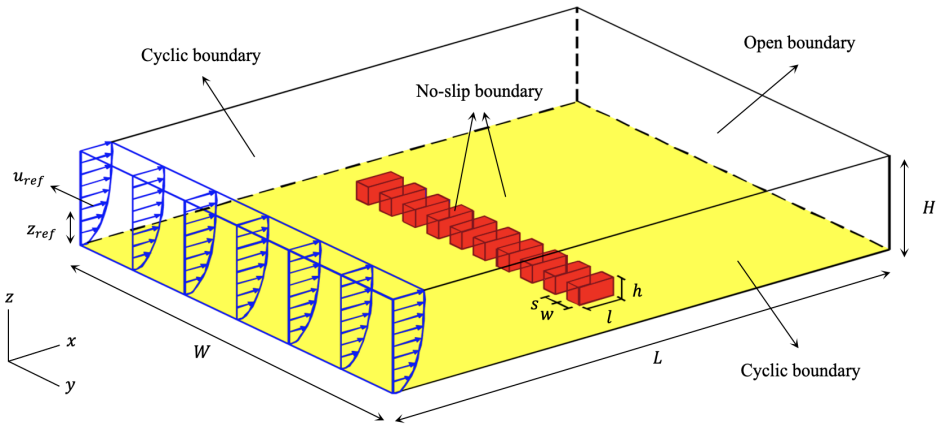

Figure 3.2: Schematization of the modelled beach buildings within the computational domain. The domain inlet is located at $x = 0$ m, and the incident wind is perpendicular to the upwind (seaward) face of buildings.

Table 3.1: Geometric dimensions of the computational domain and beach buildings.

Variable	**Value [m]**
Length of the domain (L)	150.00
Width of the domain (W)	150.00
Height of the domain (H)	50.00
Length of beach buildings (l)	6.00
Width of beach buildings (w)	2.50
Height of beach buildings (h)	2.50
Gap spacing between neighboring buildings (s)	0.25 – 10.00

As shown in Figure 3.2, the fully-developed profiles of logarithmic wind velocity, U, and turbulence parameters, k and ε, are applied as the inlet boundary conditions using the equations proposed by Richards and Hoxey (1993). The reference wind speed of $u_{ref} = 17$ m/s is considered at the reference height of $z_{ref} = 1.8$ m above the ground level, $z = 0$ m, to prescribe the logarithmic velocity profile at the inlet of the domain. A uniform surface roughness height of $z_0 = 0.00001$ m is applied at the bottom of the domain, which was computed

based on the median sediment grain size at the beach (3.00×10^{-4} m). The open boundary condition with zero-gauge pressure is considered at the outlet of the domain. At the spanwise boundaries of the domain, the cyclic (periodic) boundary condition is used to assure that the flow conditions are periodically repeating between these two boundaries, allowing the incident wind to make an angle with the centerline of the buildings (x-direction). Another advantage of using the cyclic lateral boundaries is that it reproduces the actual beach situation where the row of buildings is repetitively placed at the beach. It should be noted that we assumed a constant domain width, meaning that by increasing the gap size between neighboring buildings in the row, we reduce the distance between the neighboring rows of buildings. Furthermore, the no-slip velocity boundary condition is used at the bottom of the domain and the buildings' walls. The wall functions are used to accurately resolve the steep gradients of the flow velocity close to the wall. The log-law of the wall for turbulent flow around the buildings is used that significantly reduces the requirements for high grid resolution in the near-wall region. This is achieved by locating the first cell centroid off the wall in the log-law region of the boundary layer, $y^+ > 30$, instead of the linear viscous sub-layer, $y^+ < 5$ (Blocken et al., 2007). More detailed information on the model specifications, and the implementation of boundary conditions and wall functions can be found in Pourteimouri et al. (2022).

3.2.2. MODEL SETUP FOR SPACING AND ORIENTATIONS SCENARIO'S

TO systematically evaluate the impact of gap spacing between neighboring beach buildings on flow mechanisms and morphological changes around buildings, 16 different simulations were performed, in which the gap spacing between buildings increased from 0.1 to 4 times the width of each building. Similar to the previous studies by Luo et al. (2014) and Luo et al. (2016), a dimensionless parameter, the gap ratio, was used in the present study. When considering equal distances between neighboring beach buildings in the row, the gap ratio, $g^* = s/(s+w)$, denotes the ratio of the gap spacing between buildings to the center-to-center distance between buildings (Figure 3.3). The wind incidence angle, θ_w, represents the angle between the prevailing wind direction and the centerline of the buildings (Figure 3.3). To understand how the airflow patterns and the bed level change around beach buildings are influenced by the wind incidence angle, five different wind directions, 0°, 20°, 40°, 60° and 80°, were applied for each tested gap ratio. An overview of the total 80 conducted simulations is given in Table 3.2.

3.2.3. SEDIMENT TRANSPORT FLUX

IN sandy substrate such as beaches, the wind-blown sediment transport initiates when the wind shear velocity, $\overrightarrow{u_*}$, exceeds a certain threshold shear velocity, $u_{*_{th}}$. The com-

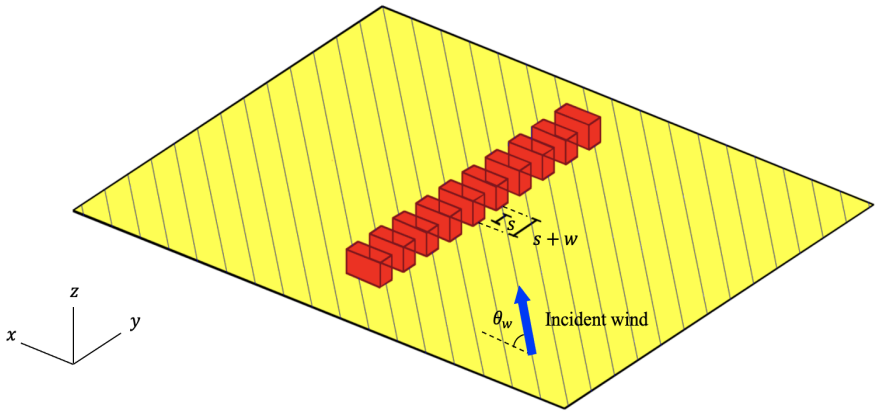

Figure 3.3: Illustration of the prevailing wind in the domain, wind incidence angle, θ_w, and the parameters used to characterize the gap ratio, g^*.

Table 3.2: Parameters of the total 80 conducted simulations.

Dimensionless gap Spacing, s/w [-]	**Gap Ratio, g* [-]**	**Wind Incidence Angle, θ_w [°]**
0.10	0.09	0, 20, 40, 60, 80
0.20	0.17	0, 20, 40, 60, 80
0.30	0.23	0, 20, 40, 60, 80
0.40	0.29	0, 20, 40, 60, 80
0.50	0.33	0, 20, 40, 60, 80
0.60	0.37	0, 20, 40, 60, 80
0.70	0.41	0, 20, 40, 60, 80
0.80	0.44	0, 20, 40, 60, 80
0.90	0.47	0, 20, 40, 60, 80
1.00	0.50	0, 20, 40, 60, 80
1.50	0.60	0, 20, 40, 60, 80
2.00	0.67	0, 20, 40, 60, 80
2.50	0.71	0, 20, 40, 60, 80
3.00	0.75	0, 20, 40, 60, 80
3.50	0.78	0, 20, 40, 60, 80
4.00	0.80	0, 20, 40, 60, 80

monly used aeolian sediment transport models based on the experimental measurements show that the equilibrium (saturated) sediment transport flux, $\overrightarrow{q}$, is a function of wind shear velocity and threshold shear velocity (Bagnold, 1937; Kawamura, 1951; Hsu, 1971; Lettau and Lettau, 1977; Horikawa et al., 1983). In this study, sediment transport was mod-

elled using the transport formulation proposed by Bagnold (1937) as follows:

$$\overrightarrow{q} = C\frac{\rho_a}{g}\sqrt{\frac{d}{D}}(|\overrightarrow{u_*}| - u_{*_{th}})^3\frac{\overrightarrow{u_*}}{|\overrightarrow{u_*}|} \tag{3.1}$$

where $\overrightarrow{q}$ [kg/m/s] is the sediment transport flux; C [-] is an empirical constant related to the sediment particle size distribution, ranging from 1.50 for nearly uniformly distributed sediment particles to 2.80 for widely distributed sediment particles; ρ_a [kg/m^3] is the density of air (1.29 kg/m^3); g [m/s^2] is the gravitational acceleration; d [m] is the nominal sediment particle size (3.00×10^{-4} m); D [m] is the reference sediment particle size (2.40×10^{-4} m); $\overrightarrow{u_*}$ [m/s] is the wind shear velocity; and $u_{*_{th}}$ [m/s] is the threshold shear velocity. The wind shear velocity, $\overrightarrow{u_*}$, is calculated by:

$$\overrightarrow{u_*} = \sqrt{\frac{|\overrightarrow{\tau}|}{\rho_a}}\frac{\overrightarrow{\tau}}{|\overrightarrow{\tau}|} \tag{3.2}$$

where $\overrightarrow{\tau}$ [N/m^2] is the wind shear stress calculated at the bed of the computational domain by solving the flow field using the airflow model used in this study, OpenFOAM. The post-processing techniques provided by OpenFOAM was used to extract the results of the bed shear stress ($z = 0$ m) at the center of each grid cell across the entire domain.

As the wind-induced drag and lift forces on sediment particles increase, there is a critical shear velocity at which the sediment particles start moving. This threshold shear velocity, $u_{*_{th}}$, is derived by Bagnold (1937) as:

$$u_{*_{th}} = A\sqrt{\frac{\rho_s - \rho_a}{\rho_a}gd} \tag{3.3}$$

where A is an empirical constant dependent on the sediment particle size; and ρ_s [kg/m^3] is the density of sediment (2.65×10^3 kg/m^3). The value of A is 0.1 for sediment particles greater than 8.00×10^{-5} m (Nickling and Neuman, 2009).

The sediment transport flux, $\overrightarrow{q}$, represents the sediment-carrying capacity of incident wind parallel to the wind direction. In order to predict the potential of wind to move sediments in the cross-shore direction and towards the dune, the x component of $\overrightarrow{q}$ is derived using the local wind incidence angles as (Bauer and Davidson-Arnott, 2003; Delgado-Fernandez and Davidson-Arnott, 2011):

$$q_c = |\overrightarrow{q}|\cos\theta_{wl} \tag{3.4}$$

where q_c [kg/m/s] is the sediment transport flux in the cross-shore direction (x component of $\vec{q}$); and θ_{wl} is the local wind direction at each computational grid.

3.2.4. INITIAL EROSION AND DEPOSITION PATTERNS

IN this study, we are investigating how the potential morphological changes around beach buildings are influenced by the gap spacing between buildings and by the wind incidence angle. To evaluate the areas at which the sediment particles are eroded or deposited around beach buildings, the Exner equation is used, which describes the mass balance between the deposited sediment on the bed and the sediment in transport. The general form of the Exner equation is as follows (Paola and Voller, 2005; Bauer et al., 2015):

$$\frac{\partial z_b}{\partial t} = -\frac{1}{\rho_s(1-n)}\vec{\nabla}\cdot\vec{q} \tag{3.5}$$

where z_b [m] is the bed level; t [s] is the time; and n [-] is the sediment porosity (0.4). The equation states that the rate of changes in bed level through time is proportional to the spatial divergence of the sediment transport flux.

3.3. RESULTS

3.3.1. NEAR-BED HORIZONTAL FLOW PATTERNS

3.3.1.1. IMPACT OF GAP SPACING

FIGURE 3.4 shows the horizontal near-bed streamline patterns around a row of ten full-scale beach buildings for different gap ratios, g^*, when the incident wind is perpendicular to the front face of the buildings, $\theta_w = 0°$. It should be noted that in computations of the streamlines, the z component of the velocity was not taken into account. For the sake of brevity, among sixteen different tested gap ratios, only the results for the five most important ones, consisting 0.09, 0.41, 0.47, 0.50 and 0.67 are presented. These figures show that the flow patterns downstream of the buildings are complex, and depend on the gap ratio between neighboring buildings. This is due to the interactions between the jet flows passing through the gap spacings between buildings and the deflected flows due to the presence of buildings, moving around the lateral faces of the buildings. The near-wake streamline patterns shown in Figure 3.4 are comparable with those observed for two adjacent wide rectangular obstacles in wind-tunnel experiments by Luo et al. (2014).

For small gap spacing, $g^* = 0.09$, the row of ten buildings effectively forms one wide rectangular bluff body for the approaching wind. The jet flows passing through the small gap spacings between buildings are negligible and the airflow is mainly split at the upwind face

of the bluff body, moving towards the lateral faces, see Figure 3.4a. The deflected flows are separated from the sharp trailing corners of the bluff body and form a pair of large opposing vortices in the low-pressure zone just behind the lee face of the body. The approximate longitudinal and spanwise dimensions of the downwind recirculation region are $l_R = 6.9w$ and $w_R = 10.98w$, respectively. It should be noted that the location of the flow reattachment point, shown in Figure 3.4a, is determined by examining where the streamwise velocity component, u, of the flow along the centerline of the central gap spacing between buildings changes in sign from negative to positive at $z = 0.25$ m. The length of the recirculation region, l_R, was then computed as the distance between the reattachment point and the lee face of the buildings. Furthermore, the width of the recirculation region, w_R, was computed as the length of the line that connects the outer edges of the opposing vortices, and is located just behind the lee face of the buildings.

As the gap ratio increases to $g^* = 0.41$, the jet flows through the gap spacings between neighboring buildings are enhanced. Jet flows are detached from the surface when they encounter the sharp lee corners of the buildings and inclined into different directions by the Coanda effect (Yen and Liu, 2011). Therefore, two small counter-rotating vortices are formed immediately downstream of the gaps. These smaller size vortices are encompassed with a pair of larger vortices that are formed by the deflected flows around the row of buildings, shown in Figure 3.4b. It is notable that the flow reattachment point appears at a closer distance from the downwind faces of the buildings, and the approximate streamwise length of the separation bubble decreases to $l_R = 6.5w$.

The jet flows through the gap spacings between buildings become more pronounced and the small vortices that form in the near-wake region just behind the gaps grow in size as the gap ratio increases. For $g^* = 0.47$, the jet flows become intense enough to maintain their initial direction for a longer distance downstream of the buildings and disturb the pair of larger vortices that surrounded the buildings row as whole. As shown in Figure 3.4c, the lee streamlines are intertwined due to the confluence of the jet flows and the deflected flows. In addition, the smaller vortices move from just behind the gap to just behind the leeward face of the buildings, and form individual recirculation regions behind each building.

The impact of neighboring buildings on each other becomes less as the gap ratio increases. For $g^* = 0.50$, the jet flows are slightly inclined inward, and the downstream streamlines are compressed (Figure 3.4d). For far enough apart buildings with $g^* \geq 0.67$, the jet flows stay parallel to the incident wind, therefore the near-bed flow patterns can be regarded almost independently from neighboring buildings (Figure 3.4e).

The near-bed streamwise velocity distribution along the centerline of the central gap spacing between buildings for eight different gap ratios and $\theta_w = 0°$ is shown in Figure 3.5. Also

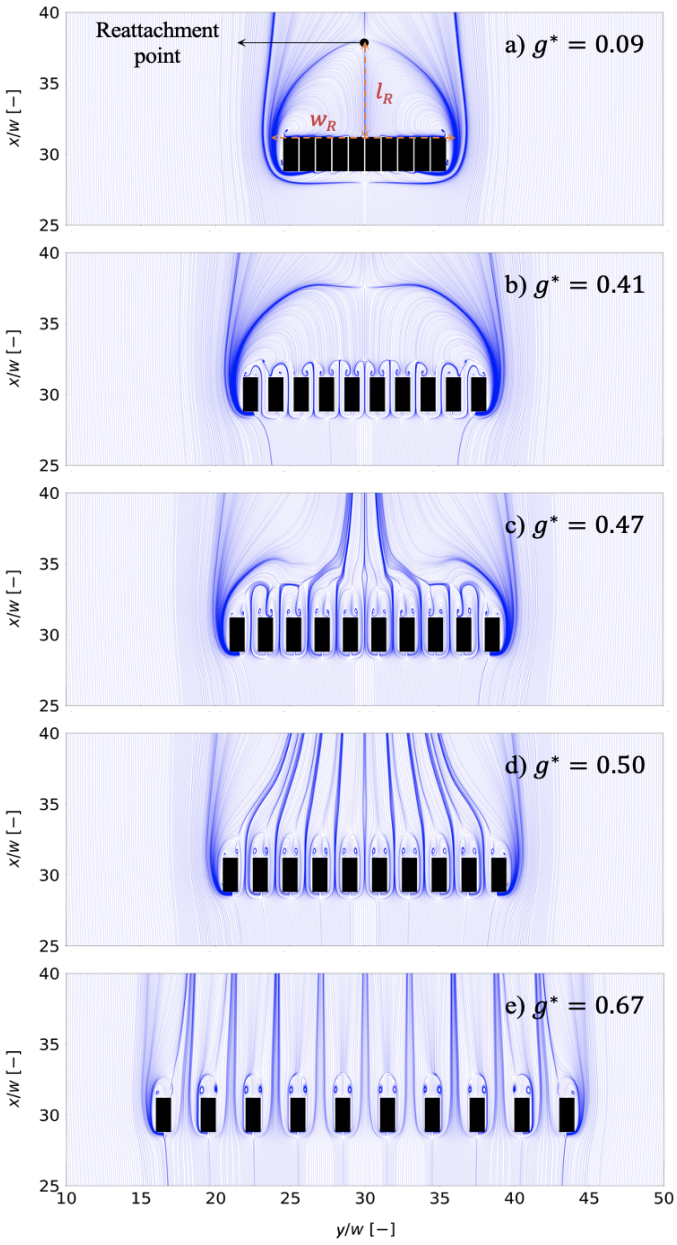

Figure 3.4: Horizontal airflow patterns at a near-bed plane, $z = 0.25$ m, for $\theta_w = 0°$, and the gap ratio, g^*, is changed as a) 0.09, b) 0.41, c) 0.47, d) 0.50 and e) 0.67.

indicated in Figure 3.5, the streamwise velocity upstream of the buildings decreases dramatically for the closely spaced buildings. For $g^* \leq 0.29$, a small reverse-flow region forms

in front of the central gap. As g^* decreases to 0.09, the upwind streamwise velocity reaches its minimum value at $x = 28.30w$, and its magnitude is approximately 1/20th of the free stream velocity far enough upstream of the row of buildings.

The funneling effect through the gap spacing between buildings causes the streamwise velocity to increase at the beginning of the gap. For $g^* \leq 0.50$, the larger the gap ratio, the farther and the greater maximum streamwise velocity through the central gap. The peak streamwise velocity through the central gap appears at $x = 28.84w$ when $g^* = 0.09$, and it increases by about 12 times at $x = 29.55w$ as g^* increases to 0.50. The streamwise velocity then begins to decrease right after the maximum to some distance downstream of the gap, and then increases to join the undisturbed flow far enough downstream of the buildings. For $g^* \leq 0.47$, the streamwise velocity becomes negative, immediately behind or at some distance downstream of the central gap, depending on the prominence of the smaller vortices just behind the gap, and the pair of large counter-rotating vortices that form behind the row of buildings. The smaller the gap size, the smaller the minimum streamwise velocity, and the minimum is located closer with respect to the lee of the central gap as shown in Figure 3.5. For instance, the minimum streamwise velocity appears at x=33.30w for $g^* = 0.09$, versus $x = 35.30w$ for $g^* = 0.50$.

For $g^* = 0.67$ at which the neighboring buildings are far enough apart to be considered almost independent from each other (Figure 3.4e), the decrease in streamwise velocity both in configurations with smaller g^*. In addition, for $g^* \geq 0.67$, the funneling effect through the central gap decreases, therefore the streamwise velocity increases less significantly through the gap. For instance, the difference between the maximum streamwise velocity through the central gap and the minimum streamwise velocity in front of the central gap when $g^* = 0.50$, is 6.60 times that of for the $g^* = 0.80$. Figure 3.5 indicates that the streamwise velocity behind the central gap spacing for configurations with larger g^*, is significantly higher than that for configurations with smaller g^*, meaning that a higher amount of sediment transport flux towards the dune is expected just behind the central gap when the gap ratio is large.

3.3.1.2. IMPACT OF WIND INCIDENCE ANGLE

THE horizontal near-bed streamline patterns (at an elevation of $z = 0.25$ m above the bed) around a row of ten full-scale beach buildings at five different wind incidence angles, θ_w, 0°, 20°, 40°, 60°, and 80°, and a constant gap spacing of $g^* = 0.67$ are shown in Figure 3.6. These figures show that the near-bed flow patterns depend on both the gap spacing between neighboring buildings and the incoming wind direction. Figure 3.6a shows that in the case of buildings oriented perpendicular to the incident wind, $\theta_w = 0°$, there is only one wall in each building facing the wind. Therefore, the approaching wind is split into two frac-

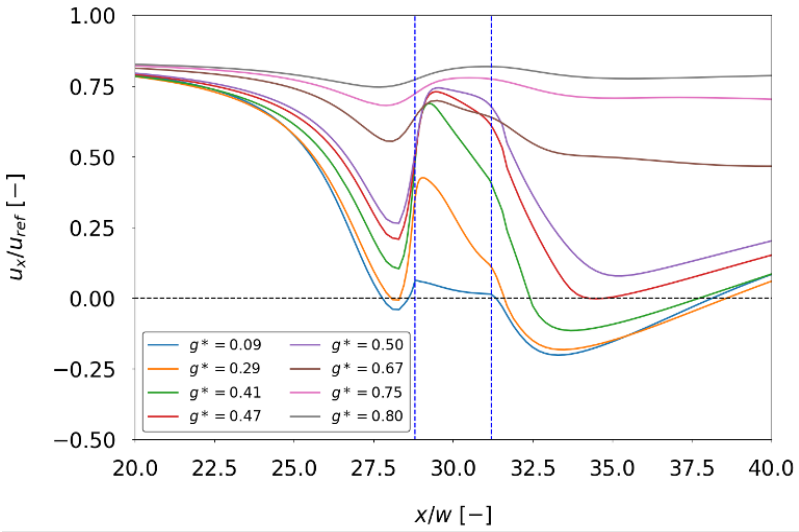

Figure 3.5: Streamwise velocity, u, at $z = 0.25$ m, along the centerline of the central gap spacing between buildings for various gap ratios, g^*, and $\theta_w = 0°$. The dashed blue vertical lines show the location of the buildings and hence the start and end position of the central gap. The reference wind speed is $u_{ref} = 17$ m/s.

tions of flow in front of the wind-facing walls, wrapping around the streamwise faces of the buildings, and creating a pair of recirculating vortices immediately behind the downwind face of the buildings. The two branches of flow are equal, and the downwind vortices are fully symmetric for buildings with large enough gap spacing. In case of obliquely oriented buildings, $\theta_w > 0°$, there are two walls in each building facing the wind. The orientation of the wind-facing walls relative to the incident wind determines the location of the stagnation point at which the incoming flow is split into two branches, and the fraction of flow steered to each side of the building.

For $\theta_w = 20°$, the incident wind is split at the shorter wind-facing wall of the buildings. Figure 3.6b shows that a large fraction of flow is steered towards the low-pressure region just behind the downwind faces of the buildings. The deflected flows, reaching the sharp corners of the buildings are separated from the surface, and form a recirculating flow region that shows reversed flow just behind the longer downwind face of the buildings. The size of the recirculating flow region and the flow reattachment point depend on the positioning of the building in the row, gap spacing between buildings and the constraint effect due to the presence of the neighboring buildings. Therefore, the flow may reattach at the shorter downwind face of the buildings (*A*) like the last building in the row, the most downwind, where there is no neighboring building on its right, or at the longer downwind face of the buildings (*B*) like the rest of the buildings in the row. In case of flow reattachment at the longer downwind face of the buildings, the flow reaching the upper right corner of the

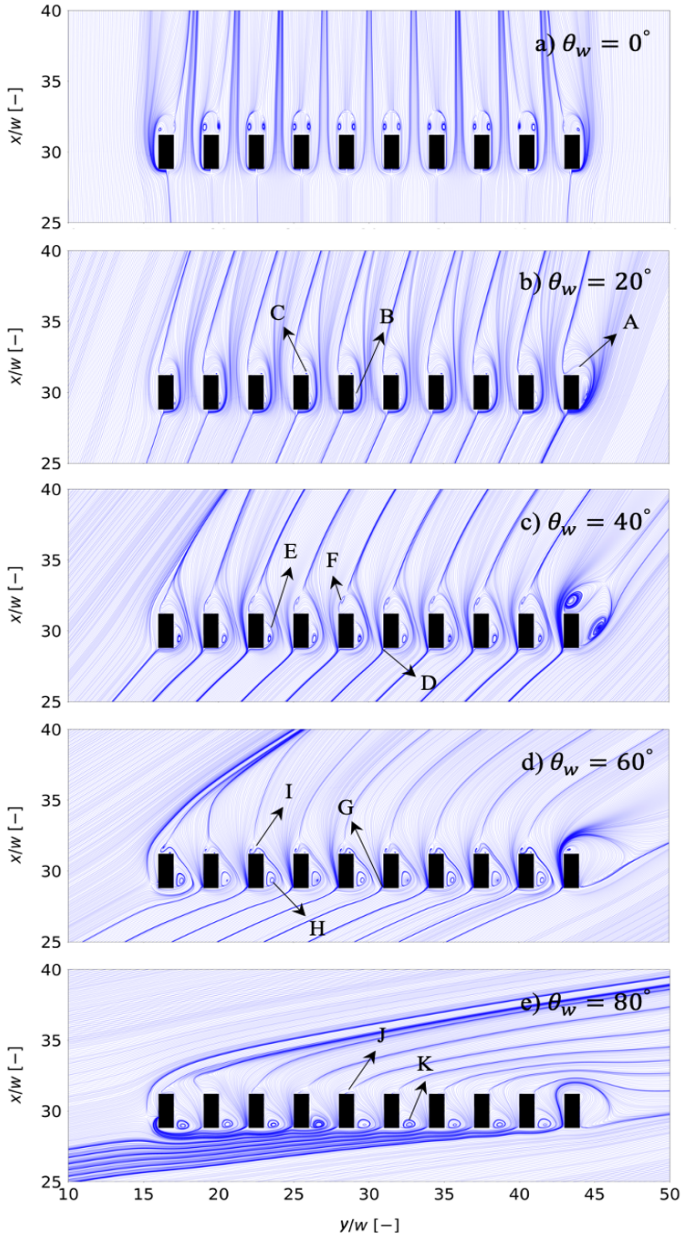

Figure 3.6: Horizontal airflow patterns at a near-bed plane, $z = 0.25$ m, for $g^* = 0.67$, and the wind incidence angle, θ_w, is changed as a) 0°, b) 20°, c) 40°, d) 60°, and e) 80°.

buildings (in the top view) is again separated from the surface and creates a small rotating vortex (C). The flow is then merged with the deflected flow at the other side of the buildings

to join the undisturbed flow far enough downstream of the buildings.

As the wind incidence angle increases to $\theta_w = 40°$, the stagnation points move to the lower left corners of the buildings (*D*), and a large portion of the flow follows the longer wind-facing wall of the buildings. The reverse flow regions just behind the longer downwind face of the buildings grow for more oblique wind (*E*) as Figure 3.6c shows. A small rotating vortex forms at some distance downstream of the shorter downwind face of the middle buildings (*F*), which is bounded on the outside by the deflected flow towards the longer wind-facing wall. This vortex disappears at the first building in the row, the most upwind, as the compressed flow spread out when there is no neighboring building on its left. In addition, the last building in the row does not face an obstruction in front, therefore these two vortices grow and cover the whole surface of the downwind walls, creating a separation bubble with two large asymmetric opposing vortices.

For $\theta_w = 60°$, the separation point appears at the longer wind-facing wall of the buildings (*G*), and the flow pattern except the last building in the row, is characterized by one large vortex just behind the longer downwind face (*H*), and two small vortices behind the shorter downwind face of the buildings (*I*). For more oblique winds, the row of buildings effectively forms a single long bluff body, see Figure 3.6d. Therefore, the deflected flow around the first building in the row affects the flow downstream of the rest of the buildings so that the streamlines bend slightly inwards, pushing the two small vortices behind the shorter downwind face of the buildings towards the buildings. This flow sheltering due to the most upwind building in the row is more intense for $\theta_w = 80°$, in which the two small vortices almost disappear (*J*). As shown in Figure 3.6e, the large elliptical vortex behind the longer downwind face of the buildings (*K*) rotate so that the longer diagonal of the vortex is along the y direction rather than the x direction.

The changes in near-bed x component of velocity along the centerline of the central gap spacing between buildings for five different wind incidence angles, and $g^* = 0.67$ are shown in Figure 3.7. As shown in Figure 3.7, the higher the wind incidence angle, the smaller the x component of velocity upstream of the buildings. In addition, for all wind incidence angles, the x component of velocity decreases in front of the central gap. The difference between the highest x component of velocity far enough upstream of the buildings, and the lowest x component of velocity in front of the central gap decreases for more oblique winds. For instance, the decrease in x component of velocity from highest to the lowest value upstream of the central gap when $\theta_w = 0°$ is 4.87 times greater than that of for $\theta_w = 80°$.

For $\theta_w \leq 60°$, the x component of velocity is then increased to an initial peak as the flow enters the central gap due to the funneling effect. In case of buildings that are placed perpendicular to the incident wind, $\theta_w = 0°$, the flow decelerates and the x component of ve-

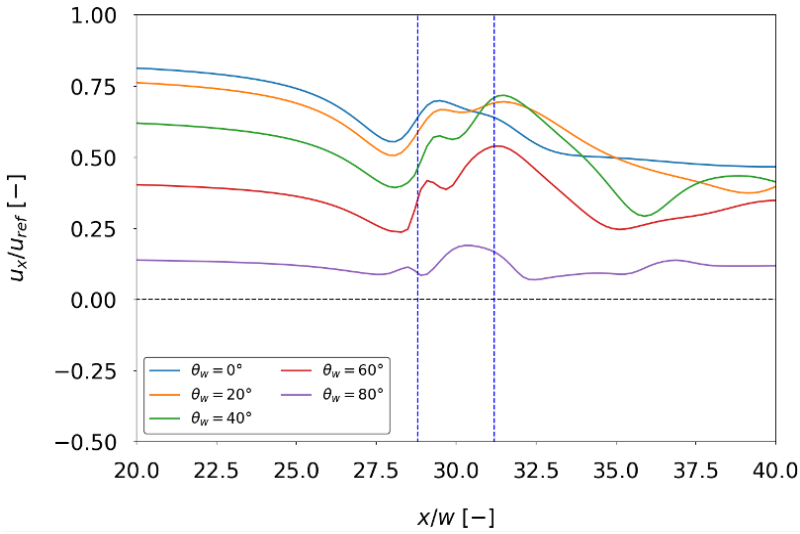

Figure 3.7: X component of velocity, u, at $z = 0.25$ m, along the centerline of the central gap spacing between buildings for various wind incidence angles, θ_w, and $g^* = 0.67$. The dashed blue vertical lines show the location of the buildings and hence the start and end position of the central gap. The reference wind speed is $u_{ref} = 17$ m/s.

locity gradually decreases through the remaining central gap to some distance downstream due to the flow expansion. As the incident wind becomes oblique, $\theta_w = 20°$, $40°$ and $60°$, a recirculation region forms just behind the longer downwind face of the buildings, causing a small decrease in the x component of velocity through the central gap. The incoming flow passing the central gap is constrained by this recirculation region and the deflected flow due to the presence of the neighboring building. The x component of velocity shows two local maximums because of the funneling effect between the buildings and the recirculation region added together. It should be noted that the flow pattern is slightly different for $\theta_w = 80°$ compared to the other wind incidence angles greater than zero. The initial peak appears immediately in front of the central gap at $x = 28.50w$. The x component of velocity decreases slightly when the flow enters the gap, which is due to the change in the orientation of the elliptical vortex when $\theta_w = 80°$ (Figure 3.6e). In addition, the second peak of the x component of velocity appears earlier at $x = 30.30w$, which is located inside the central gap.

As Figure 3.7 shows, the higher the wind incidence angle, the lower the initial peak. The second peak of the x component of velocity is always higher than the initial peak for $\theta_w \geq 20°$, and the maximum value occurs for $\theta_w = 40°$. The x component of velocity at the second peak when $\theta_w = 40°$ is 3.80 times greater than that for $\theta_w = 80°$. Furthermore, the x component of velocity behind the central gap spacing when $\theta_w \leq 40°$ is significantly higher than the other two wind incidence angles. Therefore, the lowest duneward sediment transport

flux behind the central gap is expected for the two most oblique winds. To understand which combination of the gap spacing between buildings and wind incidence angle result in the greatest amount of sediment transport towards the dunes, more quantitative justifications are needed. This will be discussed in Section 3.3.3.3.

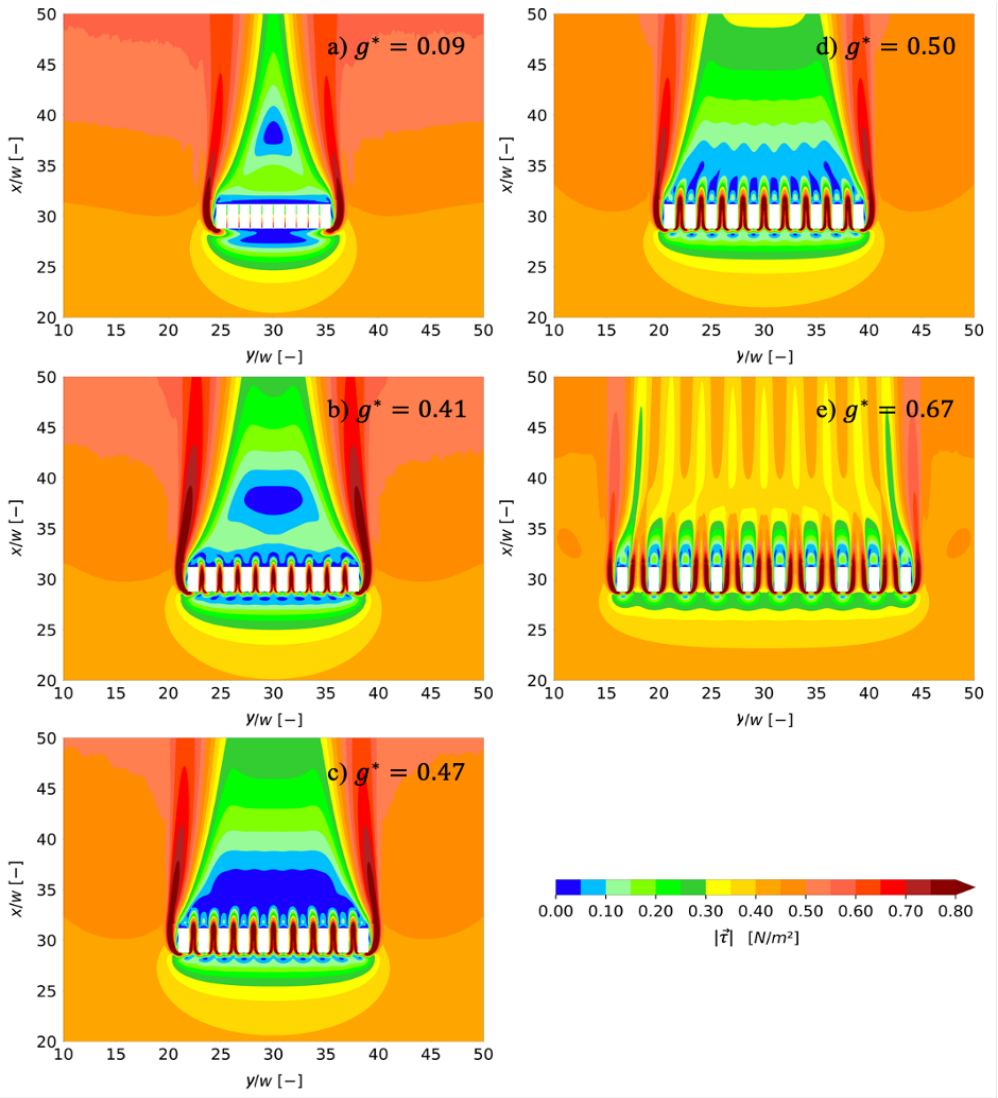

Figure 3.8: Spatial distribution of bed shear stress magnitude, $|\vec{\tau}|$, when $\theta_w = 0°$, and the gap ratio, g^*, is changed as a) 0.09, b) 0.41, c) 0.47, d) 0.50, and e) 0.67.

3.3.2. WIND SHEAR STRESS AT THE BED

3.3.2.1. IMPACT OF GAP SPACING

THE spatial variability of the bed shear stress magnitude, $|\vec{\tau}|$, around the row of buildings with five gap ratios that generated different airflow patterns in the near-wake region, for $\theta_w = 0°$ is shown in Figure 3.8. The bed shear stress results can be explained by the airflow patterns and velocity shown in Figures 3.4 and 3.5, respectively. A shadow zone with low bed shear stress develops just behind the lee face of the buildings (blue-shaded colors) as a result of flow pattern in the separation bubbles and vortices that form in the near-wake region. For smaller gap ratios, $g^* = 0.09$ and $g^* = 0.41$, another region with low bed shear stresses develops, depending on the location where the flow reattachment occurs (Figure 3.8a and b). As the gap ratio increases, the bed shear stress becomes higher in the gap spacings between neighboring buildings, and immediately behind the gaps (dark, red-shaded colors). This corresponds to high velocities between the buildings (Figure 3.5). For closely placed buildings, where $g^* = 0.09$, the flow passing through the gap spacings is negligible, therefore the increased bed shear stress in gaps is not apparent compared to larger gap ratios. Furthermore, two zones of high bed shear stress form on the outside of the row of buildings extending downstream. The intensity and the extension of these areas mostly depend on the gap spacing between buildings, the extent at which the air is blocked in front of the upwind faces of the buildings, is deflected towards the external buildings in the row, and being separated with high wind speeds from the sharp corners. For buildings that are placed sufficiently far apart, $g^* = 0.67$, the flow passing the gap spacings is more pronounced. Therefore, the flow blockage due to the presence of buildings, the deflected flows to the ends of the row of buildings, and the wind speed of the separated flows from corners is less substantial, producing areas with lower bed shear stresses around the buildings compared to smaller gap ratios. Similarly, the decreased bed shear stress just in front of the upwind faces of the buildings can also be explained by the flow blockage due to the presence of buildings. The closer the buildings, the lower the bed shear stress in front of the buildings.

3.3.2.2. IMPACT OF WIND INCIDENCE ANGLE

THE spatial variability of the bed shear stress magnitude, $|\vec{\tau}|$, around the row of buildings under five different wind directions, for $g^* = 0.67$ is shown in Figure 3.9. The bed shear stress results for different wind incidence angles show more complex patterns than with the varying gap ratios, but the overall patterns with respect to the wind-facing walls of the buildings are similar to those for the different gap spacings. For all incidence angles, the lowest bed shear stresses (blue and green-shaded colors) occur in front of the wind-facing walls of the buildings, and in the reverse flow region behind the downwind face of the buildings. For $\theta_w = 60°$ and $\theta_w = 80°$, the second to tenth buildings in the row are sheltered by the

most upwind building (first building in the row). Therefore, the near-wake region behind buildings is characterized by a larger area of low wind shear stresses than in the other wind incidence angles. Furthermore, the increased bed shear stress (dark, red-shaded colors) in the gap spacings between buildings strongly depend on the size, location, and orientation of the circulating vortices right next to the downwind faces of the buildings (see Figure 3.6). The larger separation bubble just behind the buildings confines the flow passing through the gap spacings and thus increases the funneling effect downstream of the gaps. As shown in Figure 3.9b, at which $\theta_w = 20°$, the areas with increased bed shear stress are narrower but longer, while Figure 3.9c, at which $\theta_w = 40°$, shows the wider but shorter areas with increased bed shear stress downstream of the gaps.

3.3.3. SEDIMENT TRANSPORT

3.3.3.1. IMPACT OF GAP SPACING

THE duneward sediment transport flux, q_c, distribution at the bed of the computational domain around a row of ten full-scale beach buildings with five different gap ratios for $\theta_w = 0°$ is shown in Figure 3.10. Results for each examined gap ratio show that the duneward sediment transport flux is greatest (red-shaded colors) through the gap spacings between buildings, and around the both ends of the row of buildings towards downstream. The lowest values of the duneward sediment transport flux occur in front of the windward face of the buildings, and behind the buildings, especially in the near-wake region in the wind shadow of buildings. It should be noted that the zero-duneward sediment transport flux is associated with the alongshore local wind directions, and the locations where the wind shear velocity, $\overrightarrow{u_*}$, is less than threshold shear velocity, $u_{*_{th}}$. Furthermore, the negative sediment transport flux occurs within the separation bubble just behind the buildings or in front of buildings, where the flow direction is in opposite direction relative to the prevailing wind direction.

3.3.3.2. IMPACT OF WIND INCIDENCE ANGLE

THE duneward sediment transport flux, q_c, distribution at the bed of the computational domain around a row of ten full-scale beach buildings under five different wind directions, for $g^* = 0.67$ is shown in Figure 3.11. Results show that the duneward sediment transport flux is lowest for the two most oblique wind directions, $\theta_w = 60°$ and $\theta_w = 80°$. This means that the sediment particles are likely to be transported laterally as the prevailing wind direction becomes more alongshore rather than cross-shore. Furthermore, for $g^* = 0.67$, a slightly oblique wind direction, where $\theta_w = 20°$, causes sediment transport to continue longer downstream. This might increase the chance that the sediments from the beach reach the dune toe and be deposited somewhere in front of the dune or to maintain transport and being deposited further over the dune.

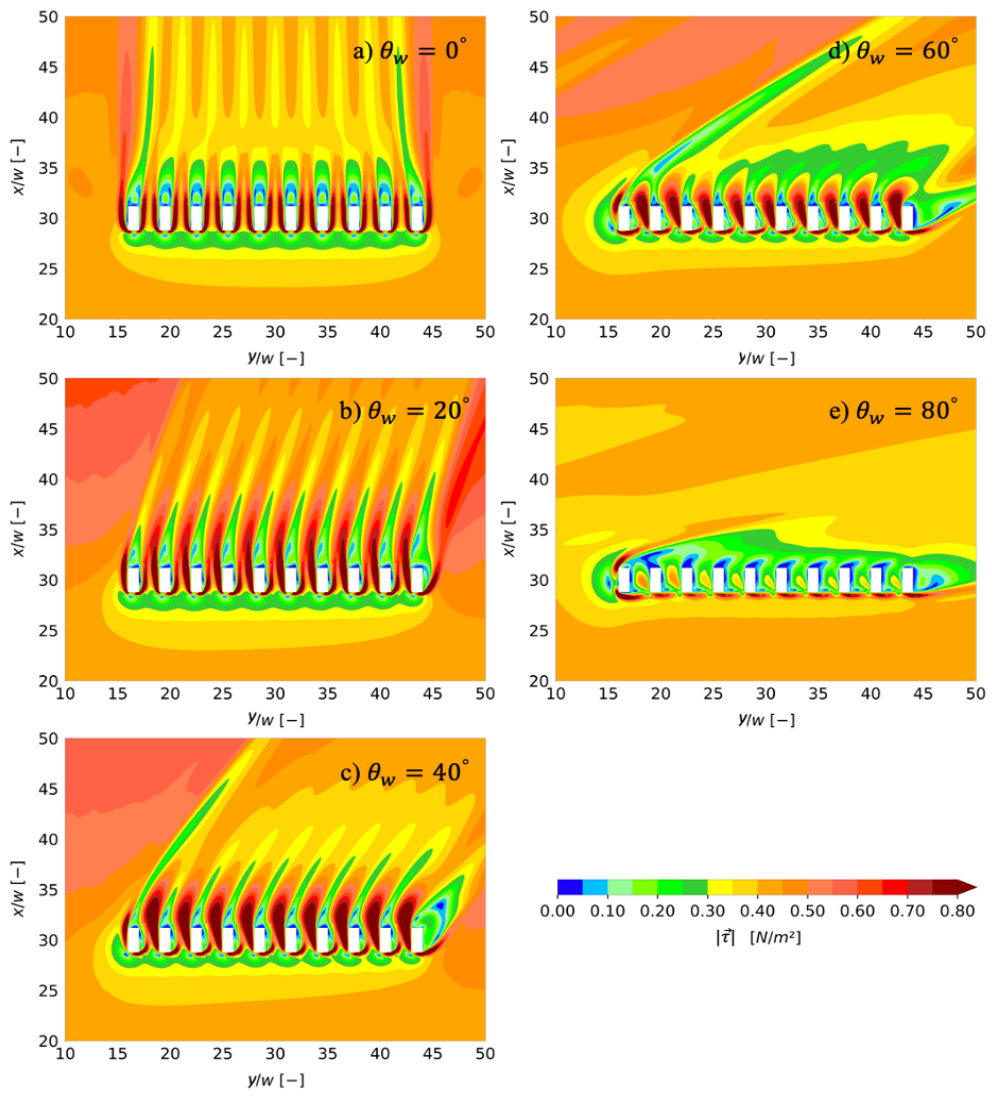

Figure 3.9: Spatial distribution of bed shear stress magnitude, $|\vec{\tau}|$, when $g^* = 0.67$, and the wind incidence angle, θ_w, is changed as a) 0°, b) 20°, c) 40°, d) 60°, and e) 80°.

3.3.3.3. COMPARISON BETWEEN DIFFERENT CONFIGURATIONS

IN the two previous sections, we focused on the systematic study of how the gap spacing between buildings and the dominant wind direction affect the spatial structure of potential sediment transport towards the dunes. However, to be able to systematically investigate the combined impact of gap spacing and the wind direction, we need to quantify the sediment transport in the downwind direction. In order to make an explicit compari-

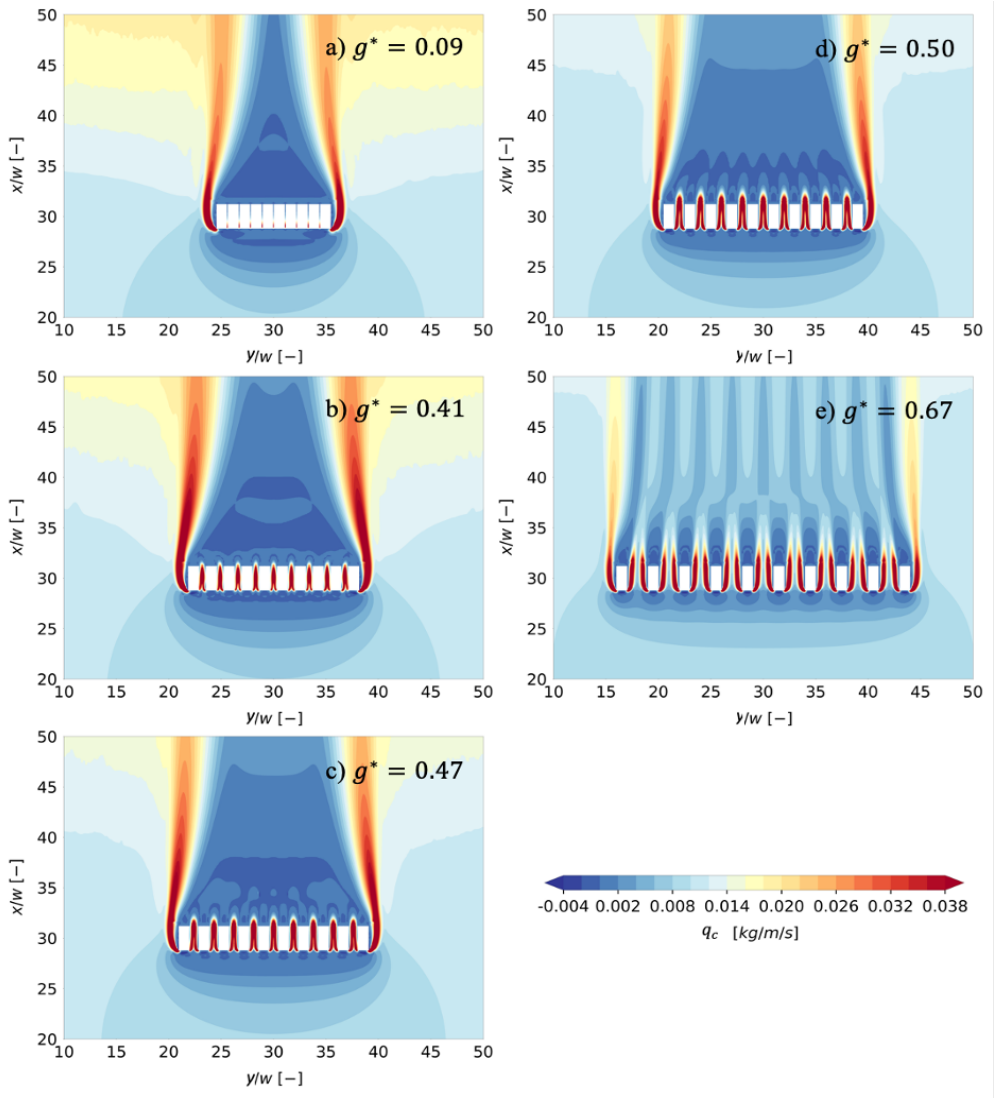

Figure 3.10: Spatial distribution of duneward sediment transport flux, q_c, when $\theta_w = 0°$, and the gap ratio, g^*, is changed as a) 0.09, b) 0.41, c) 0.47, d) 0.50, and e) 0.67.

son between 80 tested simulations, consisting of 16 different gap spacings, each tested for five different wind directions, a method is needed to find a single representative number for duneward sediment transport in each simulation, which can be compared between different simulations. For this purpose, two lines in the alongshore direction, y, are defined downstream of the row of buildings. Figure 3.12 displays that line 1 and line 2 are located 5 m, and 70 m downstream of the lee face of the buildings, respectively. These two lines

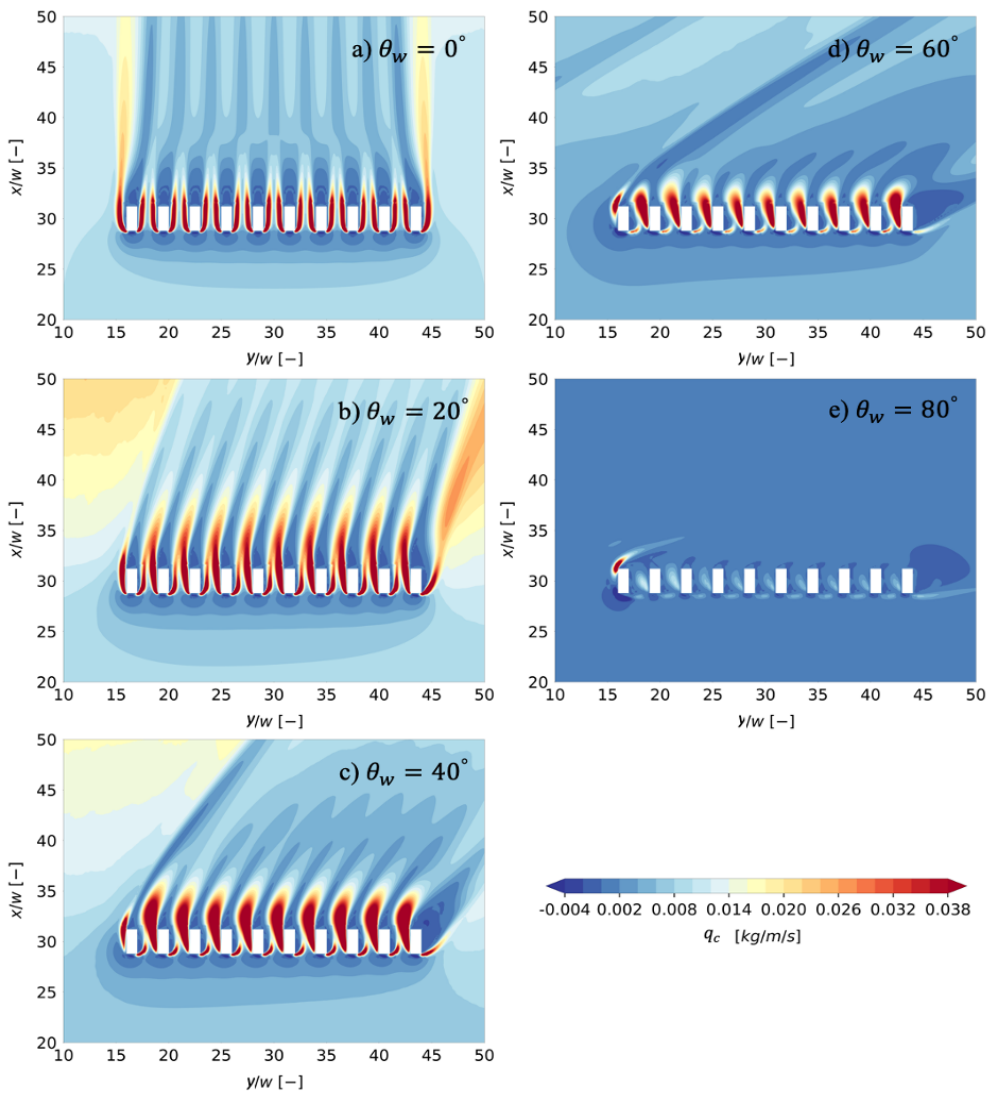

Figure 3.11: Spatial distribution of duneward (the x component of) sediment transport flux, q_c, when $g^* = 0.67$, and the wind incidence angle, θ_w, is changed as a) 0°, b) 20°, c) 40°, d) 60°, and e) 80°.

were selected, because the beach buildings are mostly placed at 5 – 10 m distance from the dune toe. Line 1 is thus representative of a typical location of a dune foot, whereas Line 2 represents a location much further downstream, i.e. somewhere well inside the dunes (but without actually modelling the dunes themselves).

The average duneward sediment transport flux in x direction is then computed over these lines for all simulations with different combinations of gap spacing and wind direction. In

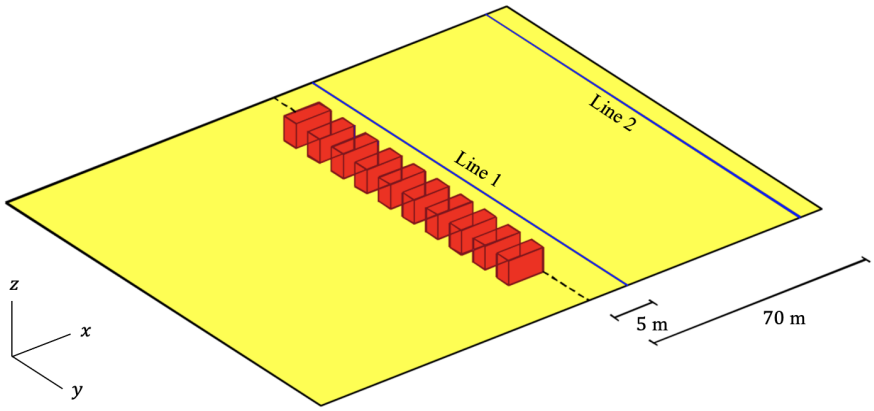

Figure 3.12: The location of the two lines downstream of the buildings, that the average duneward sediment transport flux is computed along.

order to compare the net effect of buildings on duneward sediment transport, the average transport flux along line 1 and line 2 in an empty domain without buildings, $q_{c_{ref}}$, are subtracted from the average transport flux in the domain including buildings, q_c. The results are shown in Figure 3.13, where each point corresponds to an individual simulation.

The blue shaded colors in Figure 3.13 show $q_c < q_{c_{ref}}$, indicate that the duneward sediment transport passing a given line in the presence of buildings is less than when there is no building at the beach. Similarly, the red shaded colors, $q_c > q_{c_{ref}}$, denote that the duneward sediment transport passing that line increases when the buildings are placed at the beach compared to the empty beach. In case of closely spaced beach buildings, $g^* < 0.67$, the buildings contribution to duneward sediment transport passing line 1 is small and mostly negative (see Figure 3.13a). In this situation, the highest positive effect of buildings on duneward sediment transport occurs when $\theta_w = 20°$. As the gap ratio increases, $g^* \geq 0.67$, the duneward sediment transport in the presence of buildings compared to the situation without buildings, is decreased for 0° and 80° winds, while it is enhanced for other wind directions. The highest enhanced duneward sediment transport due to the buildings occurs when $\theta_w = 40°$ and $\theta_w = 60°$.

Further downstream of the row of buildings, the buildings contribution to duneward sediment transport passing line 2 is positive in almost all combinations of the gap spacings and the wind directions (see Figure 3.13b). Results show that the highest enhanced sediment transport towards the dunes due to the presence of buildings occurs for 20° winds. Furthermore, the difference between the duneward sediment flux leaving line 2 in the situation with and without buildings is higher for closely spaced buildings compared to when buildings are far apart from each other.

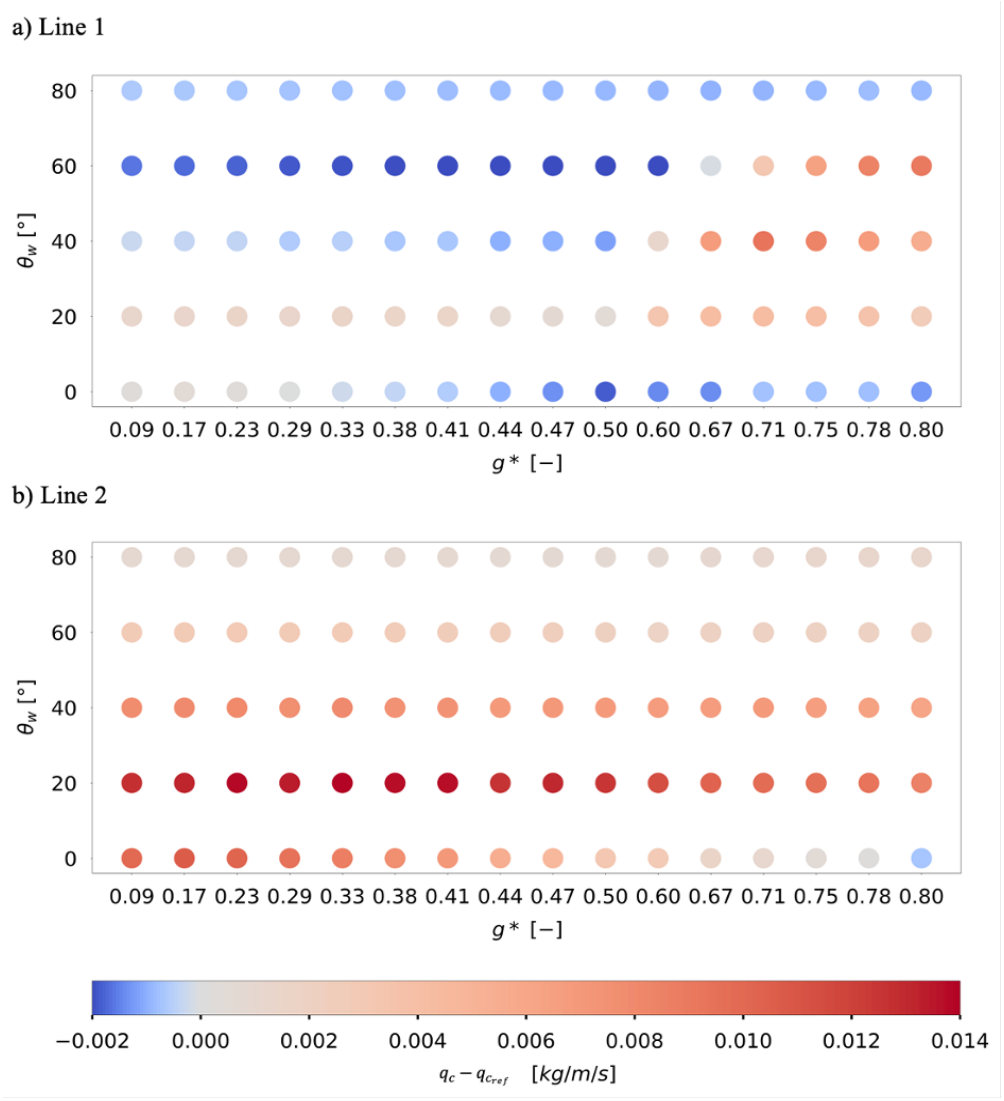

Figure 3.13: Comparison of the net impact of buildings on average duneward sediment transport flux, $q_c - q_{c_{ref}}$, between 80 different combinations of gap ratio, g^*, and the wind incidence angle, θ_w, computed along a) line 1, and b) line 2, which are located at 5 m and 70 m downstream of the row of buildings (shown in Figure 3.12), respectively.

The exact values of the average duneward sediment transport flux due to the presence of buildings, $q_c - q_{c_{ref}}$, for 80 tested simulations computed along line 1 and line 2, shown in Figure 3.13, are presented in Table 3.A.1 and Table 3.A.2, respectively, in the appendix.

3.3.4. INITIAL CHANGES IN BED ELEVATION

THE Exner equation, Eq. 4.2, is used to compute the initial bed evolution on the basis of mass continuity. This approach relates the temporal changes in bed elevation, $\partial z_b/\partial t$, to divergence or convergence in sediment transport flux, $\vec{\nabla} \cdot \vec{q}$. Figure 3.14 presents the initial erosion and deposition patterns derived from the Exner equation for three different gap ratios.

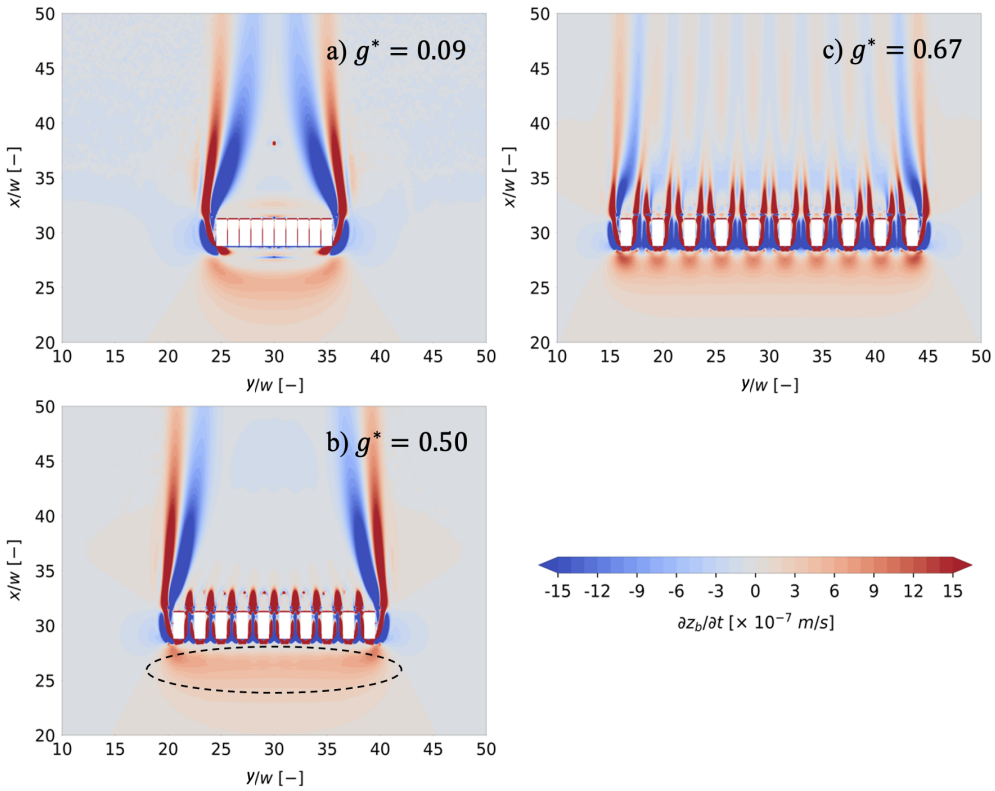

Figure 3.14: Initial erosion and deposition patterns, $\partial z_b/\partial t$, for $\theta_w = 0°$, and the gap ratio, g^*, is changed as a) 0.09, b) 0.50, and c) 0.67.

To validate the model results, the initial bed level change computed by the numerical model are qualitatively compared with the deposition pattern observed around a row of three scaled beach buildings shown in Figure 3.15. The experiments were conducted by Poppema et al. (2022b) to investigate the impact of gap spacing between scaled beach buildings, and the buildings orientation at the beach on the sediment deposition pattern that develop around buildings. Although there are some differences between the numerical and experimental model setup, the deposition patterns are comparable. The differences between field and model include the number of tested buildings in the row, buildings dimension,

wind speed, multi-directional wind at the beach, supply-limited conditions at the beach i.e. moisture, existing ripples, and other roughness elements such as shells at the beach.

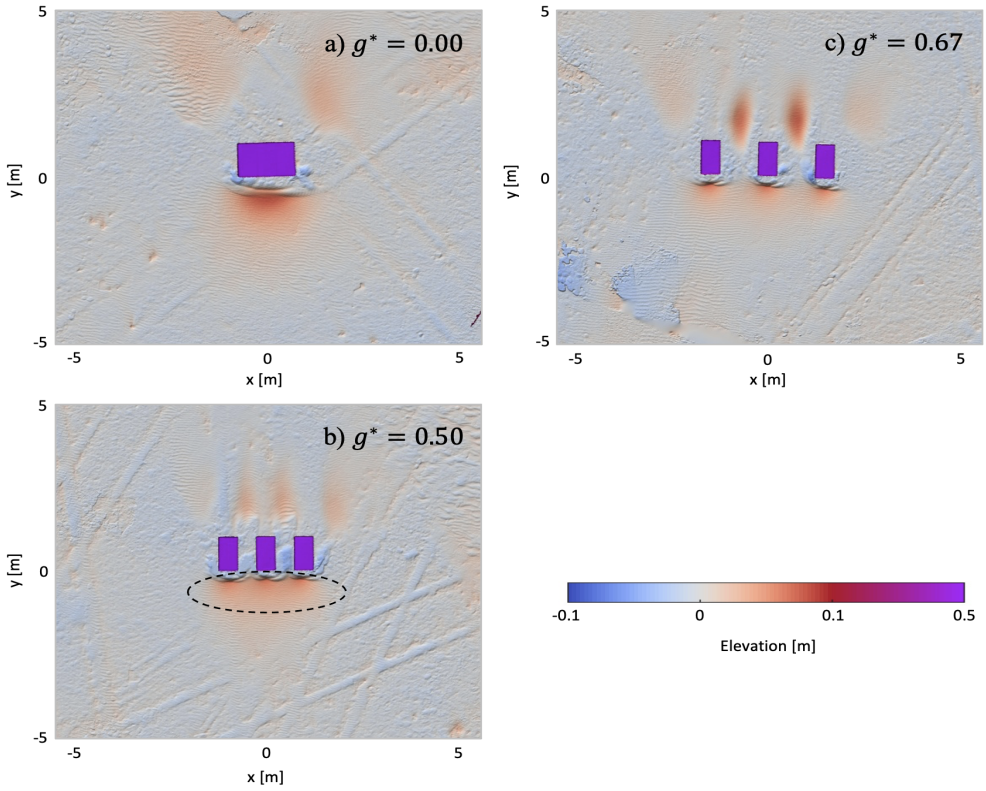

Figure 3.15: Field measurements by Poppema et al. (2022b) of bed elevation around a row of scaled beach buildings, when $\theta_w = 0°$, and the gap ratio, g^*, is changed as a) 0, b) 0.50, and c) 0.67. Figures were derived using a digital elevation model, where the elevations are computed relative to a fitted linear surface (see Poppema et al., 2022b).

As shown in both Figures 3.14a and 3.15a, in case of closely spaced buildings (beside each other at the field experiment), the row of buildings act more like a very wide building where sand deposited in the low-speed region in front of the upwind face of the large building and formed a continuous horseshoe-shaped deposition area. This upwind deposition indents in both numerical model and experiment as the gap ratio increases to 0.50 (see the black ovals in 3.14b and 3.15b). Furthermore, results show that short, triangulated deposition tails form just behind the gap spacing between two neighboring buildings. Based on the numerical results shown in Figure 3.14c, for larger gap ratio, 0.67, these inner deposition tails split up into two longer and narrower deposition tails that wrap around the buildings and continue to some extent downstream. Figure 3.15c shows a different shape of the inner deposition tails in the field. This difference might be because of the temporal changes in the wind

direction at the beach. As the wind swings between two bounding directions, two adjacent tails gradually merge, and form a single deposition tail downstream of the gaps. The darker red colors in Figure 3.14c show that the two outer deposition tails tend to become shorter as the size of the gap increases. In addition, the upwind depositions form at a closer distance relative to the upwind faces of the buildings, and their peaks become almost separate from neighboring peaks.

3.4. DISCUSSION

THE aerodynamic behavior of wind flow around adjacent beach buildings is an interesting coastal engineering problem, because of the influence that these complex flows might have on the sediment supply from the beach to the dunes. Also, the sediments might accumulate around the buildings and cause failure of the buildings structure. In addition, the arrangement of the structures can influence the sand transport directing it towards the toe or top of the dunes downstream of the buildings. The latter helps the natural flood defense functioning of the dunes. The airflow patterns that developed in the near-wake region behind the row of buildings in this study are consistent with those observed in wind-tunnel experiments of previous studies. For example, the observed variations in flow patterns for different tested gap ratios in the wind-tunnel experiments conducted by Luo et al. (2014) are comparable with our findings in Figure 3.4. Although we examined ten full-scale longitudinal buildings compared to two wide small-scale buildings tested in Luo et al. (2014), the flow mechanisms proposed by them are still recognizable in our model results. We tried a wider range of gap ratios, $g^* = 0.09 - 0.80$, compared to $g^* = 0.09 - 0.44$ of Luo et al. (2014), and observed that almost all switches in flow behavior when the gap size increases occur at a larger gap ratio than those suggested by Luo et al. (2014). Comparing their flow classification based on the mean streamlines in the near-wake region, with the streamlines in our steady-state simulations (see Figure 3.4), we observed the single-vortex flow pattern at $g^* = 0.09$, gap-enveloped flow pattern at $g^* = 0.41$, wake-interference flow pattern at $g^* = 0.47$, and at $g^* \geq 0.50$ the streamlines of our simulations seem to correspond well with their time-averaged coupled vortex-street flow pattern. Furthermore, wind-tunnel results for the coupled vortex-street mode, i.e. $g^* = 0.44$ in Luo et al. (2014), show almost symmetric counter-rotating vortices just behind the lee face of both buildings. However, the streamlines downstream of the reattachment point of flow is not fully parallel with the dominant wind direction. Therefore, the gap ratio of 0.44 appears to be the critical gap spacing below which the airflow patterns around buildings are affected by the neighboring building. Our numerical model results showed almost independent flow patterns, when $g^* \geq 0.67$ (see Figure 3.4e). At first glance, we could attribute this lag in flow patterns to the scale at which the buildings are modelled experimentally and numerically. The field experiments around

scaled buildings at the beach, performed by Poppema et al. (2022b), however showed the same critical gap ratio, $g^* = 0.67-0.75$, as observed for our numerical model results. This is likely because even though the geometrical scales in the numerical model and field experiments are different, the frontal width-to-height aspect ratio, w/h, in both our simulations and scaled models at the beach is similar, $w/h = 1$.

The difference in the length of the area with low bed shear stress (green-shaded colors in Figures 3.9b, c and d) behind the leading building in the row can be explained by the flow patterns shown in Figure 3.6. For $\theta_w = 20°$, the short face of the buildings is the windward face. The flow streamlines in the wake region downwind of the buildings are almost parallel to each other (Figure 3.6b). As the wind incidence angle increases to $\theta_w = 40°$, the wind is separated at approximately the lower left corner of the buildings. The results showed that the downwind flow behind the reattachment point of the leading building is slightly inclined compared to the direction of the downwind streamlines behind the rest of the buildings in the row (Figure 3.6c). For more oblique wind direction, $\theta_w = 60°$, the long face of the buildings is facing the wind. The buildings tend to act more like a very long building against the wind. Therefore, the vortices behind the buildings are smaller, the reattachment points downwind of the buildings get closer to the lee face of the buildings and the downwind streamlines become curved. It seems that the deflected flow around the leading building pushes the flow behind the other buildings in the row (Figure 3.6d). The wind-induced friction behind the leading building depends on the extent to which the flow momentum is being pushed by the deflected flow around the leading building. This could be an explanation for the various length of the region with low bed shear stress behind the leading building when buildings are exposed to different wind incidence angles.

Comparisons between the bed level changes based on the numerical model and field experiments show generally good agreement. However, there are some differences between numerically predicted erosion and deposition patterns and those observed at the beach. There are several reasons that can be put forth to explain the differences. The first reason is that the scale of tested buildings and the number of buildings placed besides each other in the numerical model differs from those used in the field study by Poppema et al. (2022b). In the field study, three scaled beach buildings with the length, width, and height of $1 \times 0.5 \times 0.5$ m were placed at the beach, while considering the same frontal aspect ratio, we tested ten full-scale buildings of size $6 \times 2.5 \times 2.5$ m. Secondly, the actual wind field at the beach is unsteady, with the wind direction and speed show strong variations over time, whereas in the model the wind speed and direction are not varying. Although, the one-day experiments by Poppema et al. (2022b) limits the variations in wind condition, the variations could potentially influence the shape and size of the bed topography patterns. Thirdly, we considered the transport-limited (i.e., not supply-limited) condition in our model, such that the bed of

the numerical domain can unlimitedly provide sediment particles. The bed in the model is fully dry and flat, and consists of non-cohesive and uniformly-graded particles. However, there are some adverse impacts at the real beach bed that lead to the supply-limited condition, in which the capability of the bed to supply sediment particles becomes limited. Conditions that limit the sediment availability at the beach include bed moisture content, vegetation, ripples, sediments sorting, slope, and beach armoring (Delgado-Fernandez, 2010; Nolet et al., 2014; Silva et al., 2018; Hoonhout and De Vries, 2019). This might be the reason for the differences observed in the deposition region around scaled beach buildings, and more horse-shoe shaped deposition in the numerical model. Finally, we assumed a uniform aerodynamic roughness length, z_0, for the bed surface of the numerical model domain, but uniformity is not likely in reality where grains of different sizes occur and small-scale bedforms will also influence the roughness. Next to this the bed level changes derived from Exner equation, are the initial patterns developed at a flat beach where the local morphological feedback has not been taken into account. The erosion and deposition patterns developed around buildings change the beach topography, which might locally influence the wind speed and direction, and in turn alter the wind-induced shear stresses. Furthermore, the actual beach bed consists of spatially different roughness. This is due to the existence of shells, vegetation, and sand grains with different sizes. Although the abovementioned differences between the actual beach situations and our model assumptions exist, the comparisons between the field observations and our numerical model results are in good agreement.

3.5. CONCLUSION

THIS study aims to understand how the airflow characteristics and wind-induced bed shear stress, which directly affect the sediment transport and bed topography, are influenced by the positioning of buildings at the beach. This research focused on a row of ten buildings having systematic changes in the gap spacing between two neighboring buildings, and the incident wind direction relative to the buildings.

Our findings showed that the gap ratio, g^*, between neighboring buildings is a key parameter in flow behavior and resulting bed shear stress in the vicinity of buildings, which determines the sediment transport and bed elevation around and in between buildings. We found that the flow through the gap between buildings placed very close to each other, $g^* = 0.09$, is limited. Therefore, the increased bed shear stress through the gaps is not apparent, and the results showed no deposition in the lee of the gaps. The closely-spaced buildings mainly act as a single building, creating a continuous large horseshoe-shaped deposition region starting at some distance upstream of the upwind faces of the buildings.

Furthermore, two deposition tails develop around the corner buildings in the row and extend downstream of the buildings.

The flow through the larger gap spacings, i.e. $g^* > 0.50$, significantly increases due to funneling effects, while the wind speed begins to decrease afterwards. This flow deceleration causes some of the sediment in transport to be deposited as so-called sand drift in the lee of the gaps. In addition, our findings showed that the upwind deposition becomes indented and develops at a closer distance relative to the upwind faces of buildings for larger gap ratios. For $g^* \geq 0.67$, both flow patterns and initial erosion and deposition patterns develop mostly independent from neighboring buildings. The jet flows passing through gaps between buildings remain parallel to the incident wind, and the separated flows from upwind edges of each building create a pair of opposing vortices just behind the lee face of buildings without interfering with the airflow around adjacent buildings. The upwind deposition peaks become separated from each other, and the length of the outer deposition tails decreases and becomes almost equal to inner deposition tails. It should be noted that the sand drifts no longer develop downstream of the gaps, and instead two deposition tails wrap around individual buildings and extend farther downstream than sand drifts in $g^* < 0.67$ conditions.

Another key factor that largely affects the size and the location at which the vortices form around buildings, is the wind incidence angle. Depending on the dominant wind direction, the separation bubble downwind buildings might locate behind the smaller face of the buildings or in between two neighboring buildings and close to the longer face. The latter would obstruct the incoming wind from entering the gap spacing and moving downstream towards the dunes. On the other hand, the wind entering the narrow space bounded on one side by the outer edges of the recirculation vortex downwind of the building, and on another side by the diverted flow from the sharp edge of the next building, experiences a funneling effect. Upon leaving this narrow gap, the flow expands and decelerates downstream, leading to the formation of larger sand drifts. It is noteworthy that these flow behaviors strongly depend on the gap spacing between buildings and the dimension of the buildings. Furthermore, we found that for $\theta_w \geq 60°$, the streamlines behind the flow reattachment point downstream of the second to the last building, are influenced by the diverted flow from the sharp edges of the most upwind building in the row. This leads to slightly bent streamlines directly behind the reattachment point instead of straight streamlines parallel with the dominant wind direction. As wind direction increases to $\theta_w = 80°$, the flow pattern around buildings is mostly similar to those developed around a very long building, when the wind is almost perpendicular to the shorter face of the long building. Therefore, results show that the orientation of vortices form just behind the downwind face of buildings change for 90 degree compared to less oblique winds (the longer diagonal of the elliptical vortices in x

direction).

To determine the combined impact of gap spacing and wind direction on sediment transport rate towards the dunes behind the row of buildings, we determined the average of transport flux along two different lines located at 5 m and 70 m downstream of the buildings. We have checked other distances as well, and have seen that 5 m and 70 m are representative of a typical location of a dune foot and a location well inside the dunes, respectively. The average sediment transport along these lines was used as the representative numbers for duneward sediment transport that could be compared between 80 different combinations of the gap ratio and wind direction. This approach is useful for coastal designers to compare complex building configurations and find an optimal building positioning at the beach to minimize the dunes erosion or enhance the dunes growth. We found that, different than our expectations, buildings might have positive effects on the duneward sediment transport. Complex flow patterns develop as a result of the presence of buildings at the beach, which could steer more sediments to the dunes. Results showed the maximum duneward sediment transport across a line 5 m downwind of the buildings occurs when $g^* = 0.71$ and $\theta_w = 40°$; while the maximum along 70 m downwind of the buildings would occur for the combination of $g^* = 0.33$ and $\theta_w = 20°$. Therefore, these findings motivate further research whether an optimum distance exists between a row of beach buildings and the dune foot so that it maximally promotes the sediment transport from the beach to the dunes under natural (variable) wind conditions.

ACKNOWLEDGMENTS

This research is part of the ShoreScape project, which is a joint research project of the University of Twente and Delft University of Technology. ShoreScape focuses on sustainable co-evolution of the natural and built environment along sandy shores. This research was funded by Netherlands Organisation for Scientific Research (NWO) (contract number ALWTW.2016.036) and co-funded by Rijkswaterstaat (RWS) and Hoogheemraadscap Hollands Noorderkwartier (HHNK).

3.A. APPENDIX

Table 3.A.1: Net buildings-induced average duneward sediment transport flux, $q_c - q_{c_{ref}}$ [$\times 10^{-4}$ kg/m/s], along line 1 for 80 different combinations of gap ratio, g^*, and the wind incidence angle, θ_w, corresponding to Figure 3.13a.

θ_w \ g^*	**0.09**	**0.17**	**0.23**	**0.29**	**0.33**	**0.37**	**0.41**	**0.44**
0	2.36	4.46	2.49	−0.13	−2.04	−3.68	−5.64	−9.91
20	13.04	13.68	16.20	13.51	16.36	15.12	14.73	9.47
40	−2.81	−3.59	−3.78	−5.89	−5.01	−6.79	−6.63	−9.91
60	−16.15	−17.18	−17.96	−18.83	−19.28	−19.75	−20.16	−20.70
80	−6.10	−6.50	−6.88	−7.26	−7.59	−7.87	−8.18	−8.49
θ_w \ g^*	**0.47**	**0.50**	**0.60**	**0.67**	**0.71**	**0.75**	**0.78**	**0.80**
0	−13.45	−18.50	−14.17	−13.85	−7.40	−7.58	−7.90	−12.78
20	7.99	4.94	33.28	41.79	41.64	40.86	35.06	26.94
40	−10.12	−11.85	12.51	68.07	93.78	83.64	68.77	55.92
60	−20.94	−21.66	−21.26	−0.84	32.05	64.34	84.81	90.07
80	−8.60	−8.81	−9.36	−9.60	−9.34	−8.66	−8.25	−8.69

Table 3.A.2: Net buildings-induced average duneward sediment transport flux, $q_c - q_{c_{ref}}$ [$\times 10^{-4}$ kg/m/s], along line 2 for 80 different combinations of gap ratio, g^*, and the wind incidence angle, θ_w, corresponding to 3.13b.

θ_w \ g^*	**0.09**	**0.17**	**0.23**	**0.29**	**0.33**	**0.37**	**0.41**	**0.44**
0	100.57	106.33	101.86	94.79	86.67	77.29	70.83	55.24
20	127.86	131.74	138.81	133.85	142.54	137.17	137.25	126.64
40	77.80	79.14	80.90	77.21	79.78	75.08	74.91	69.14
60	27.84	27.73	28.45	27.64	27.93	27.01	26.16	24.09
80	9.09	9.13	9.10	9.10	9.30	9.20	8.88	8.27
θ_w \ g^*	**0.47**	**0.50**	**0.60**	**0.67**	**0.71**	**0.75**	**0.78**	**0.80**
0	46.64	32.15	28.68	15.38	11.20	4.44	1.40	−6.90
20	130.17	125.59	114.78	103.09	98.37	95.82	93.17	86.06
40	70.74	69.10	67.08	66.87	69.17	66.23	64.51	61.93
60	23.07	21.42	18.13	20.02	20.18	19.15	19.26	19.25
80	8.73	8.53	8.63	10.39	11.38	12.24	12.50	12.51

4

THE INFLUENCE OF ELEVATED BUILDINGS ON AIRFLOW PATTERNS, SEDIMENT TRANSPORT PATTERNS AND FORCED BED MORPHOLOGY

This chapter is accepted (in publishing process) as Pourteimouri, P., Campmans, G. H. P., Wijnberg, K. M. and Hulscher, S. J. M. H. (2023). Modelling the influence of beach building pole heights on aeolian morphology and downwind sediment transport. *Geomorphology*

ABSTRACT: Beach buildings locally change the near-bed airflow structures. The building-induced changes in airflow influence the aeolian sediment transport patterns, hence the morphologic developments around buildings. Buildings at the beach are often placed on poles. To quantify the influence of different pole heights, three-dimensional simulations have been performed making use of OpenFOAM which is an open-source computational fluid dynamics solver. Simulations were performed, in which we modelled a row of ten full-scale beach buildings placed on a flat/smooth bed surface. A constant gap size between neighbouring buildings and the perpendicular wind direction were used. The pole height was systematically varied from zero, when buildings are placed directly at the beach, to higher pole heights. The airflow patterns showed the flow acceleration underneath the elevated buildings and through the gaps between neighbouring buildings. The Exner equation together with the Bagnold's sediment transport flux formulation, and a newly-developed model that couples the airflow model with a sediment transport model, AeoLiS, were used to model the initial and further-developed aeolian morphologic developments around buildings. The effective sediment transport flux across various lines in the long-shore direction downstream of the buildings was computed. Our study revealed that, depending on the height of the poles, the buildings can have a significant effect on sediment transport. They can either steer sediment transport downwind or block it from moving in that direction, such as by preventing sediment from being transported upwind of the buildings.

4.1. INTRODUCTION

THE use of sandy beaches for recreation and tourism leads to the construction of hotels, restaurants, seasonal beach houses and pavilions at the beach-dune interface (Figure 4.1a). Depending on their dimension, geometry, material composition, orientation, elevation from bed and positioning at the beach, these buildings affect the wind field close to the bed (Jackson and Nordstrom, 2011). Inevitably, the changes in near-bed airflow due to human-made structures determine the aeolian sediment transport and the source-to-sink relationships in sandy substrates such as beaches (Nordstrom et al., 2000). The flow deceleration upwind of the buildings and in the shadow zone just behind the buildings decreases the wind-induced sediment carrying capacity. This results in a decreased sediment transport flux and subsequently in deposition of the sediments from the airflow (Cooke et al., 1993; Qian et al., 2011; Jackson and Nordstrom, 2011; Luo et al., 2012). Conversely, the flow acceleration occurs as the air moves around the buildings, through the gaps between neighbouring buildings and underneath the elevated buildings. The acceleration zone enhances the sediment transport potential and hence causes surface erosion (Iversen et al., 1991; Luo et al., 2014; Luo et al., 2016; Smith et al., 2017; Tominaga et al., 2018).

The aforementioned building-induced flow perturbations influence the sediment supply from the beach towards the dunes. This process might disrupt the natural processes in a way that the alterations to the sand dune system negatively affects its flood safety functioning (Nordstrom and McCluskey, 1984). On the other hand, many researchers believe that buildings at the beach cause both positive and negative impacts on the dune systems (i.e. both growth and erosion) (García-Romero et al., 2016; Smith et al., 2017). Buildings at the beach do not always separate aeolian sand dunes from the sediment sources at the beach, while they can also be used to enhance the sediment transport and improve sand dunes (Nordstrom et al., 2000). It is also noteworthy that buildings at the beach trap aeolian depositions (Figures 4.1b and c). This becomes problematic for buildings functioning and might block the entrance to the buildings over a longer time period. To prevent ongoing sediment accumulation and subsequent need for sediment removal measures, building owners sometimes use alternative solutions such as placing buildings on poles (Figures 4.1d and e).

An understanding of the airflow and sediment transport patters underneath and around buildings on poles would provide important insights for both the building owners to choose a specific pole height, and the coastal management authorities who determine the regulations for placing buildings at the beach, considering both the recreational demands and the nature-based flood defense strategies. Previous studies on the morphological impacts of beach buildings have focused primarily on identifying the erosion and deposition patterns that form around buildings on the sedimentary bed (Bagnold, 1941; Pye and Tsoar,

(a) (b) (c) (d) (e)

Figure 4.1: Buildings at the beach-dune interface. a) Different types of beach buildings at the Scheveningen beach, the Netherlands. b) A restaurant with heavy sediment deposition around at the Noordwijk beach, the Netherlands. c) A building with some sediment deposition behind the downwind face at the Noordwijk beach, the Netherlands. d, e) A row of beach buildings on poles at the Kijkduin beach, the Netherlands.

2008; McKenna Neuman and Bédard, 2015; Tominaga et al., 2018), and how these patterns depend on buildings characteristics such as geometry and size (Iversen et al., 1991; Cooke et al., 1993; Poppema et al., 2021; Pourteimouri et al., 2022) as well as buildings positioning such as orientation and spacing from each other (Luo et al., 2012; Luo et al., 2014; Luo et al., 2016; Poppema et al., 2022b; Pourteimouri et al., 2023). Beach buildings are frequently placed on poles, however a scientific study on bed level changes surrounding elevated buildings and to what extent they influence the duneward transport depending on

the pole height is missing. Furthermore, the abovementioned studies are mostly conducted using scale models of beach buildings in the field or in a wind-tunnel with sandy bed. The study by Poppema et al. (2021) contains a field observation of erosion and deposition patterns around a full-scale beach building. However, performing a wide range of studies with systematic changes in pole heights, using such a large building is not easily applicable at the beach.

The goal of this study is to quantify the influence of a row of full-scale elevated buildings on airflow, morphological changes at the bed and the sediment delivery from the beach through the buildings to the dunes as a function of building pole height. Firstly, the three-dimensional numerical CFD model (Pourteimouri et al., 2022) is used to simulate airflow around buildings and calculate the wind shear stress at the bed, sediment transport fluxes, and initial rate of change in bed elevation. Secondly, the CFD model is coupled with AeoLiS (Hoonhout and De Vries, 2016), which is a process-based sediment transport model, to compute aeolian bed evolution around buildings. Thirdly, we compared the bed topography results obtained by different sediment transport methods used in this study.

This study will answer three research questions: Q1) How does the near-bed wind field change when beach buildings are placed on poles?; Q2) How do the sediment transport and bed elevation change when buildings are placed on poles?; Q3) To what extent does the duneward aeolian sediment transport through the buildings depend on pole heights?

4.2. METHODOLOGY

4.2.1. NUMERICAL MODEL SETUP

IN this study, the airflow and wind-induced erosion and deposition patterns around a row of ten full-scale beach buildings on poles (with square cross-section) are modelled using the OpenFOAM model developed by Pourteimouri et al. (2022). The beach buildings are typically placed in a row with small gaps between them and a greater distance from the neighboring rows. The number of beach houses varies from one beach to another, but to maintain consistency with what we observed at the beach, we selected this configuration with ten buildings placed in close proximity to each other and a larger gap at the sides of the two outermost buildings. The impact of systematic changes in poles height on airflow and bed morphology around buildings is then studied. The three-dimensional simulations are conducted using the simpleFOAM solver, which solves Reynolds-averaged Navier-Stokes (RANS) equations for steady, incompressible, and turbulent flows. The simpleFOAM solver uses the Finite Volume Method (FVM) for Pressure-Linked Equations (SIMPLE) to solve the flow equations. The well-known $k-\varepsilon$ turbulence closure model is applied to simulate the

turbulent flows over the beach and around the buildings. Figure 4.2 displays a commonly-used building configuration at the beach-dune interface where a periodic row of buildings is seasonally placed in the along-shore direction, y. The dimensions used in this study are presented in Table 4.1. It is noteworthy that beach buildings come in various sizes, ranging from small changing cabins to large holiday cottages and restaurants. For the purposes of this study, we focused primarily on holiday cottages, which are identical buildings placed in periodic rows close to each other along the beach. Although the size of these holiday cottages can vary significantly, we based our dimensions on the standard size of a shipping container, which was used in an earlier comparison of model results to field observations (Pourteimouri et al., 2022). The dimensions of a shipping container are in the same range as found for the holiday cottages at the beach.

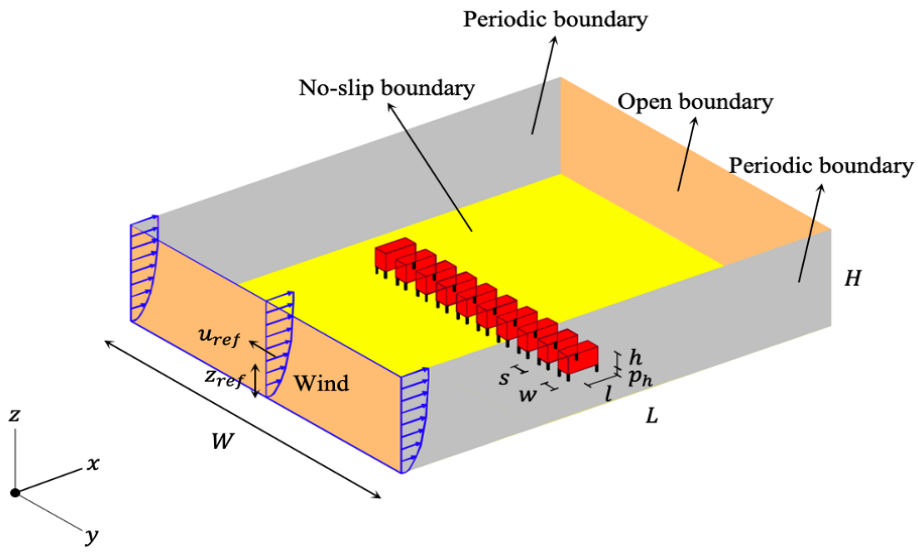

Figure 4.2: Schematic design of buildings configuration at the beach-dune interface. The highlighted area shows the numerical model setup. The logarithmic wind velocity profile is applied at the inlet of the computational domain, $x = 0$ m. The wind direction is perpendicular to the front face of buildings.

The computational grids within the numerical domain are generated using an automated meshing utility, cfMesh. The finest grid size is of order $\Delta x = \Delta y = \Delta z = 0.125$ m adjacent to the buildings on poles and bed surface, while the coarsest grid size of $\Delta x = \Delta y = \Delta z = 0.75$ m is used farther away from the buildings and bed. This grid combination creates a total of about 2.7 million cells. The logarithmic wind velocity profile is prescribed using the reference wind speed of $u_{ref} = 17$ m/s at the reference elevation of $z_{ref} = 1.8$ m. This reference wind speed was selected based on field measurements taken at Noordwijk beach in the Netherlands using the WindSonic anemometer by Poppema et al. (2021). To ensure a repre-

sentative wind speed for actual sediment transport, an average of the measured wind speed over a period of three storm days was taken. The uniform roughness height of $z_0 = 0.00001$ m is used at the bed surface of the domain that was derived based on the median grain size at the beach ($d = 3.00 \times 10^{-4}$) m. The boundary conditions used in this study are shown in Figure 4.2. The slip boundary condition is used for the top boundary of the domain. The periodic boundary condition is employed at the lateral sides of the computational domain. This allows for oblique winds, used in Pourteimouri et al. (2023), but in this paper these boundaries may as well be free slip walls. To accurately capture the flow behavior near the solid walls, we used a combination of the wall function approach and a near-wall resolving approach. The wall function approach is used to bridge the viscosity-affected region near the bed, without resolving it explicitly. Meanwhile, the near-wall resolving approach involves defining thin boundary layers and implementing local refinement near the building walls and poles, allowing us to resolve the near-wall flow region. More detailed description of the model, flow equations and implementation of boundary conditions can be found in Pourteimouri et al. (2022).

Table 4.1: Model domain and beach buildings data.

Variable	**Value [m]**
Domain length (L)	150.00
Domain width (W)	150.00
Domain height (H)	30.00
Buildings length (l)	6.00
Buildings width (w)	2.50
Buildings height (h)	2.50
Poles length (p_l)	0.50
Poles width (p_w)	0.50
Poles height (p_h)	$0 - 7.50$
Gap between buildings (s)	2.50

4.2.2. AEOLIAN SEDIMENT TRANSPORT

IN case the magnitude of the wind-induced shear velocity, $\overrightarrow{u_*}$, exceeds a threshold value, $u_{*_{th}}$, the sediment grains come into motion. In this study, we model aeolian sediment transport using two different methods that are explained below.

4.2.2.1. METHOD 1: INSTANTANEOUS BAGNOLD FORMULATION

IN the first method, the theoretical sediment transport flux, $\overrightarrow{q}$ [kg/m/s], is computed using the modified Bagnold's equation (Bagnold, 1937) proposed by Nickling and Neuman (2009):

$$\overrightarrow{q} = C\frac{\rho_a}{g}\sqrt{\frac{d}{D}}(|\overrightarrow{u_*}| - u_{*_{th}})^3\frac{\overrightarrow{u_*}}{|\overrightarrow{u_*}|} \tag{4.1}$$

with the empirical constant $C = 1.80$ [-]; the air density $\rho_a = 1.29$ [kg/m^3]; the gravitational acceleration $g = 9.81$ [m/s^2]; the sediment grain size $d = 3.00 \times 10^{-4}$ [m]; the reference sediment grain size $D = 2.40 \times 10^{-4}$ [m]; the wind shear (friction) velocity $\overrightarrow{u_*} = \sqrt{|\overrightarrow{\tau}|/\rho_a}\overrightarrow{\tau}/|\overrightarrow{\tau}|$ [m/s]; the bed shear stress $\overrightarrow{\tau}$ [N/m^2]; the threshold shear velocity $u_{*_{th}} = A\sqrt{[(\rho_s - \rho_a)/\rho_a]gd}$ [m/s]; the sediment density $\rho_s = 2.65 \times 10^3$ [kg/m^3]; and the constant $A = 0.1$ [-] (Nickling and Neuman, 2009).

We are interested in erosion and deposition patterns around buildings on poles of different heights. Therefore, the Exner equation is used which predicts the bed level changes based on the mass conservation between the sediment in sandy substrate, i.e. beaches, and sediment grains that are being transported (Bauer et al., 2015):

$$\frac{\partial z_b}{\partial t} = -\frac{1}{\rho_s(1-n)}\overrightarrow{\nabla}\cdot\overrightarrow{q} \tag{4.2}$$

with the bed elevation z_b [m]; the time t [s]; and the sediment porosity $n = 0.40$ [-].

It should be stated that the Bagnold's transport equation is only valid under transport-limited conditions in which the wind properties are steady, and the sandy bed can endlessly provide dry sediment. In addition, Bagnold's transport equation only considers horizontal uniform flows. Consequently, the theoretical equations for modelling aeolian sediment transport mostly overpredicts sediment transport since other transport limiting factors are not taken into account (Sherman and Li, 2012). Although limitations in sediment budget at the beach are typically incorporated in empirical models using calibration parameters, it is still a challenging issue to account for real beach conditions where the bed features and thus the sediment availability changes in both space and time.

4.2.2.2. METHOD 2: COUPLING BETWEEN OPENFOAM AND AEOLIS

IN the second method, the process-based numerical model AeoLiS (Hoonhout and De Vries, 2016), is used. This model was developed to simulate wind-blown sediment transport. Unlike the Bagnold's transport equation, AeoLiS can also takes the impacts of supply-limited conditions into account. These supply-limiting factors, that influence the amount

of active sediment and thus reduce the sediment transport include bed moisture, vegetation, salt crusts, grain size and sorting, bed slope, beach armoring and non-erodible roughness elements (Delgado-Fernandez, 2010; Hoonhout and De Vries, 2019). AeoLiS is capable of simulating aeolian sediment transport in the case of varying sediment budget in both space and time.

Aeolian sediment transport in AeoLiS is modelled using a two-dimensional advection equation proposed by De Vries et al. (2014):

$$\frac{\partial c}{\partial t} + u_{s,x}\frac{\partial c}{\partial x} + u_{s,y}\frac{\partial c}{\partial y} = E - D \tag{4.3}$$

with the sediment concentration per unit area in the air c [kg/m^2]; the time t [s]; the saltation velocity of the sediment grains in x direction (cross-shore) $u_{s,x}$ [m/s]; the saltation velocity of the sediment grains in y direction (along-shore) $u_{s,y}$ [m/s]; the potential erosion rate E [kg/m^2/s]; and the potential deposition rate D [kg/m^2/s]. The saltation velocity is computed using the method proposed by Sauermann et al. (2001). The right-hand side of the Eq. 4.3 denotes the net sediment entrained from the sandy bed, and is computed using the following equation (De Vries et al., 2014):

$$E - D = \min\left(\frac{c_{eq} - c}{T}, \frac{\partial m_a}{\partial t}\right) \tag{4.4}$$

with the equilibrium (saturated) sediment concentration per unit area in the air c_{eq} [kg/m^2]; the saltation timescale for sediment grains T [s] that is assumed to be equal to the timescale of both erosion and deposition; and the sediment budget at the bed m_a [kg/m^2].

The equilibrium sediment concentration, c_{eq}, is computed using a theoretical aeolian sediment transport model, i.e. the Bagnold's formulation shown in Eq. 4.1:

$$c_{eq} = \frac{|\vec{q}|}{|\vec{u_s}|} \tag{4.5}$$

Up to now, the wind-induced bed shear stress in AeoLiS, $\vec{\tau}$ [N/m^2], was computed using the following equation:

$$\vec{\tau} = \vec{\tau_0} + |\vec{\tau_0}|\delta\vec{\tau} \tag{4.6}$$

with the uniform bed shear stress only due to wind $\vec{\tau_0}$ [N/m^2]; and the bed shear stress perturbation due to the interaction between the wind field and the bed morphology $\delta\vec{\tau}$

[N/m^2]. The latter term is estimated based on the analytical method suggested by Weng et al. (1991) and Kroy et al. (2002) in which a more accurate non-logarithmic wind field close to the surface of a smooth topography is estimated. It should be noted that the above equation is only valid for gentle slopes such as smooth hills or aeolian sand dunes outside their slip face (lee face).

To simulate morphologic changes around buildings with steep (vertical) walls, a new coupled model that links the airflow model, OpenFOAM, with the sediment transport model, AeoLiS, is developed. The new conceptual approach used in this study is shown in Figure 4.3. The 3D steady-state OpenFOAM model, described in 4.2.1, is run to compute the wind field around a row of beach buildings that are located on an initially flat sandy bed, $z_b = 0$ m. Instead of using Eq. 4.6, the wind-induced bed shear stress computed by OpenFOAM is derived for the grid point locations in AeoLiS. AeoLiS is then run to compute the bed topography over a period of 20 hours, using the constant in time bed shear stress field provided by OpenFOAM. As long as bed changes are small, the changes in flow induced bed shear stress are assumed to be small compared to the large-scale shear stress field effects caused by the buildings. The changes in bed elevation around buildings influence the wind field close to the surface hence the bed shear stress needs to be updated via OpenFOAM with the new bed topography. Therefore, the OpenFOAM model containing buildings on new bed topography is run to update the bed shear stress that will be used in AeoLiS for the next round. This iterative coupling of OpenFOAM and AeoLiS is continued from the initial time, $t_0 = 0$ s, until the end of the simulation, here $t = 80$ hours. It is noteworthy that the internal time step used in AeoLiS is equal to $\Delta t_{int} = 60$ s, which is different from the time interval that the bed shear stress recalculated by OpenFOAM.

4.3. RESULTS

4.3.1. NEAR-BED, TOP VIEW VELOCITY FIELD

THE wind velocity field in the horizontal plane near the bed, $z = 0.25$ m, around buildings without and with poles is shown in Figure 4.4. The corresponding streamline patterns are shown in Figure 4.5. The distance in streamwise and spanwise directions as well as the poles height are converted to dimensionless parameters expressed as x/w, y/w and p_h/w, respectively. Figure 4.6 compares the dimensionless streamwise component of velocity, u_x/u_{ref}, along two different lines L_{x_1} and L_{x_2} shown in Figure 4.4, for buildings without and with poles. L_{x_1} passes the center of the one of the two central buildings, while L_{x_2} is the domain centerline.

For buildings placed directly on the beach surface, $p_h/w = 0$, the incident wind can only

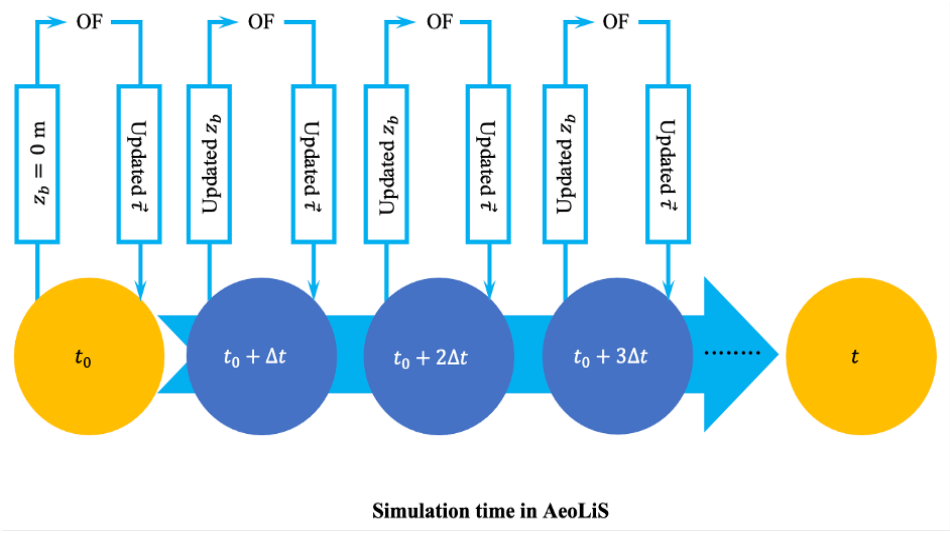

Figure 4.3: New conceptual approach for coupling between OpenFOAM and AeoLiS. The OF is the abbreviation for OpenFOAM.

flow through the gaps between buildings and over the top of the buildings. Figure 4.4a shows small regions with low velocities (dark blue colors) in front of the windward faces of the buildings. A negative x component of velocity, showing the existence of reversed vortex flow, forms upstream of the buildings (see the blue crosses in Figure 4.6a). The jet flow between the two neighbouring buildings is constrained due to the funneling effect, and the wind velocity through the gap increases to about 2.7 times the wind velocity just in front of the gap (see the blue crosses in Figure 4.6b). This flow acceleration could increase the sediment transport capacity. On the other hand, the flow is expanding and decelerating just behind the gaps, as shown in Figure 4.6b, that might result in lowering of the sediment transport capacity hence the sediment deposition. Furthermore, the streamlines pattern shows a pair of vortices that are rotating in opposite directions immediately behind the lee face of the buildings (Figure 4.5a). These so-called separation bubbles are characterized by lowest wind velocities in the vicinity of buildings (Figure 4.6a).

As buildings are placed on poles, $p_h/w = 1$, the incident wind not only flows through the gaps and over the buildings but also underneath the buildings (Figure 4.5b). The minimum near-bed streamwise wind velocity in front of the buildings on poles and buildings directly on the bed surface reaches almost 0.4 and -0.1 times the velocity of the undisturbed flow far away from the buildings, respectively. Results reveal that the velocity in front of the buildings on poles decreases more gradually compared to the case when buildings are placed directly on the beach surface (see the green crosses in Figure 4.6a). This means that build-

ings on poles impact a larger area upwind of the buildings (Figure 4.4b). As the wind enters the gap between the bed and the lower face of the buildings, the flow is substantially accelerated. The flow acceleration is slightly higher at the beginning and end of the pathway underneath the buildings due to additional flow compression in between the poles (Figure 4.6a). Downwind, the wind velocity decreases both behind the buildings (Figure 4.6a) and behind the gaps (Figure 4.6b), however the slope of the curve behind the buildings is greater than behind the gaps.

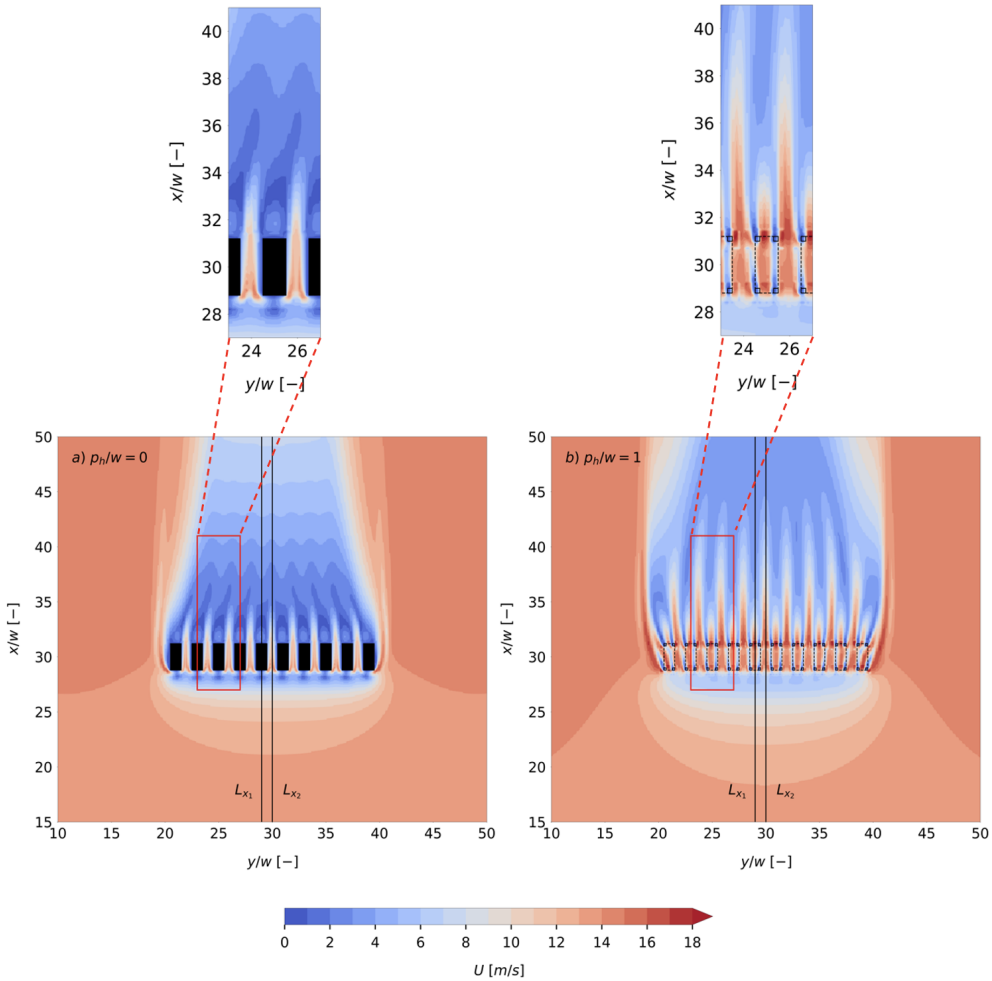

Figure 4.4: Spatial distribution of wind velocity magnitude, U, at a horizontal near-bed plane, $z = 0.25$ m, for a) buildings on the beach surface, $p_h/w = 0$, and b) buildings on poles, $p_h/w = 1$. For buildings on poles, the small solid rectangles show the exact location of the poles, while the large, dashed rectangles show the projection of buildings on the near-bed horizontal plane.

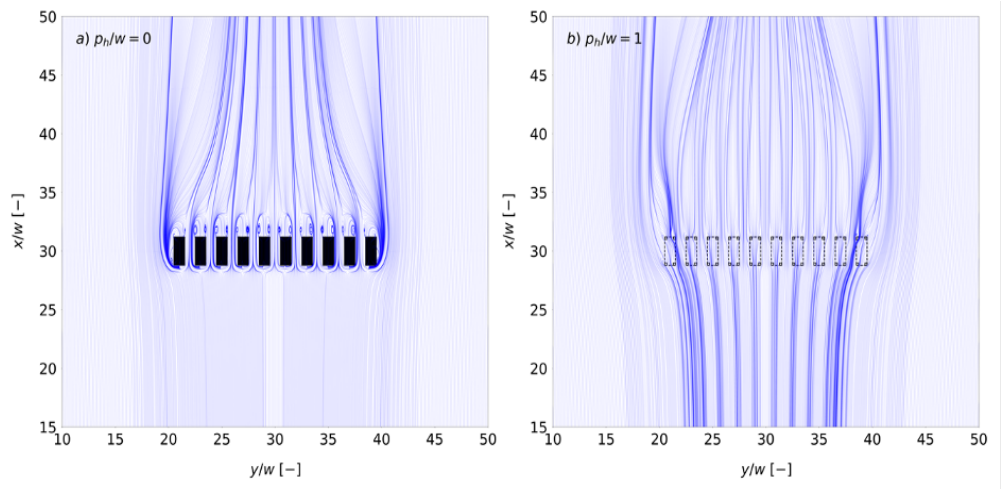

Figure 4.5: Patterns of the flow streamlines at a horizontal near-bed plane, $z = 0.25$ m, for a) buildings on the beach surface, $p_h/w = 0$, and b) buildings on poles, $p_h/w = 1$. The streamlines are only based on horizontal flow components.

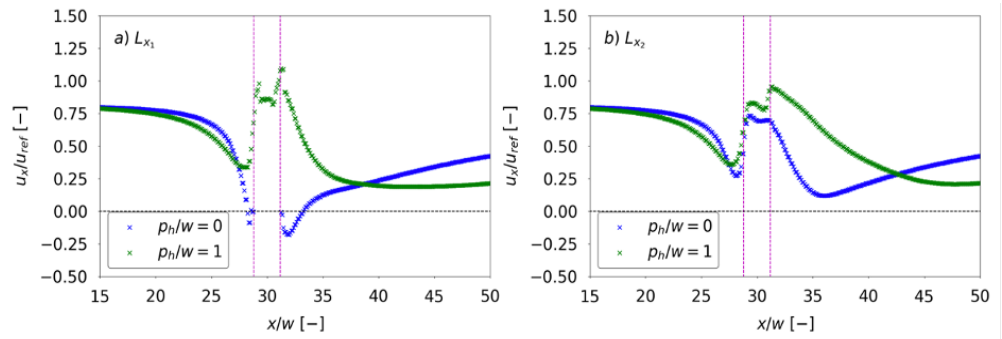

Figure 4.6: Streamwise wind velocity, u_x, distribution at a horizontal near-bed plane, $z = 0.25$ m, along the a) centerline of one of the two central buildings, and b) domain centerline (respectively L_{x_1} and L_{x_2} shown in Figure 4.4) for buildings on the beach surface and buildings on poles. The purple dashed lines show the beginning and end positions of the buildings in x direction.

4.3.2. SIDE-VIEW VELOCITY FIELD

THE wind velocity field in the vertical plane passing the center of one of the two central buildings (along L_{x_1} shown in Figure 4.4), $y = 72.5$ m, in the case of buildings directly on the beach surface and on poles is shown in 4.7. To provide more detailed information on how the vertical distribution of the wind velocity changes in the vicinity of buildings, the streamwise wind velocity is presented at the eight different locations along lines L_{z_1} to L_{z_8} in Figure 4.7. The corresponding results are shown in Figure 4.8.

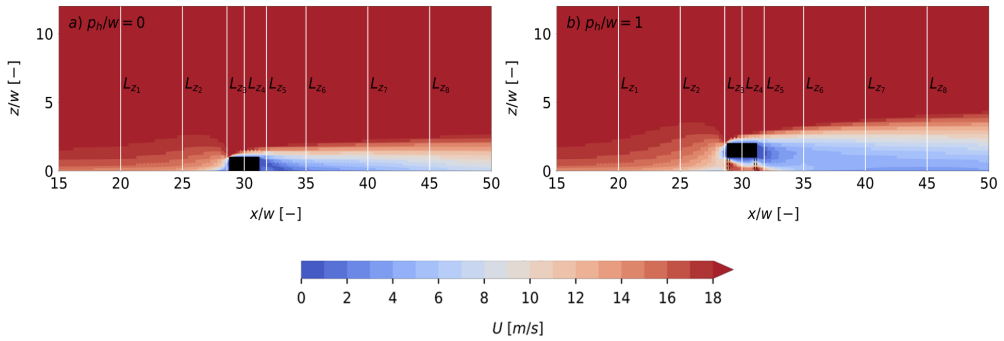

Figure 4.7: Spatial distribution of wind velocity magnitude, U, at a vertical plane passing the centerline of the one of the two central buildings (along L_{x_1} shown in Figure 4.4), y = 72.5 m, for a) buildings on the beach surface, $p_h/w = 0$, and b) buildings on poles, $p_h/w = 1$. The streamwise wind velocity along vertical profiles, L_{z_1} to L_{z_8}, will be presented and discussed later.

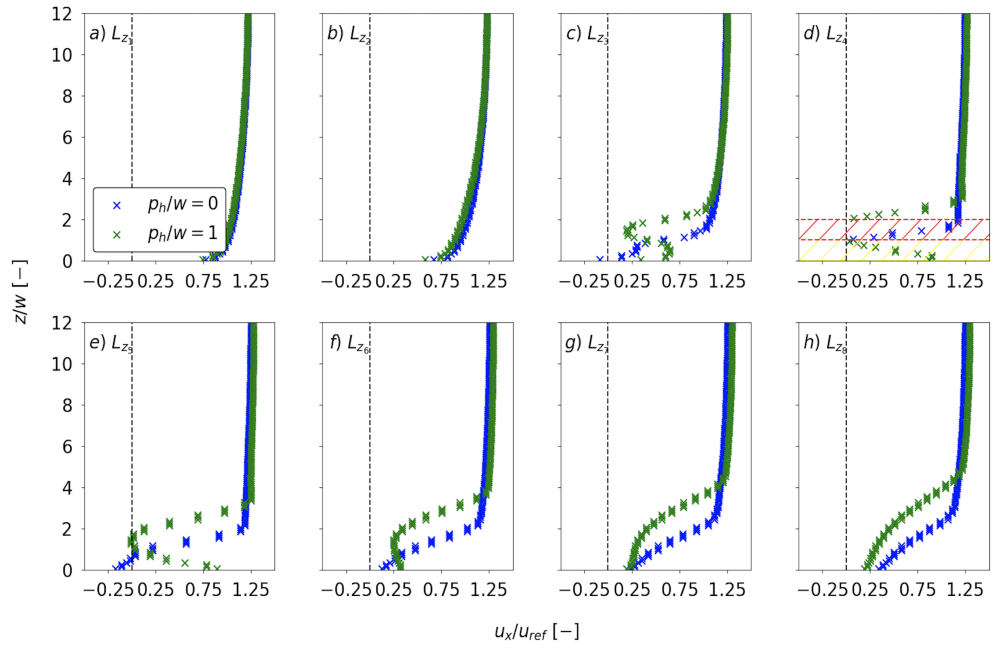

Figure 4.8: Streamwise wind velocity, u_x, distribution at a vertical plane, y = 72.5 m, for eight different locations at a) $x/w = 20$, b) $x/w = 25$, c) $x/w = 28.6$, d) $x/w = 30$, e) $x/w = 31.8$, f) $x/w = 35$, g) $x/w = 40$, and h) $x/w = 45$ (respectively L_{z_1} to L_{z_8} shown in Figure 4.7). Results are shown for buildings on the beach surface and buildings on poles. The yellow and red hatched areas show the extension of the top and bottom of the buildings placed on the beach surface and on poles, respectively. The vertical black dashed lines show the zero-wind velocity. It is noteworthy that the velocity exactly at the bottom boundary is zero due to the no-slip boundary condition. However, the data points in this figure show the cell center values. This explains why the zero velocity at the bed is not included in this figure.

The comparisons between velocity patterns around buildings on the beach surface (Figure 4.7a) and buildings on poles (Figure 4.7b) clearly indicate an increased wind velocity underneath the buildings placed on poles. In addition, larger areas of low wind velocity both upstream and downstream of the buildings form for buildings with poles compared to those without poles. The vertical profile of the approaching wind velocity sufficiently upstream of the buildings follows the logarithmic law (Figures 4.8a and b). However, for $x/w = 25$ (L_{z_2}), the velocity slightly decreases and buildings on poles show somewhat higher attenuation rate. As the flow gets closer to the buildings, the more complicated the patterns of the velocity field become. A further decrease in the wind velocity at the lower part of the domain and the slightly negative velocity close to the bed and immediately in front of the buildings on the beach surface, $x/w = 28.6$ (L_{z_3}), clearly shows the existence of the circulation region (see the blue crosses in Figure 4.8c). This is due to the downward flow that moves from the stagnation point at the upwind face of the buildings and continue in the reverse direction relative to the incident wind. Just upwind of the buildings on poles, $x/w = 28.6$ (L_{z_3}), the wind velocity significantly decreases in front of the body of the buildings, though a gentle decrease occurs close to the bed and in front of the gap between upwind poles (see the green crosses in Figure 4.8c). A thin layer with low wind velocities is observed over the top side of both the buildings on the bed surface and the buildings on poles (Figure 4.8d). This can be explained by the flow separation that occurs when the wind encounters the upwind edge of the buildings. The flow velocity in this thin layer gradually increases with increasing height above the top face of the buildings. Underneath the buildings on poles, the flow is highly accelerated due to the funneling effect. It is noteworthy that, unlike the closed-channel flows, the maximum velocity does not occur halfway between bed surface and floor of the building. The reason is that the flow has to make a turn when passing the sharp lower edge of the buildings. Therefore, due to separation and the downward push of the horizontal momentum the point with the maximum velocity is deflected downward.

A small distance downwind of the buildings without poles (1.5 m behind the buildings), $x/w = 31.8$ (L_{z_5}), the results show a larger circulation region with negative velocities compared to upwind of the buildings, $x/w = 28.6$ (L_{z_3}) (see the blue crosses in Figure 4.8e). For buildings on poles, the near-bed velocity remains high, while the flow deceleration and slightly reversed flow occurs behind the body of the building (see the green crosses in Figure 4.8e). The farther away from the buildings, the less impacts the buildings have on the flow. The velocity of the decelerated flow behind the building's body, both without and with poles, increases while downstream of the poles the near-bed flow acceleration decreases (Figures 4.8f, g and h).

4.3.3. SEDIMENT TRANSPORT USING THE BAGNOLD FORMULATION

THE spatial variability of bed shear stress, $|\overrightarrow{\tau}|$ [N/m^2], around a row of buildings without and with poles is shown in 4.9. The bed shear stress results were entered in the Bagnold transport equation leading to sediment transport rates. The duneward component (x direction) of the transport, q_x [kg/m/s], is presented in Figure 4.10.

Model results indicate a substantial variation in bed shear stress around the buildings due to the poles. The row of closely spaced beach buildings placed directly on the bed effectively form a very wide building against the incident wind. Hence, the buildings largely block the flow and a connected area with low bed shear stress values develops just in front of the upwind face of the buildings (Figure 4.9a). Although a larger area with reduced bed shear stress forms upwind of the buildings with poles, our findings show slightly higher values due to flow ability to pass underneath the buildings (Figure 4.9b). For buildings placed on poles, high bed shear stress not only develops in the gaps between neighbouring buildings (similar to buildings without poles), but also underneath the buildings and just behind the buildings. This is caused by the flow compression and acceleration underneath the buildings, especially when passing the gap between the poles. Furthermore, the increased bed shear stress through the gaps between elevated buildings remains present far longer downstream compared to buildings placed directly on the bed surface. The small bed shear stress magnitudes in the shadow zone just behind the buildings on the beach surface are pushed downstream for buildings placed on poles.

The sediment transport rate derived from the bed shear stress show highly increased sediment transport rate in x direction through the gaps, below and behind the buildings on poles. While the transport rate in x direction just behind the buildings without poles is almost zero and somewhat negative (Figure 4.10a), the highest transport rates occur immediately downstream of the buildings on poles (Figure 4.10b). In addition, the increased sediment transport rates downstream of the gaps between elevated buildings take place over a longer distance in x direction compared to buildings without poles. Hence, placing buildings on poles could cause a larger amount of sediment to reach the dune foot.

4.3.3.1. INFLUENCE OF DIFFERENT POLE HEIGHTS

IN the present study, we are interested in understanding the impact of building poles height on the sediment delivery from the beach to the dune area behind the row of buildings. Until now, we have shown the comparisons between buildings without poles, $p_h/w = 0$, and with poles, $p_h/w = 1$, for flow patterns, wind-induced bed shear stress and sediment transport rate in x direction, which we call the duneward transport. For this purpose, we define six lines that are parallel to y direction and located at different positions in x direction downstream of the row of buildings (see L_{y_1} to L_{y_6} in Figure 4.11). The average

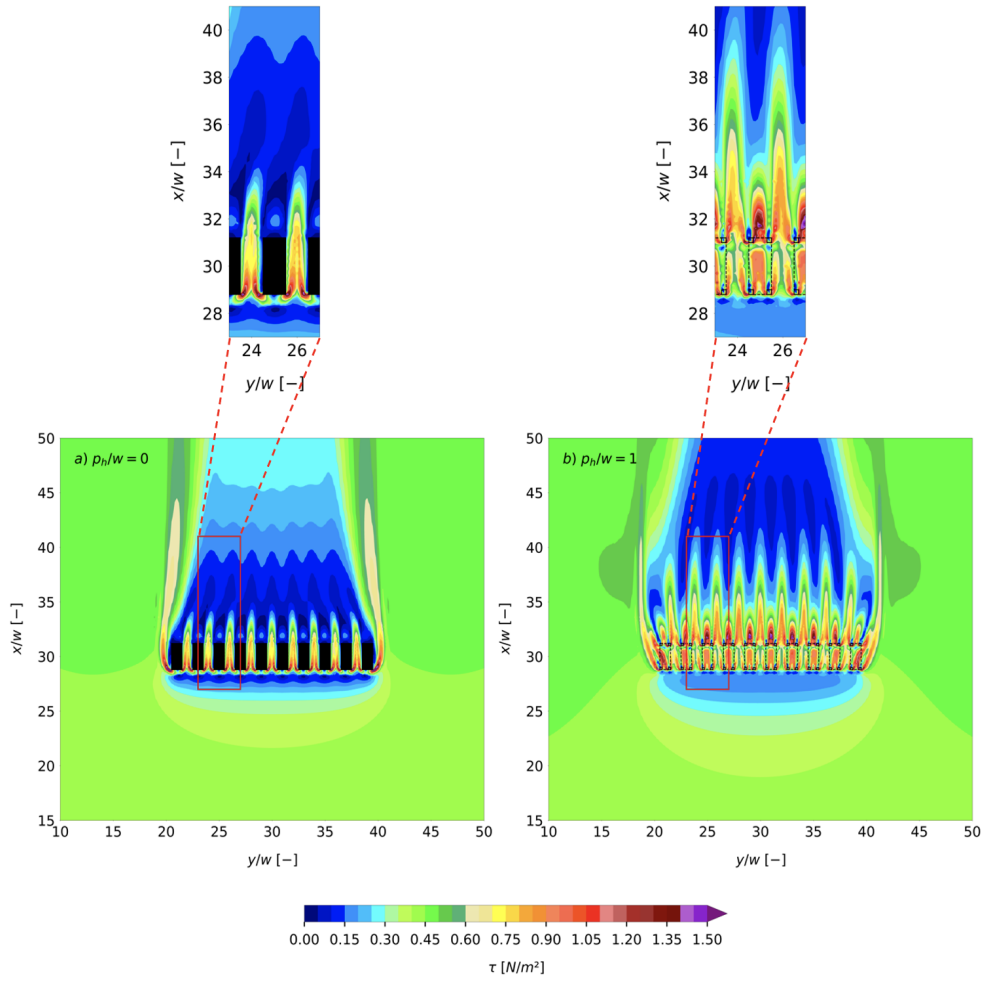

Figure 4.9: Distribution of bed shear stress, $|\vec{\tau}|$ [N/m^2], around a) buildings on the beach surface, $p_h/w = 0$, and b) buildings on poles, $p_h/w = 1$.

sediment transport flux in x direction, q_x, passing each line is then computed for buildings with different pole heights, and the results are compared in Figure 4.12. It should be noted that the results are presented as the net impact of buildings (with or without poles) on duneward sediment transport. Therefore, the average sediment transport flux over the lines at the same locations in an empty domain is computed, $q_{x_{ref}}$, and subtracted from the corresponding transport flux in the presence of buildings, $q_x - q_{x_{ref}}$.

Immediately behind the lee face of buildings, $x/w = 31.2$, all tested pole heights, ranging $p_h/w = 0 - 2.5$, cause positive impacts on the duneward (x direction) sediment transport flux. In other words, more sediment particles reach line L_{y_1}, when buildings with poles are

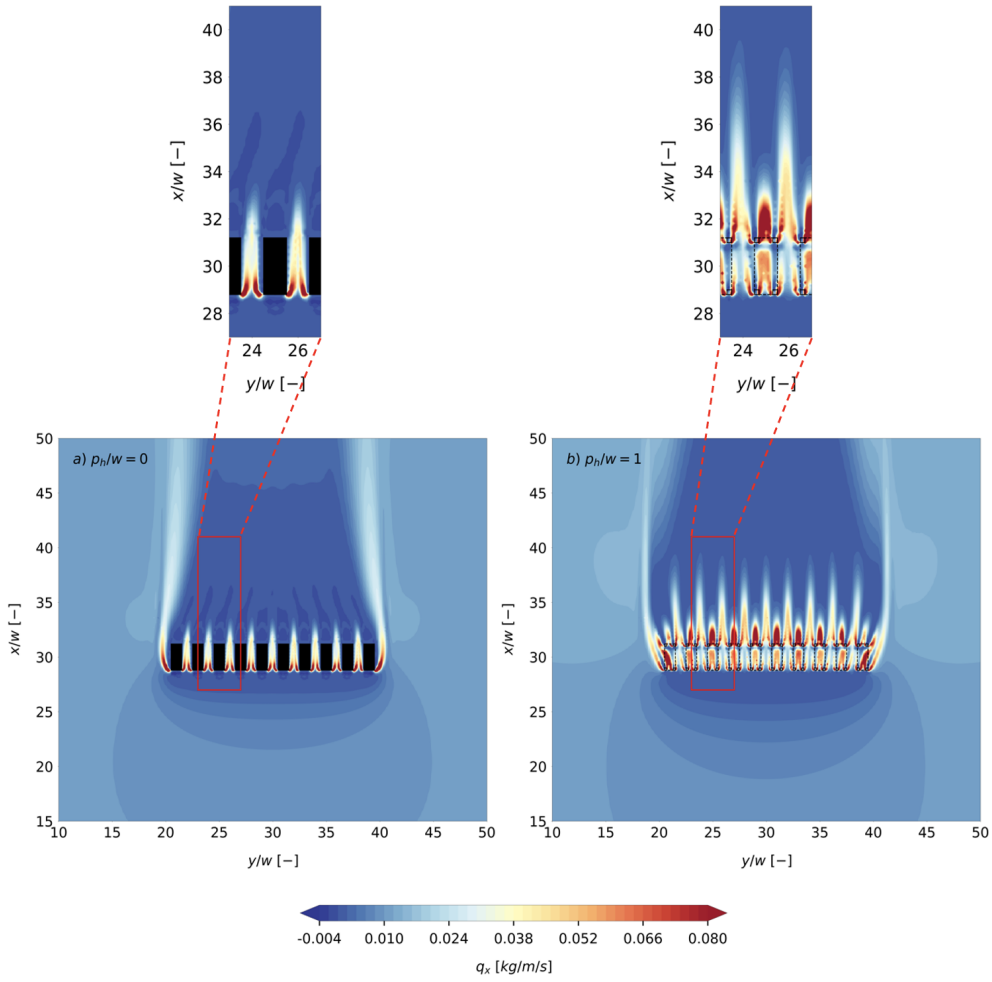

Figure 4.10: Distribution of sediment transport rate in x direction, q_x [kg/m/s], around a) buildings on the beach surface, $p_h/w = 0$, and b) buildings on poles, $p_h/w = 1$, using an aeolian sediment transport model proposed by Bagnold (1937).

placed in an empty model domain. Buildings with shorter poles, $p_h/w \leq 0.3$, have very small positive effect on the duneward transport, while the net effect of buildings considerably increases for higher pole heights, $0.4 \leq p_h/w \leq 1$. Results show that the buildings-related duneward flux reaching L_{y_1} for $p_h/w = 1$ is about eight times higher compared to when buildings with $p_h/w = 0.3$ are placed in the domain. There is a slight decrease in the effective transport flux, $q_x - q_{x_{ref}}$, for $p_h/w = 1.1$ and $p_h/w = 1.2$, for higher pole heights, $p_h/w \geq 1.3$, the transport flux increases mildly with pole height. Five meters downstream of the buildings' lee face, $x/w = 33.2$, buildings with pole heights $p_h/w \leq 0.5$ reveal neg-

ative impacts on duneward transport. This can be explained by the reverse flow and/or low-speed flow region where sediment particles move in the opposite direction compared to the incident wind (i.e. seaward) and/or the wind speed is not sufficient to initiate movement of the sediment particles. In addition, model results show stronger increase of sediment flux at L_{y_2} with increasing pole height when $0.6 \leq p_h/w \leq 1.3$, compared to higher poles. Further downstream, $x/w = 35.2 - 47.2$, results show an increase in the range of pole heights that leads to negative effective duneward transport,that is, less duneward transport compared to an undisturbed situation. This is apparently because the increased duneward sediment fluxes remain present far longer for taller poles (see Figure 4.10). The opposite pattern occurs downwind of L_{y_3}, $x/w \geq 35.2$, and for smaller pole heights, in such a way that the effective duneward sediment transport flux increases with increasing the distance from buildings. This occurs because the area with lowest bed shear stresses, dark-blue colors in Figure 4.9, is pushed further downstream by the high-speed jet flows through the gaps and below the buildings with higher poles. Conversely, the lowest bed shear stresses occur close to the buildings on shorter poles, and the flow is being recovered far downstream.

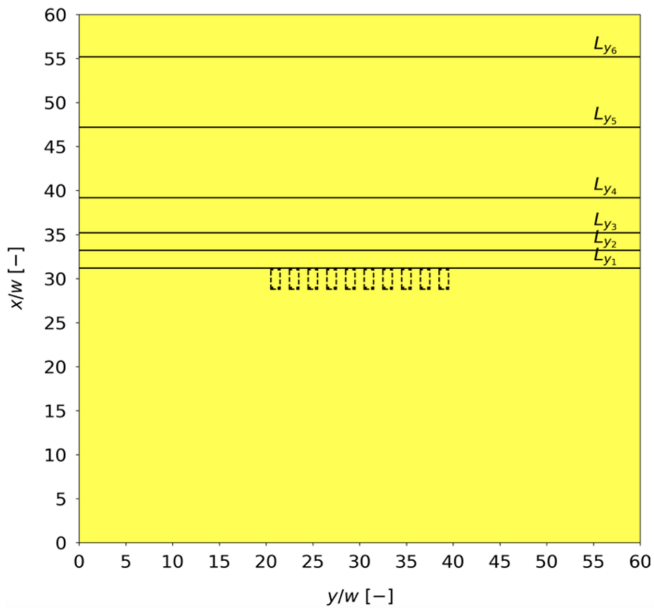

Figure 4.11: The positions of the lines in the y direction where the average sediment transport flux will be computed and analyzed in detail later in the paper are denoted by L_{y_1} to L_{y_6}. L_{y_1} is at $x/w = 31.2$, L_{y_2} is at $x/w = 33.2$, L_{y_3} is at $x/w = 35.2$, L_{y_4} is at $x/w = 39.2$, L_{y_5} is at $x/w = 47.2$, and L_{y_6} is at $x/w = 55.2$. Hence, lines L_{y_1} to L_{y_6} are positioned at 0, 5, 10, 20, 40, and 60 m downwind of the buildings, respectively, with a building width of $w = 2.5$ m and the downwind face of the buildings located at $x = 78$ m.

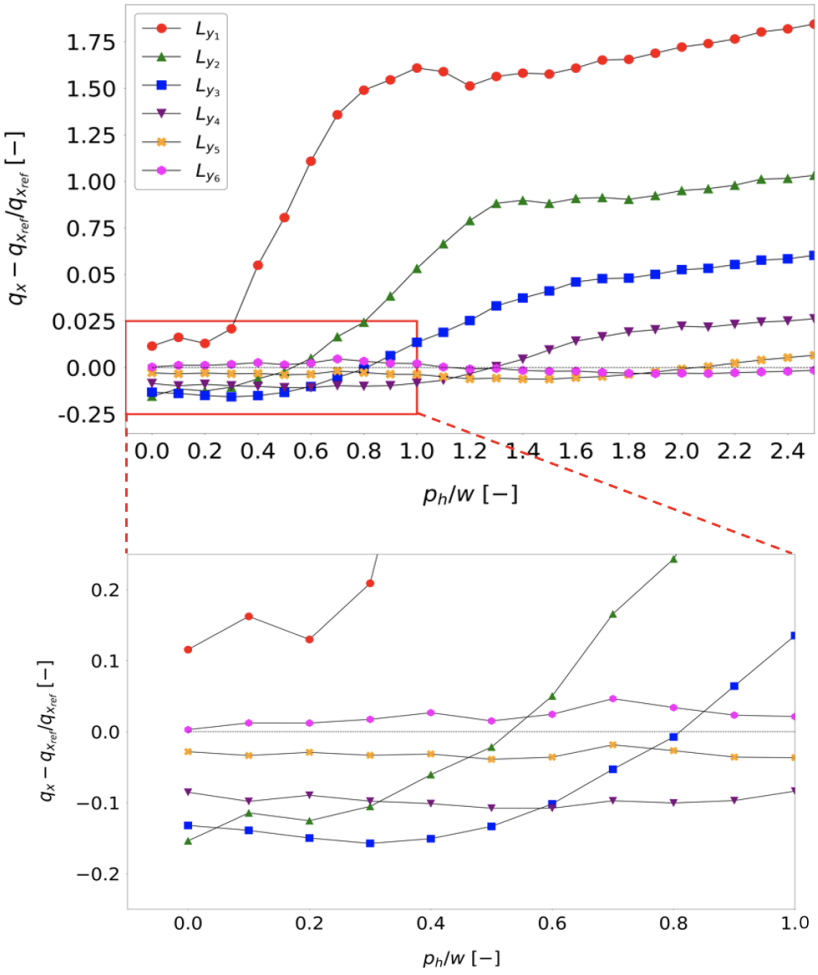

Figure 4.12: Net impact of buildings with different pole heights, p_h, on sediment transport flux in x direction (duneward), $q_x - q_{x_{ref}}$, passing lines L_{y_1} to L_{y_6} shown in Figure 4.11.

4.3.4. INITIAL BED LEVEL CHANGES USING EXNER EQUATION

THE initial erosion and deposition patterns, $\partial z_b/\partial t$ [m/s], that develop around a row of buildings without and with poles, using Bagnold and the Exner equation presented in Eq. 4.2 is shown in 4.13. To test the model validity, the field measurements of bed level changes around isolated scale models with different pole heights performed by Poppema et al. (2022b) are qualitatively compared with the numerical model results. The experiments took place at the Sand Motor beach in the Netherlands, and the scale models were present at the beach for a few days. Figure 4.14 shows the elevation maps relative to a fitted linear surface for individual sub plots to highlight the bedform changes due to the presence of

buildings.

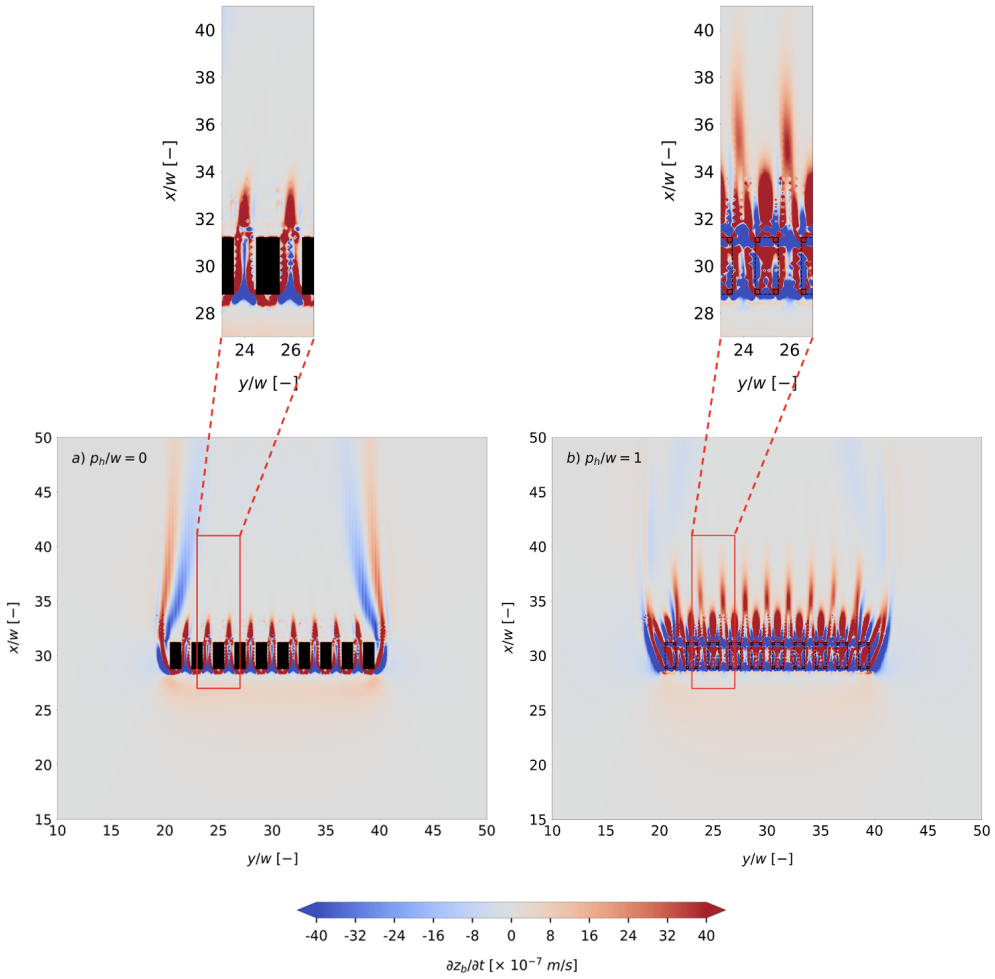

Figure 4.13: Initial erosion and deposition rate patterns, $\partial z_b/\partial t$ [m/s], around a) buildings on the beach surface, $p_h/w = 0$, and b) buildings on poles, $p_h/w = 1$, based on numerical model results using Exner equation (Eq. 4.2).

The numerical results show slightly lower deposition rates upstream of the elevated buildings. However, the upwind deposition spreads out over a larger area compared to when buildings are placed at the bed surface (Figure 4.13). In addition, the strong erosion and deposition areas that develop along and downstream of the two external buildings in the row of buildings without poles become smaller in height for buildings with poles. Considering that we only have field measurements of the bed level changes around isolated scale models at the beach (not a row of buildings), the observations show the similar patterns (compare Figure 4.14a with Figures 4.14b-f). Furthermore, deposition regions form around buildings

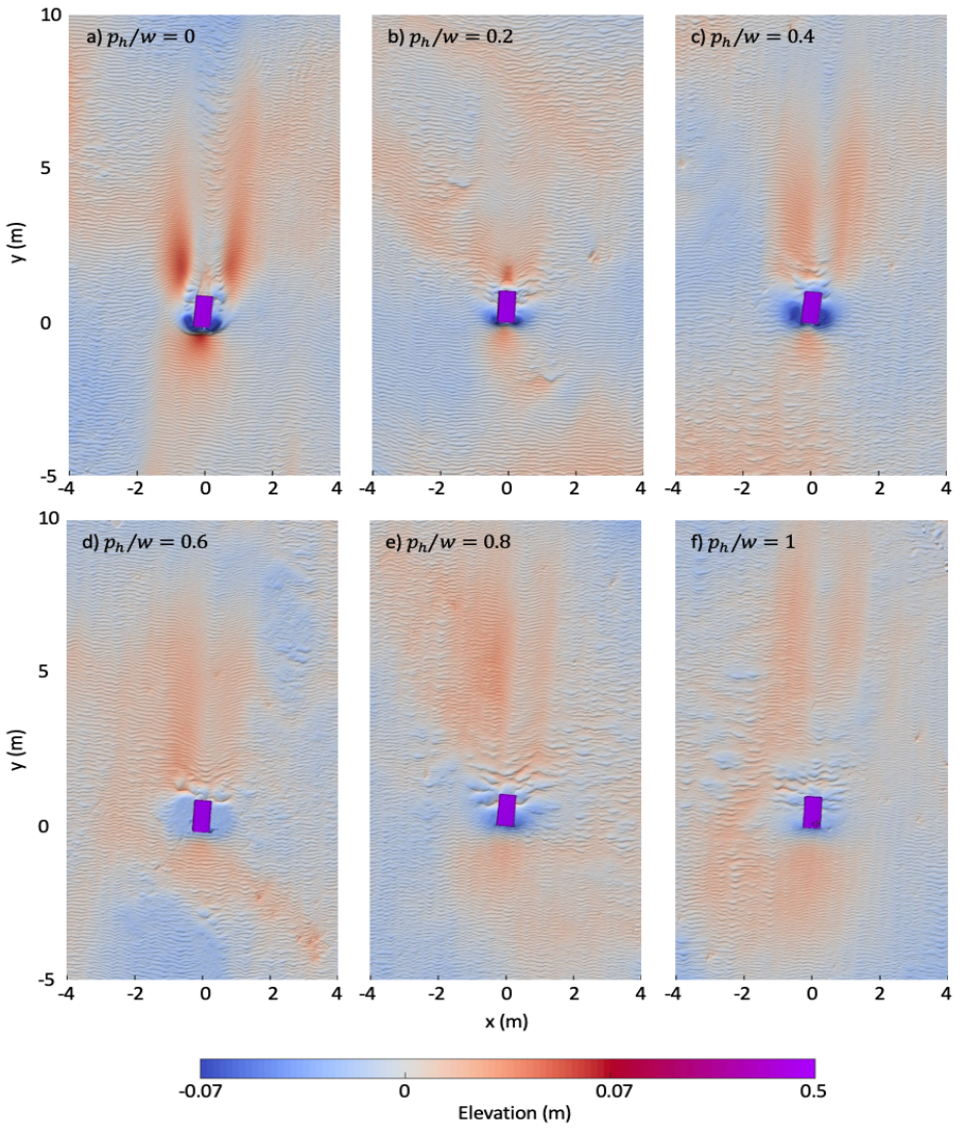

Figure 4.14: Measured morphologic patterns around isolated scale models of beach buildings on different pole heights, consisting a) $p_h/w = 0$, b) $p_h/w = 0.2$, c) $p_h/w = 0.4$, d) $p_h/w = 0.6$, e) $p_h/w = 0.8$ and f) $p_h/w = 1$. The scale models with length, width, and height of $1 \times 0.5 \times 0.5$ m were placed for a few days at the Sand Motor beach, the Netherlands. The dominant wind direction is perpendicular to the windward face of buildings and from bottom to up. The experiments were performed by Poppema et al. (2022b).

and extend further downstream, following the shape of the horse-shoe vortex (Blocken et al., 2011; Oke et al., 2017). The downwind deposition tails for two neighbouring buildings without poles, connect just behind the gaps and next to the buildings (Figure 4.13a). As

buildings are placed on poles, these deposition tails appear to extend over longer distances downwind the buildings and the connecting points move somewhat downstream in comparison with the buildings on the bed surface (Figure 4.13b). Similarly, the elevation maps show downwind deposition tails starting next to the scale models on the beach surface (Figure 4.14a), while they move somewhat downwind for buildings on poles (Figures 4.14b-f). Last, the numerical results show slightly shorter but stronger deposition tails just behind the elevated buildings compared to deposition tails behind the gaps (Figure 4.13b). This is comparable with experimental observations around some of the scale models (e.g. Figures 4.14b, c and e).

4.3.5. FURTHER DEVELOPED BED LEVEL CHANGES USING COUPLED MODEL

FIGURE 4.15 shows the bed level changes, z_b, around a row of buildings without and with poles, using the new coupled model. The bedforms are the result of an 80-hour simulation, while the wind shear is updated, using OpenFOAM, every 20 hours during the simulation time in AeoLiS. Results show that buildings placed directly on the beach surface form a large deposition area upwind of the buildings. Small depositions similar to echo dunes develop at small distance behind the gaps. For buildings placed on poles, less deposition develops in front of the buildings, while more sediments deposit both downstream of the buildings and the gaps between buildings. The well-pronounced downwind deposition tails behind the gaps between elevated buildings, red-shaded colors, are about 5 meters longer than those develop behind the gaps between buildings without poles.

To compare the bed topography estimated by the Exner formulation with those computed by the coupled model, the rate of changes in bed level around elevated buildings calculated by the Exner formulation is converted to the bed elevation developed within 80 hours of simulation (Figure 4.16). Results show that the upwind deposition is of about the same order of magnitude for both models. However, a notable difference exists in the bed level below and downwind of the buildings computed by the two models. The coupled model shows erosion below the buildings and immediately behind the buildings. However, the Exner equation mainly shows deposition in these regions. At some distance behind the buildings and the gaps between buildings, both models show depositions however, the deposition computed by the Exner equation is much higher than those simulated by the coupled model.

These differences can be explained by the methods that each model uses to calculate the sediment mass. In empirical formulations like Bagnold's transport equation, the sediment flux is only related to the wind velocity. The sediment transport flux derived from Bagnold's equation describes the equilibrium (saturated) sediment transport rate. In equilib-

rium condition, the actual sediment transport flux is equal to the sediment-carrying capacity of the air. Therefore, the equilibrium sediment transport flux is the maximum transport that occurs in case of fully-developed saltation, in which abundant sediment is available at the beach and the fetch distance is beyond the critical fetch (Nordstrom and Jackson, 1992; Nordstrom and Jackson, 1993; Van der Wal, 1998; Bauer and Davidson-Arnott, 2003; Delgado-Fernandez, 2010). The AeoLiS model uses an advection equation and sediment source and sink terms to model the sediment mass transport. In addition, AeoLiS accounts for the adaptation of flow velocity when local changes in spatial flow patterns occur. It also considers the avalanche processes that avoids large gradients near e.g. the piles, which typically is a non-linear process. Non-linear processes might decrease the growth in amplitude of the patterns, which is well-known in morphodynamic processes. This could be a reason that the coupled model shows wider and lower depositions, whereas the results derived by Exner equation show narrower and higher depositions.

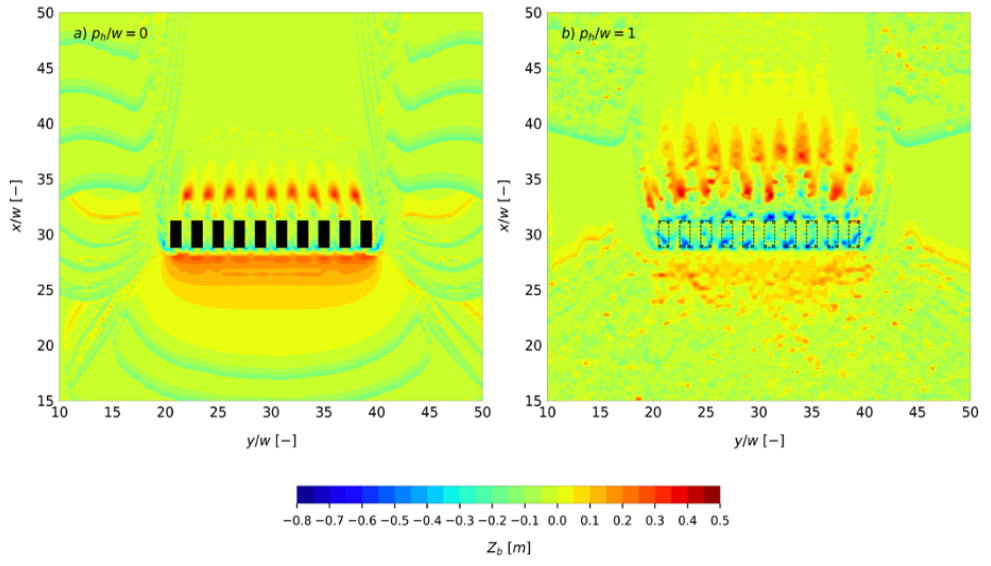

Figure 4.15: Bed elevation, z_b [m], around a) buildings on the beach surface, $p_h/w = 0$, and b) buildings on poles, $p_h/w = 1$, calculated within 80 hours of simulation in the coupled model.

4.4. DISCUSSION

Nordstrom and McCluskey (1984) pioneered in studying the morphological impacts of elevated buildings on dunes. Nordstrom and McCluskey (1985) studied the wind velocity underneath and around buildings with poles located at the Fire Island dunes in New York. Their flow measurements revealed that the mean wind speed considerably reduces in the

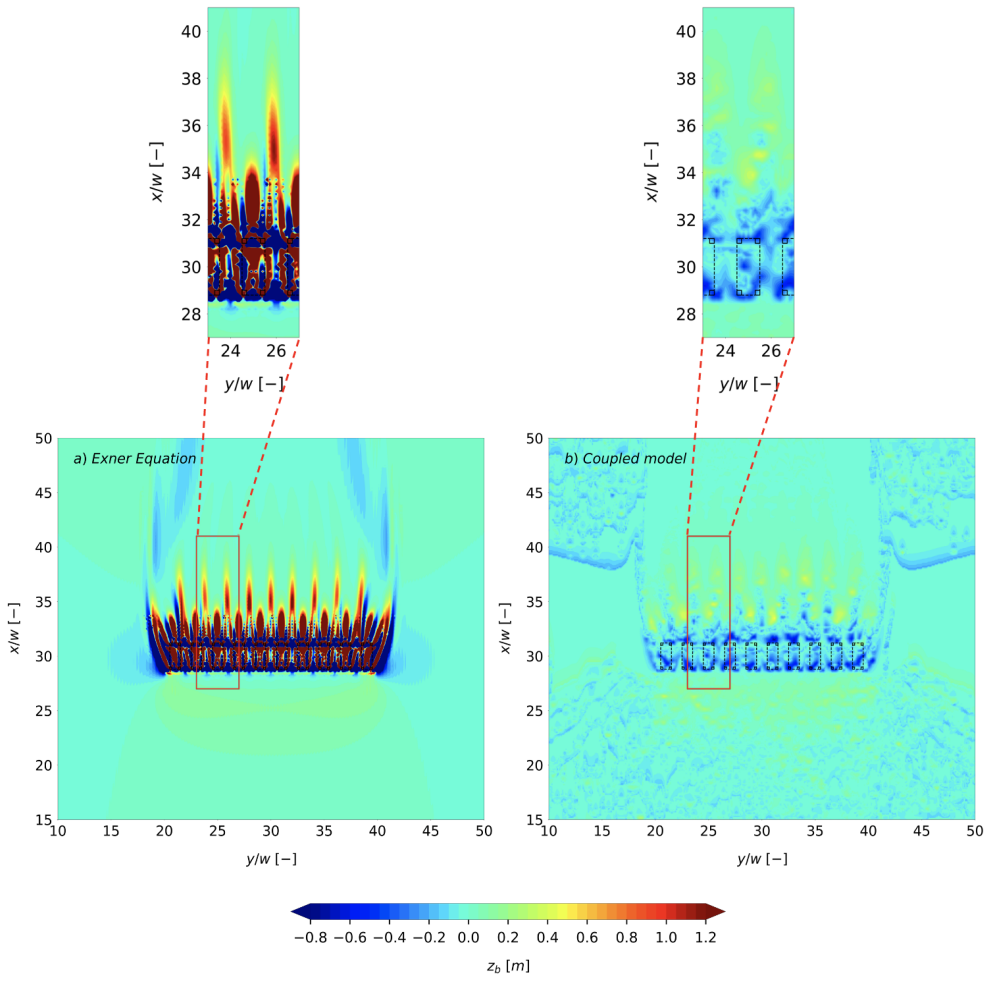

Figure 4.16: Bed elevation, z_b [m] around buildings on poles, $p_h/w = 1$, calculated within 80 hours of simulation using the a) Exner equation, and the b) coupled model.

lee of buildings, even though they are placed on poles. In contrast, the wind channelization below elevated buildings caused relatively high wind speeds that can be of the same order as the undisturbed wind speed far upstream of the buildings. These findings are in line with our model results. Figure 4.6a showed that the streamwise wind velocity downstream of the buildings with poles, $x/w = 42.85$, reaches approximately 0.24 the wind speed far upwind the buildings, $x/w = 15$. Conversely, the vertical profiles of the streamwise wind velocity at various locations in x direction, shown in Figure 4.8, revealed that the wind speed underneath the elevated buildings, $x/w = 30$ (Figure 4.8d), becomes even slightly higher than (1.06 – 1.16 times) the wind speed sufficiently upstream of the buildings, $x/w = 20$ (Figure

4.8a).

In this study, we assumed a steady wind condition, in which, the speed and direction of the dominant wind do not change over time. Conversely, beach buildings at the real beach are under unsteady wind gust conditions. The wind changes in speed, and it swings in different directions. Furthermore, the wind speed used in this study (u_{ref} = 17 m/s at the z_{ref} = 1.8 m) was sufficiently high to be considered as the storm wind speed in the Beaufort Scale. This implies that the bed shear stress, thus the sediment transport calculated in this study might over-estimate the actual sediment transport observed around buildings at the beach.

Aeolian sediment transport is substantially affected by a variety of supply-limiting factors such as bed moisture, vegetation cover, beach slope, particle properties, soluble salts, shells, and roughness elements (Pye and Tsoar, 2008; Nickling and Davidson-Arnott, 1990). These surface characteristics decrease the sediment carrying capacity of the air and/or the number of sediment particles that are available to join the saltation layer, causing reduced sediment transport rate. The impact of these supply-limiting factors on wind-blown sediment transport is typically incorporated by means of modifications in the threshold shear velocity, $u_{*_{th}}$ (Nickling and Ecclestone, 1981; Cornelis and Gabriels, 2003; J. King et al., 2005). This simplified approach complicates the sediment transport calculations using the aeolian transport models, specifically under real beach condition where the limitation in sediment budget exists. Consequently, the sediment transport models, e.g. the Bagnold's formulation used in this study, systematically overpredicts the transport fluxes (Sherman et al., 1998; Sherman and Li, 2012; Hoonhout and De Vries, 2019).

The AeoLiS model is able to take the impacts of both temporal and spatial variations of limiting factors in sediment availability into account. The model uses a simplified method to calculate the wind shear in the presence of smooth topographies. However, this method is no longer valid for buildings with vertical walls. The newly-developed coupled model benefits from both detailed wind-induced bed shear stress around buildings, computed by OpenFOAM, and the complicated sediment transport, using AeoLiS. However, deciding on the frequency of updating bed shear stress in Aeolis using the results from OpenFOAM, while running the transport model, AeoLiS, could be a challenging issue. Increasing the number of updates in wind shear increases the precision of the calculations but makes the simulations more computationally-expensive. In addition, small changes in bedform around buildings might not influence the near-bed wind field significantly. Therefore, further research is necessary to determine an optimal number of updates.

In this study, a constant wind speed and direction, i.e. a single extreme wind event was assumed. However, the coupled model could also be used to test morphological development for a longer time, including changes in wind speed and direction similar to the real

beach condition where the wind is constantly changing in speed and direction. Considering a constant wind direction, the sediments pile up in front of the building, sheltering the beach surface in the downstream area and close to the building against the wind. This reduces the actual influence of buildings, i.e. the impact of sharp edges, on their sandy surrounding. This means that the constant wind direction might create less erosion around the upwind face and corners of the building. This can be explained by the approaching wind that follows an aerodynamically smooth dune (the upwind sediment pile up) rather than a sharp-edged building.

Our model configurations relied on certain assumptions, particularly with regard to the geometric shapes and positions of the buildings at the beach. It is worth noting that any changes to these assumptions could potentially affect the patterns observed in this study. We discuss the implications of these assumptions and their potential influence on our results below, which may provide valuable insights for future research in this area.

Firstly, our study considered cubic buildings with flat roofs (Figure 4.1c), however beach buildings can come in various shapes, and roof designs such as pyramidal (Figure 4.1b), gabled (Figure 4.1d), wedged (Figure 4.1e) and others. Previous research by Enteria (2016), revealed that these different roofing designs can significantly affect the flow field velocity, pressure coefficients, and surface pressure coefficients of buildings. For example, Enteria (2016) found that flow separation occurs above the leading edge of building with flat roof, while for building with gabled roof, flow separation occurs at the roof's top (ridge). Moreover, the pressure coefficients behind building with flat roof were lower than those behind building with gabled roof. The observed variations in flow patterns can have significant impacts on bed shear stress and sediment transport. By focusing on buildings with flat roofs, our study provides a starting point for further investigation into the influence of different roofing designs on these processes.

Secondly, the numerical simulations in this study were performed using a constant gap (between neighbouring building) size of one time the width of a single building and under perpendicular wind condition. However, previous studies showed that the surface shear stress in the lee of buildings and gaps considerably depends on the gap size and the orientation of buildings at the beach (Luo et al., 2012; Luo et al., 2014; Luo et al., 2016; Poppema et al., 2022b; Pourteimouri et al., 2023). The streamlines downwind of the buildings without poles are deflected slightly inward (see Figure 4.5a). Depending on the gap size, the row of buildings close to each other might effectively function as a single wide building in front of the wind. Hence, the incident wind tends to create a large recirculation region encompassing the lee faces of all buildings. The larger the gap size, the more intense jet flows. Therefore, the two large opposing vortices cannot fully develop behind the buildings, and the

high-speed separated flows from the edges of the corner buildings only deflect the jet flows, especially the external ones, inward. We selected a gap size equal to one time the width of a single building based on research by Pourteimouri et al. (2023), which demonstrates reduced flow perturbations in the lee of buildings without poles when this gap size is used compared to when buildings are placed closer together. Moreover, this gap size ensures that neighboring buildings remain somewhat independent of each other, while still allowing for a degree of interaction between adjacent buildings.

Thirdly, we modelled buildings on poles with a constant top sectional area of 0.5×0.5 m in our simulations. The length and width of building poles could influence the airflow field underneath the buildings. This, in turn, affects the aeolian sediment transport beneath and downwind of the buildings. The flow speed-up increases as the gap between the inner edges of the poles becomes narrower. Besides, the separation bubbles form downwind of the wide poles that could potentially traps sediments. Therefore, the quantitative results presented in this study are only representative for the tested geometry, gap size and wind direction. For the future studies, the impact of changes in these three parameters can be systematically investigated further.

Up until now, the morphological changes due to elevated buildings at the beach, and the impact of various pole heights on sediment delivery to the dune systems have not been studied yet. In the present study, we did not explicitly model the dunes behind the buildings. Placing buildings in front of the sand dunes would change the flow structures developing in the lee of buildings (depending on several parameters such as the dune slope, height, shape, and the distance between the row of buildings and the dune foot) which in turn, alters the sediment transport.

With all this, our findings not only improve the knowledge on the impact of different pole heights on duneward sediment transport fluxes, but also takes a significant step forward aiding in coastal decision-making processes, by quantifying the results with a number of systematic simulations.

4.5. CONCLUSIONS

THIS research aimed to quantify the influence of elevated buildings at the beach on airflow structures, aeolian sediment transport patterns and the bed level changes around buildings. A row of ten full-scale beach buildings placed on a flat/smooth bed was modelled making use of the open-source CFD solver, OpenFOAM. The Exner equation together with the Bagnold's sediment transport rate formulation, and a newly developed coupled model were used to simulate the initial and further-developed morphologic patterns around build-

ings, respectively. The impact of systematic changes in pole height on the potential sediment supply to the dunes was then investigated. The pole height determines whether the air can flow through the gap underneath the buildings, thereby determining the amount of sediment that can be carried by the wind to downstream of the buildings. This sediment could be deposited on the dunes, leading to dune growth and an increase of flood safety.

Our findings showed that the elevated buildings influence the wind speed of a larger region upwind of the buildings compared to buildings without poles. However, the lowest wind speed that occurs in front of the buildings on poles is much higher than the wind speed immediately upwind of the buildings without poles. The jet flows are significantly accelerated, compared to the wind speed in front of the gaps, when they are funneled through the gaps between both the buildings without poles and the buildings on poles. The flow speed-up through the gaps is slightly higher for elevated buildings. The flow speed decreases as it expands downstream of the gaps. For elevated buildings, the high-speed airflow behind the gaps decelerates gradually over a long distance downstream of the buildings. However, the flow behind the gap decreases rapidly for buildings without poles. Then, the wind speed increases as the flow joins the undisturbed flow in the wake region.

To gain insight in the effect of elevated buildings on duneward sediment transport, the effective average sediment transport rates across along-shore lines at different locations downstream of the row of buildings were calculated. Our research showed that buildings on poles could either enhance the sediment transport to the dunes or, alternatively, block the sediments upstream of the buildings and cause a decrease in the amount of sediment reaching the dunes. For buildings with pole height to width ratios of $p_h/w \leq 0.3$, the sediment flux just behind the buildings showed a small increase in comparison to the sediment flux in an undisturbed situation. The sediment transport significantly increases for higher poles, $0.3 < p_h/w \leq 1.0$, whereas for pole height ratios greater than 1.0, the sediment transport increases mildly with pole height. The effective sediment flux across a virtual line five meters downwind of the buildings showed a reduction in duneward sediment transport for $p_h/w \leq 0.5$. For higher pole height ratios up to 1.3, a rapid increase of sediment transport with increasing pole height was observed whereas for higher poles a further increase in pole height had only a small effect on further increasing sediment transport. Our findings showed that the effective sediment flux decreases up to 10 meters downwind of the buildings. However, this is not always valid for further distances away from the buildings, especially for buildings with shorter poles that showed an opposite pattern. This can be explained by the airflow behavior downstream of the buildings. The region with reduced bed shear stress forms immediately behind the buildings without poles or buildings on short poles. The flow is then recovered as it joins the undisturbed flow far downstream of the buildings. For buildings on higher poles, the region with reduced bed shear stress is

pushed further downstream. Therefore, the effective sediment flux for higher pole heights decreases very far away from the buildings.

The findings of this study could help coastal managers to choose an appropriate pole height when they set regulations for designing buildings at the beach to either get most benefits from beach buildings in regards to the sediment transport to dunes, or minimize their potential negative impacts on dunes.

5

Discussion

THIS thesis focused on understanding of the influence of buildings at the beach-dune interface on the wind field, sediment transport and bedform patterns in their surroundings. In Chapters 2-4, we studied how airflow and sediment transport patterns in the vicinity of buildings depend on building characteristics (dimensions and pole height), positioning with respect to the neighbouring buildings, and the orientation relative to wind direction at the beach. In this chapter, the results are further discussed, comparisons with literature are made, and the applications and limitations of this study are explicitly elaborated.

5.1. FLOW MECHANISMS RESPONSIBLE FOR AEOLIAN MORPHOLOGIC PATTERNS AROUND BUILDINGS

THE formation and evolution of wind-driven erosion and deposition patterns around beach buildings are determined by the secondary flow structures that develop due to the presence of buildings. The wind approaching a sharp-edged building is diverted into four branches; downward to the bed, sideward around the building and upward over the building (see Figure 1.3). The downward flow experiences flow reversal. The reversed flow together with the approaching wind form a standing vortex at some distance in front of the building. This vortex wraps around the upwind corners, stretches out around the lateral sides and further downstream of the building creating a horseshoe shape (Peterka et al., 1985; Blocken et al., 2011). The incoming wind and the reversed flow form a deposition region, similar to the shape of echo-dunes, at some distance upwind the building where the flow deceleration is pronounced. The reduced wind speed decreases the sand transport capacity of the wind, explaining the formation of upwind deposition. Apart from flow deceleration, the convergence of the third-order horizontal velocity field enhances the deposition in front of the building. This finding is consistent with the results reported in previous studies, where the echo-dunes form at a small distance in front of solid obstacles, i.e. buildings, hills, and cliffs, when the windward slope of the obstacle is steeper than $50° - 55°$ (Tsoar, 1983; Cooke et al., 1993; Qian et al., 2011). Therefore, the third-order convergence of the horizontal flow replicates the sediment transport convergence qualitatively well. The horse-shoe shape vortex causes high-speed regions at small distance away from the upwind corners and the lateral sides of the building, creating local eroded regions at those locations, especially around the leading corners (Iversen et al., 1991; Tominaga et al., 2018; Poppema, 2022). This can be also explained by the large negative convergence of the third-order horizontal velocity field. Deposition tails form around and/or downstream of the building as the accelerated flow slightly decelerated when joining the undisturbed flow far away from the building. Buildings create either one or two deposition tails, depending on the sediment supply, wind shear velocity, building shape and orientation (Cooke et al., 1993; McKenna

Neuman et al., 2013). There is a sheltered area immediately downwind the building, within which the wind-induced bed shear stress, thereby the sediment transport capacity of the wind is small. This causes sand accumulation just behind the building, also referred to as lee dune or sand shadow (Bagnold, 1941; Pye and Tsoar, 2008; Luo et al., 2012). The similar phenomenon occurs for river dunes or bedforms in shallow seas. The sand is trapped in the low-speed flow separation zone that forms behind the slip face of the dune. Conversely, the flow speed-up occurs over the stoss face of the dune. These together induce dune migration over longer time scales (Paarlberg et al., 2007; Lefebvre, 2019; Lokin et al., 2022).

In case of multiple buildings close to each other, the airflow patterns and thus the aeolian erosion and deposition patterns change. The gap size between neighbouring buildings plays an important role in the development of sand drifts in the lee of gaps (Cooke et al., 1993; Greeley and Iversen, 1985; Luo et al., 2014; Luo et al., 2016). The flow speed-up through the gap causes an elevated wind-induced bed shear stress, hence increases the sediment transport capacity of the wind. Conversely, the flow expansion beyond the gap causes flow deceleration, and as a result sand deposition occurs. Buildings placed very close to each other act similarly to an isolated very wide building against the wind regarding the flow patterns. They form a large continuous deposition region upwind of the row of buildings, and dominantly divert sand particles to the outer buildings in the row. For larger gap sizes, the flow intrudes through the gaps. The sediment transport increases as a result of funneling effect, creating larger sand drifts just behind the gaps while smaller deposition tails occur at external sides of the row. Our findings showed that there is a critical gap size, beyond which less flow intensification occurs through the gaps and morphologic patterns around each building in the row are similar to those patterns that form around an isolated building. Apart from the gap size, the wind direction relative to the buildings is of high importance affecting the aeolian sediment transport. The wind direction determines the orientation and size of the circulation regions forming in the vicinity of buildings. The development of large vortices in the gaps between buildings causes flow blockage for the approaching wind, thereby an intense funneling effect occurs through the gaps. This affects the significance of the sand drift behind the gaps.

It is noteworthy that we only tested one size for the buildings in the row. Our findings might change if different width-to-height ratios for buildings are applied. For example, our results in Chapter 2 showed that when the buildings get higher, the airflow passing around the lateral faces of the buildings accelerates and the separation bubble behind the buildings becomes larger. This flow speed-up around the buildings might increase the sediment-carrying capacity of the wind and steer more sediments to downstream.

5.2. COMPARISON BETWEEN THE DIFFERENT SEDIMENT TRANSPORT MODELS

SEDIMENT transport has been widely modelled using equations that relate the transport flux to the third power of the wind velocity (Bagnold, 1941; Kawamura, 1951; Lettau and Lettau, 1977). The sediment transport rates derived from these empirical formulations describe the equilibrium (saturated) sediment transport rate. The equilibrium sediment transport rate is the maximum transport rate occurring in case of fully developed saltation, in which the fetch distance is beyond the critical fetch ($F > F_c$) (Nordstrom and Jackson, 1992; Nordstrom and Jackson, 1993; Van der Wal, 1998; Bauer and Davidson-Arnott, 2003; Delgado-Fernandez, 2010). Under equilibrium transport theories, the actual sediment transport rate is equal to the sediment-carrying capacity of the wind. Therefore, there is a balance between the sediment deposition (inflow) and the entrainment (outflow) from the bed surface. In case of abundant sediment supply at the beach and fetch distances beyond the critical fetch, the equilibrium sediment transport rate can be considered as an appropriate indicator for the actual transport rate at the beach (Hoonhout and De Vries, 2016). However, the fetch distance on an actual beach is limited by the beach width, and the supply-limiting factors usually exist on beaches. Parameters affecting the availability of sediment on the beach consist of vegetation, surface moisture (Davidson-Arnott et al., 2005; Bauer et al., 2009; Nolet et al., 2014), beach slope (Hardisty and Whitehouse, 1988; De Vries et al., 2012), grain size and sorting (Horikawa et al., 1986), beach armouring (Hoonhout and De Vries, 2019), shells (McKenna Neuman et al., 2012), non-erodible roughness elements (Logie, 1982) and soluble salts (Nickling and Ecclestone, 1981). The factors noted above limit the entrainment of sediment particles from the beach surface.

The empirical formulations represent transport-limited situations, meaning that the bed surface supplies unlimited dry and uniform sediments under steady wind conditions over a flat bed. Hence, the actual sediment transport rates on natural sandy beaches are often much lower than those estimated by the empirical models, and consequently they cannot be considered as appropriate indicators for the measured sediment transport rates in the field (Sherman et al., 1998; Sherman and Li, 2012; Hoonhout and De Vries, 2019). The influence of supply-limiting conditions on the sediment available for aeolian transport at the beach is commonly incorporated using calibration coefficients for the wind velocity threshold (Nickling and Davidson-Arnott, 1990; Cornelis and Gabriels, 2003). This approximation method could be a limitation in empirical sediment transport models, especially when modelling the actual beach where inherent spatial and temporal variability in bed surface features exist.

To model sediment transport around buildings, the 3D airflow model developed using OpenFOAM was coupled with the process-based 2D sediment transport model, AeoLiS, in which the aeolian sediment transport rate, fetch distance, wind shear threshold for sand entrainment and sediment availability at the beach are incorporated. The AeoLiS model simulates the sediment availability for aeolian transport on sandy environments rather than parameterisation of the threshold velocity. It can also simulate arbitrary variations in bed surface features in either space or time that enables modelling more realistic cases, i.e. sandy beaches. Unlike the empirical formulations, in which the sediment transport is only related to the airflow velocity, AeoLiS takes the spatial effect of the adaptation to local changes in flow patterns, e.g. separation zones, into account. In this thesis, the coupled model was used to examine the finite amplitude evolution of bed level around buildings without and with poles placed on a flat sandy substrate, i.e. an open beach, within a couple of days. Although, AeoLiS is already capable of modelling several parameters such as surface moisture, vegetation, hydrodynamic, waves, tide, groundwater and none-erodible obstacles (Hoonhout and De Vries, 2016; Hoonhout and De Vries, 2019), the supply limitation capabilities of AeoLiS have not been considered in this study. We assumed a constant wind speed and direction, i.e. a single extreme wind event, in our simulations. However, using the coupled model, it is also possible to consider wind time series, in which the wind conditions are constantly changing similar to the situation at a real beach. The spatial distribution of bed shear stress surrounding the building changes substantially with the wind direction. Furthermore, considering a uni-directional wind, the sediments pile-up in front of the windward face of the building might create a hindrance for downstream, sheltering the beach surface close to the building against the wind. This reduces the influence of buildings on their sandy surroundings, creating for instance less intense eroded regions around the upwind face and corners of the building. In case the sediment deposition becomes truly high, the approaching wind might follow the flow mechanisms forming over and around an aerodynamically smooth dune rather than a sharp-edged building. It should be noted that although the coupled OpenFOAM-AeoLiS model is key to simulating real-world situations, it could become computationally expensive. The total frequency of coupling between OpenFOAM and AeoLiS depends on the time scale over which we are looking at wind-driven morphologic patterns, also the time interval in AeoLiS that the bed shear stress needs to be updated using OpenFOAM. The latter affects the accuracy of the model results.

5.3. MODEL LIMITATIONS

5.3.1. BEACH BUILDINGS IN FRONT OF DUNES

IN this thesis, we studied the impacts of buildings with various configurations on a flat/open

beach in their surroundings. However, on an actual beach, multiple rows of beach buildings are generally positioned in front of the dunes. To obtain insight into the influence of buildings on dunes, we examined the average sediment transport fluxes passing multiple lines in along-shore direction and at different locations downwind of the buildings. Our findings showed that the averages vary considerably depending on the location of the lines. Although these investigations enable comparisons between the potential duneward sediment transport for different building configurations at the beach, they cannot be considered as detailed projections of the sediment transport when buildings are placed in front of the dunes. The reason is that when buildings are placed in front of the dunes, more complicated airflow and thus sediment transport patterns form in the lee of the buildings. Figure 5.1 shows the wind speed and direction around a row of full-scale buildings in front of the dune. These patterns mainly depend on the distance between the buildings and the dune foot, dune slope and wind direction (Nordstrom et al., 2000; Smyth and Hesp, 2015; Hesp and Smyth, 2021). To make a fair interpretation of the impact of buildings on duneward sediment transport, the examination of the sediment transport towards the dunes without the presence of buildings is needed. In the absence of buildings, Jonkheer (2022) found that three flow regimes occur in front and over the dune, depending on the dune slope and wind direction. These flow regimes consisting the flow attached to the stoss slope of the dune, single circulation region in dune foot, and two circulation regions; one in dune foot and one over the top of the dune. Placing a row of buildings in front of the dunes will locally change the flow patterns mentioned above and the flow properties (speed and direction) depending on the distance between the buildings and the dune foot as well as building characteristics. This causes changes in the duneward sediment transport patterns and magnitude (Stevers, 2021; Hobeika, 2021).

5.3.2. BEACH HOUSES IN COMBINATION WITH LARGE BUILDINGS

IN this study, we modelled a row of beach buildings with the same size and geometry placed on a flat bed. In a real beach, the row of beach houses are sometimes placed in combination with large buildings, e.g. restaurants, hotels and pavilions. Depending on the size of these pavilions and beach houses, gap size between them and the orientation of these buildings relative to the wind direction, the airflow patterns around buildings change which, in turn, alter the aeolian sediment transport and potential morphologic patterns around buildings. Figure 5.2 shows the flow field (speed and direction) around a row of buildings in front of the dune. Large buildings can give more significant interactions between buildings and dunes.

As indicated in Figure 5.2, the separation bubble consisting of two large counter-rotating

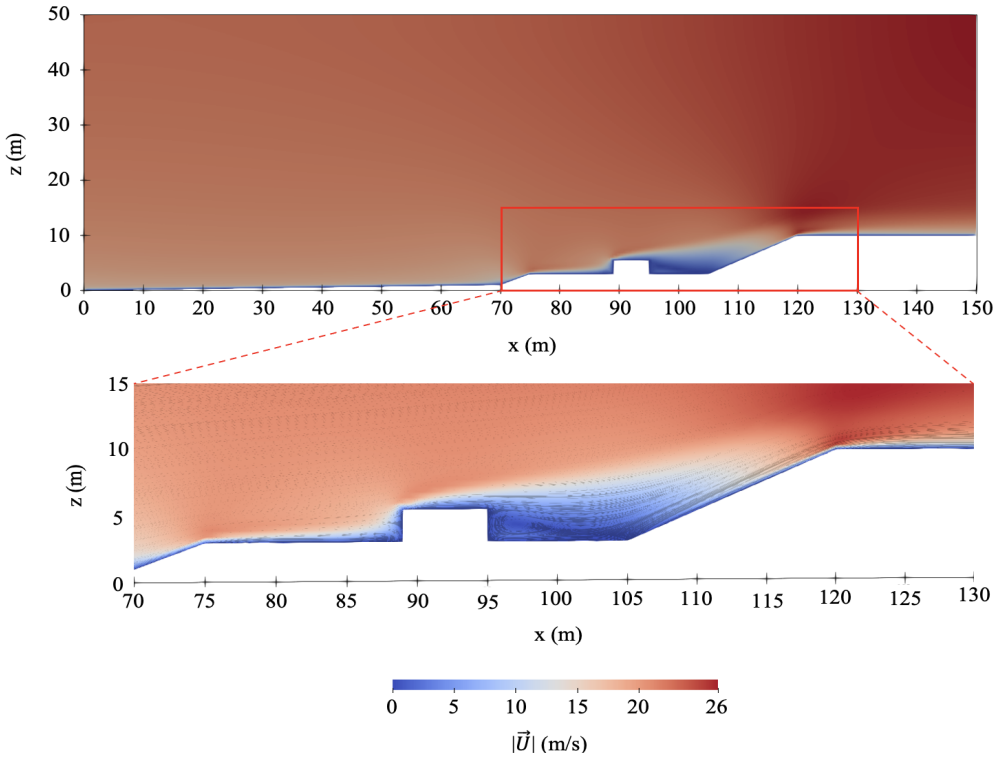

Figure 5.1: Wind velocity magnitude and flow direction around a row of ten full-scale beach buildings with the length, width and height of 6.0 × 2.5 × 2.5 m, placed in front of a dune. The gap spacing between neighbouring buildings is equal to the width of each building. The dune height is 10 m, and buildings are placed on the beach which is at an elevation of 3 m from the zero level. The wind speed is 17 m/s at 1.8 m, and wind direction is perpendicular to the upwind face of the buildings (left to right). Results are derived for a vertical plane passing the center of the one of the two central buildings.

vortices forms downwind of the large building that there is no beach houses in its downwind. Conversely, the large building with beach houses in its downwind shows disturbed airflow patterns in the separation bubble, meaning that the flow patterns in the vicinity of the large building and adjacent beach houses interact. The number of beach houses that are located in the shadow of the large building depends on a number of parameters (e.g. gap width, wind direction) that have not been studied in this thesis.

5.3.3. CROSS-SECTIONAL AREA OF THE POLES OF ELEVATED BUILDINGS

CHAPTER 4 of this thesis studied the influence of pole height on the airflow patterns and aeolian bedform development around a row of buildings. A constant cross-sectional area of 0.5 × 0.5 m was used for poles in all tested simulations with elevated buildings. How-

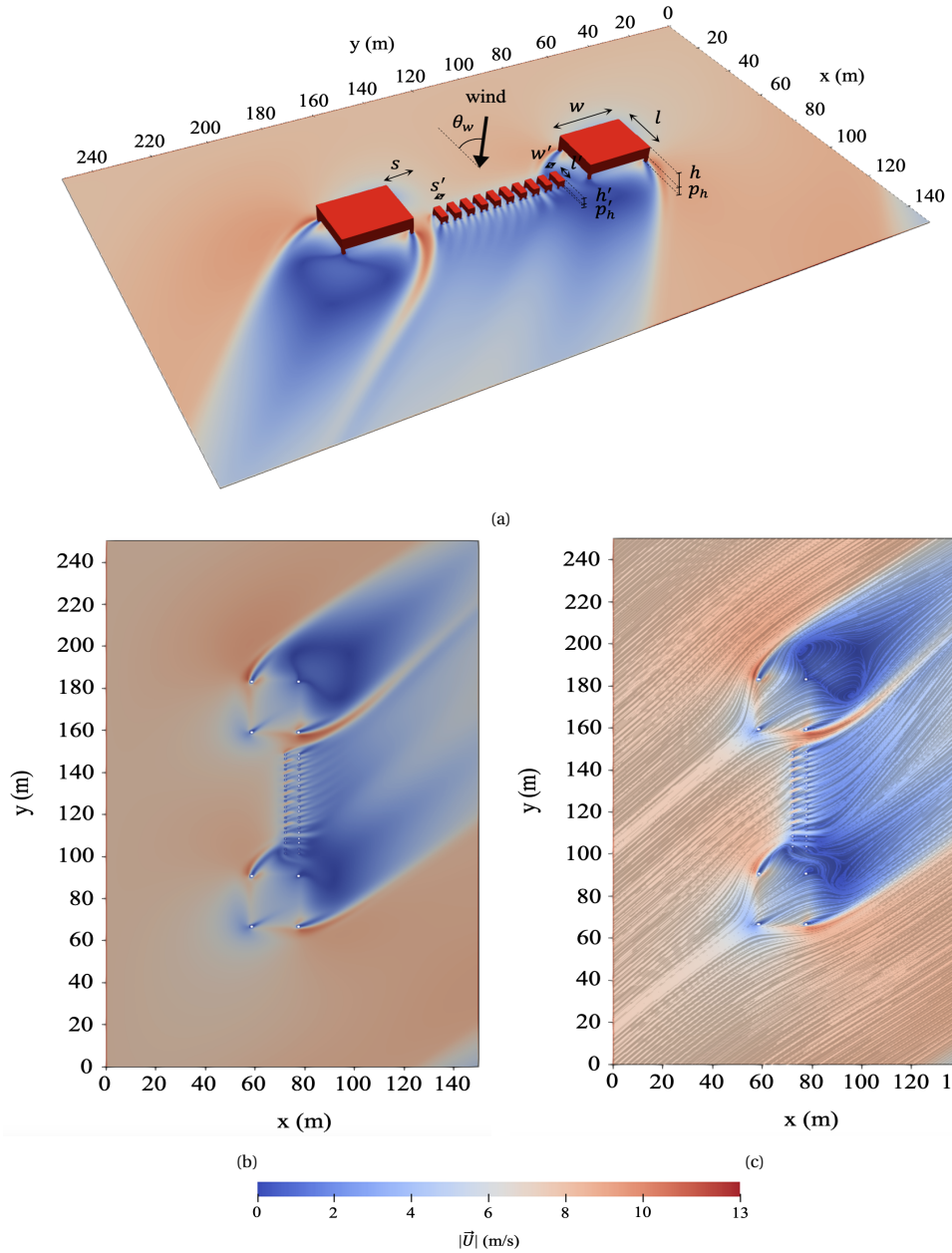

Figure 5.2: The flow field around a row of beach houses with the length (l'), width (w') and height (h') of 6×2.5×2.5 m that are placed in between two large buildings with the length (l), width (w) and height (h) of 20 × 25 × 5 m. The beach houses are placed on poles with the height of ${p_h}' = 1.25$ m. The large buildings are placed on poles with the height of $p_h = 2.5$ m. The top section of the poles in the beach houses is 0.5 × 0.5 m, whereas it is 1.0 × 1.0 m for the large buildings. The gap width between the large buildings and the first/last building in the row (s), and the gap width between the two neighbouring beach houses (s') are 10 m and 2.5 m, respectively. Figures a and b show the downwind view and bottom-view of the wind speed magnitude around buildings, and Figure c shows the flow direction. The Figures are plotted for a horizontal plane at an elevation of $z = 0.25$ m from the bed surface. The incident wind is $u_{ref} = 17$ m/s at $z_{ref} = 1.8$ m, and the wind direction is $\theta_w = 45°$ relative to the x direction of the domain.

ever, the length and width of the poles will vary in reality, depending on the size of the building, and could affect the flow behaviour underneath the buildings which, in turn, influences the wind-blown sediment transport. For instance, the narrower the gap between the inner edges of the poles, the more intense funneling effect and acceleration in flow. Furthermore, the recirculation region that forms downwind of the wide pole could potentially traps sand grains.

5.3.4. ANTHROPOGENIC INTERVENTIONS

SANDY beaches attract a large number of people, especially during the touristic season. Human interventions alter the aeolian sediment transport at the beach and thereby also the morphologic patterns around buildings and the dune topography (Nordstrom, 1994; Nordstrom et al., 2000; Jackson and Nordstrom, 2011; Martínez et al., 2013). Human activities affecting the natural aeolian processes at the beach consist of walking/driving on building-induced bedforms, trampling/removing vegetation, beach cleaning operations and relocating sediments (Bochev-Van der Burgh et al., 2011).

The deposition tails forming downwind of the buildings close to the dunes could enhance the development of the dune ramps that are crucial to facilitate aeolian sediment transport onto the dune stoss slope and toward the crest (Walker et al., 2017) (Figure 5.1). Deposition close to the building might hinder the access walkway and the doors to the buildings. Hence, to prevent the inundation of buildings by sand, the property owners remove sand deposition just behind the buildings. This induces negative impact on the development of the dune ramp, hence retarding the dune growth. Furthermore, removing the sediments immediately behind the buildings creates a very steep slope that results in sand avalanche and impedes the dune growth.

Figure 5.3: A row of closely-spaced vacation houses with deposition regions behind their lee face. The buildings are placed at a close distance to the dunes (photo by Daan Poppema.)

To better understand and quantify the anthropogenic effects on aeolian morphologic development around buildings at the beach, the linking between the coupled model developed in this thesis and the models that represent the human dynamics at the beach is needed. This can be done by multi-level modelling that engages the scientific knowledge provided by this study with social, economic, and policy disciplines to capture the human actions across a range of time scales (Lazarus et al., 2016). In addition, the coupled model developed in this study helps to describe the physics in anthropogenic-based processes.

5.3.5. OTHER LIMITATIONS

IN this thesis, the influence of building characteristics, positioning relative to each other and the orientation with respect to the incident wind direction on airflow structures and aeolian morphologic patterns around buildings have been studied. In our simulations, the dunes were not modelled and building(s) placed on a flat open area. The influence of natural bedforms, e.g. ripples, on the flow field was not taken into account. The small roughness length z_0 used in this study results in a smooth bed surface, which its roughness is significantly smaller than that of for the sandy beach surface. Furthermore, the sediment supply and the impacts of supply-limiting conditions have not been included in the model.

Although these simplifications of reality were assumed in the presented model results, the most important processes of airflow and sediment transport are included such that the model is able to investigate their primary effects. The erosion and deposition patterns that the model describes seem to match reality to a satisfactory degree to have confidence in the model.

5.4. MODEL APPLICATIONS IN COASTAL MANAGEMENT

NUMERICAL models were developed to examine the building-induced effects on airflow and sediment transport patterns in their surroundings, when buildings properties and location at the beach relative to each other and the wind direction systematically change. Although we studied buildings on a flat/open sandy beach, at the actual beach the buildings are often placed in front of the dunes. To account for the influence of buildings on sand supply from the beach to dunes, we computed the net average sediment transport flux passing different lines downwind the buildings.

Coastal sand dunes provide natural flood defences by protecting inland from storm surges. They also provide crucial ecological values as they are habitat for diverse species. Despite the widespread believe that buildings at the beach-dune interface hinder the aeolian sedi-

ment transport to the dunes (e.g. Hallin et al., 2019), the findings of this thesis suggests that buildings, depending on their characteristics, positioning and orientation at the beach, are capable to enhance downwind sediment transport. Therefore, buildings at the beach do not always disconnect dunes from their sediment source, also they can be used to enhance duneward aeolian sediment transport. This is also compatible with the findings reported by Nordstrom et al. (2000).

For example, we found that a row of buildings with very small gap sizes in between, i.e. 0.1 times each building width, causes almost no sediment flux through the gaps. They form a large deposition upwind of the buildings and mainly send sediments to the outer buildings in the row. As the gap size increases, up to 1.0 times each building width, flow speed-up and thereby increased sediment flux occurs through the gaps. Conversely, less sediments move to the outer buildings in the row. For gap sizes greater than 2.0 times each building width, less intense funneling effect occurs through the gaps. In addition, the airflow and sediment transport patterns developing around each building are approximately similar to those patterns that develop around isolated buildings. Hence, the neighbouring buildings have minor effects on each other and the resulting pattern can be described as more individual patterns around buildings. The similar findings were reported based on the field measurements performed by Poppema et al. (2022b). The above noted findings are valid for perpendicular wind direction, and they might differ for oblique wind directions. For instance, results showed that wind direction of 20° causes the most sediment delivery to far downstream of the buildings for all tested gap sizes between 0.1 to 4.0 times each building width. The implementation of rules of thumb that we derived based on the tested wind directions in this study might become challenging for the real beach where the wind direction is constantly varying over time. To use our findings for a real case study, the wind characteristics recorded by the nearby meteorological stations can provide the dominant wind direction over the most common seasons that the vacation buildings are placed at the beach, e.g. spring and summer. To obtain more accurate results, the weighted average of the net average sediment transport fluxes passing a certain line can also be computed considering the frequency of each wind direction provided by the wind rose.

Our results, furthermore, showed that not all the elevated buildings on poles cause positive impacts on dunes compared to when the buildings are placed directly at the beach surface. For instance, the effect of elevated buildings with various pole heights on the net average sediment flux, reaching five metres downstream of the buildings showed negative influence on dunes when buildings are placed on pole height smaller than 0.5 times each building width. The sediment flux increases considerably for greater pole heights up to 1.3 times building width, and beyond which the rate of change in sediment flux decreases. Therefore, an optimum pole height could lead to a reasonable amount of sediment to the dunes, while

minimising the cost of constructing extra pole height and access stairs to the buildings.

As mentioned above, we systematically studied the influence of gap size and pole height as a multiple of the width of each building on airflow and sediment transport patterns. The reason is that our findings in chapter 2 showed that the flow mechanisms and aeolian erosion-deposition patterns around buildings mostly depend on the building width perpendicular to the wind rather than the other two dimensions. Therefore, to obtain the dimensionless parameters, all dimensions were divided by the building width.

The findings of this thesis provide coastal managers with insights on how buildings at the beach influence their sandy environment and dunes morphology. Considering the assumptions used in this study, we found that:

- The airflow patterns, hence the aeolian bedform developments around buildings mostly depend on the building's width perpendicular to the prevailing wind direction. These patterns are least dependent on the length of the building parallel to the wind direction.

- The gap spacing between neighbouring buildings determines the flow patterns, especially downwind of the building. For $g^* \leq 0.09$, the row of buildings close to each other effectively act as a very wide building against the wind. Hence, the flow passing through the gaps is negligible, and two large opposing vortices form behind the entire row of building.

- For $g^* = 0.41$, the size of two outer vortices slightly decreases, whereas the jet flows through the gaps become more pronounced. Hence, the smaller-sized vortices that form behind the gaps are encompassed with a pair of larger opposing vortices. The outer vortices are destroyed by the intense inner jets as the gap ratio increases to 0.47.

- There is a critical gap spacing of $g^* = 0.67$ beyond which the airflow structures and erosion-deposition patterns around buildings are almost independent from neighbouring buildings. Hence, the resulting patterns are a linear superposition of the individual patterns forming around each building.

- The buildings with pole heights of $p_h/w \leq 0.3$ cause a very small increase in the net duneward sediment transport (compared to an empty domain) reaching the area just behind the lee face of the buildings. For higher pole heights, $0.3 < p_h/w \leq 1.0$, the net sand supply to the dunes significantly increases just behind the buildings.

- Five meters downwind of the buildings, the pole heights of $p_h/w \leq 0.5$ cause less duneward sediment transport compared to an empty domain. However, the higher

pole heights, $0.5 < p_h/w \leq 1.3$, result in a rapid increase of sediment transport with increasing pole height.

- The wind direction of $\theta_w = 20°$ causes a narrower and longer sediment transport downwind of the gaps between buildings. While the wind direction of $\theta_w = 40°$ results in a wider and shorter sediment transport behind the gaps.
- Far downstream of the buildings, the wind directions of $\theta_w = 20°$ and $\theta_w = 40°$, respectively, lead to the highest amount of net sand supply to the dunes for all gap ratios except for smaller ones ($g^* < 0.41$), where the net duneward transport for perpendicular wind direction, $\theta_w = 0°$, is higher than that of for $\theta_w = 40°$.
- The row of buildings creating an angle of $\theta_w = 80°$ with the incident wind direction, effectively acts as a very long building against the wind (wind is more perpendicular to the longer face of the buildings). Hence, the minimum duneward sediment transport is expected to occur similar to along-shore wind directions.

Using these rules of thumb, coastal managers could place buildings at the beach in a manner to either gain most benefits from buildings in regard to the sediment supply to dunes or minimise the negative impacts on their surrounding (i.e. sand accumulation locking the access door to the buildings or burying the boardwalks).

5.5. MODEL APPLICATIONS IN THE DEVELOPMENT OF SNOWDRIFTS AROUND BUILDINGS

THE building-induced aeolian bedforms found in this thesis are comparable with the snowdrifts that form around buildings (Thiis and Gjessing, 1999; Thiis, 2003; Beyers and Waechter, 2008; Tominaga, 2018; Liu et al., 2018). It has been confirmed that the main snowdrift patterns are erosion around the upwind corners of the building, and deposition in both upwind and downwind of the building (Tominaga, 2018).

The deposition of the snow particles mostly depends on two factors: it requires a low friction velocity and available snow particles for accumulation. However, the building-induced perturbations increase the snow concentration in the air which, in turn, results in snow accumulation at higher friction velocities than that of needed for snow deposition under undisturbed flow condition at an empty environment (without buildings) (Thiis, 2003).

A key difference between the aeolian sediment transport and snowdrift developments around buildings is that the sediment at the beach is not supplied from the falling process. Hence, the sediment transport around buildings at the beach only depends on the shear stress ex-

erted by the wind and the threshold shear velocity for sediment particle movement. In the case of snow blowing around the buildings, the snow particles are restrained from entering the sheltered area just behind the building. Hence, the snow accumulation just behind the lee face of the building depend on the vertical snow distribution in the upwind area, especially over the building's roof. The snow passing the top of the building can be trapped in the sheltered area. However, when the snow transport takes place only in saltation, the snow particles can only be entrained from the sides of the wake. The latter is more similar to the aeolian sediment transport that occurs at the beach.

Furthermore, an existing snowdrift around the building could change the roughness of the bed surface. The smoothening effect results in an increased wind-induced bed shear stress compared to a clean bed surface (Thiis, 2003). The increase in bed shear stress impedes the deposition of the snow particles.

5.6. MODEL APPLICATIONS IN ARID AND DESERT REGIONS

IN addition to coastal environments, the arid and desert regions (drylands) are potentially susceptible to aeolian sediment transport. The airflow and erosion-deposition patterns observed in drylands are similar to those patterns occurred in coastal zones. However, the wind-blown sediment transport in drylands could become more pronounced in comparison with coastal zones, because the dry sand is generally available in these areas and they are wide regions that can mostly provide the critical fetch distance. These areas are increasingly hosting anthropogenic activities such as transportation, industry, mining and housing. The hazards induced by aeolian sediment transport in drylands have been studied by Zhang et al. (2007), Salman et al. (2010), Liu et al. (2011), Middleton and Sternberg (2013) and Boulghobra (2016).

The wind-blown sediment transport in drylands acts at the scale of an isolated building (He et al., 2018), urban area (Mestoul et al., 2017) and at the infrastructures such as railways, roads, pipelines and irrigation canals (Bruno et al., 2018). The accumulated sand volume around civil structures and infrastructures in arid regions or deserts translates into both direct and indirect impacts. The direct impacts are static loads exerted on the structures, whereas the indirect impacts consist of undermined durability, functionality, human comfort and safety, as well as increased maintenance measures (Raffaele and Bruno, 2019).

The coupled model developed in this thesis can be used to gain insight on erosion and deposition patterns around buildings in arid regions or deserts. In addition, minor changes allow to use the model for simulating the aeolian morphologic patterns around infrastructures.

6

CONCLUSIONS AND RECOMMENDATIONS

THE goal of this thesis was to quantitatively study the influence of buildings at the beach on airflow structures, the aeolian sediment transport and how morphologic patterns form in their surrounding. In our study, we focused on understanding how building characteristics and positioning at the beach affect the bedforms in their vicinity. For this purpose, we developed a three-dimensional model using OpenFOAM that simulates the wind field around an isolated building or a row of buildings placed on an open beach. The bed shear stress derived from OpenFOAM model was used to model sediment transport and thereby wind-driven erosion and deposition patterns using two methods. Firstly, we developed a model to compute sediment transport fluxes using the Bagnold's (1941) formulation. Then, the Exner equation was applied to estimate initial bed level changes based on the convergence of the sediment transport fluxes. Secondly, we developed a new coupled model that allows to compute the evolution of morphologic patterns around buildings. This chapter answers the research questions formulated in Section **??**, using the studies that have been conducted in Chapters 2-4. Furthermore, the recommendations on future research possibilities are presented.

6

6.1. RESEARCH CONCLUSIONS

Q1 How do building dimensions (i.e. length, width, and height) influence the airflow and initial aeolian erosion-deposition patterns around an isolated building at the beach?

Our findings in Chapter 2 showed that the near-bed airflow patterns and the aeolian sediment transport both depend least on the length of the building parallel to the incident wind direction, while they depend most on the building width perpendicular to the wind direction and the building height. The length of the separation bubble just behind the building slightly decreases with increasing building length. The width of the building considerably influences the near-bed wind field in the vicinity of the building. The wider the building, the larger areas both upwind and downwind of the building were influenced due to the presence of the building. The height of the building also affects the near-bed wind field, but not as much as the building width. The taller building creates the longer pair of vortices, thereby also a larger separation bubble just behind the building.

The convergence of the third-order horizontal near-bed wind velocity field was used as a proxy for sediment transport. Results showed strong erosion around the windward corners of the building. The upwind deposition form at some distance in front of the windward face of the building. Furthermore, two downwind deposition tails develop around the building to somewhat downstream. We found that these deposition tails develop at a slightly slower rate for a longer building. As the building becomes wider, the upwind deposition increases in spatial extent and the downwind deposition tails slightly increase in length and width.

The growth rate of the upwind and downwind depositions slightly decreases with increasing building width. In addition, small deposition forms in the lee of the wide building. For taller buildings, the spatial size of the scour around the upwind corners increases. Furthermore, the taller the building, the slower deposition rate upwind of the building, while the downwind deposition increases.

Q2 How do wind direction and gap size between adjacent buildings affect the airflow, duneward sediment transport and the initial aeolian morphologic patterns around a row of buildings at the beach?

Chapter 3 showed that the gap ratio, g^* (the ratio of the gap width to the centre-to-centre distance between buildings), and the wind incidence angle, θ_w, are key factors determining the wind-driven bed shear stress and the sediment transport patterns around buildings. Buildings placed very close to each other, $g^* = 0.09$, effectively form a single wide building for the wind. The wind flows through the gaps are negligible thus no depositions form in the lee of the gaps. Instead, the buildings mainly block sediments at small distance upwind their windward faces or send sediments to the outer buildings in the row, creating two deposition tails around the entire row of the beach buildings. For larger gap sizes, up to $g^* = 0.50$, the airflow is accelerated through the gaps due to funneling effect, and it decelerates as expands downstream of the buildings. This induces formation of sand depositions in the lee of the gaps. For buildings placed further apart, $g^* \geq 0.67$, the funneling effect is less prominent and the airflow and sediment transport patterns are almost independent from neighboring buildings. Therefore, the sand depositions no longer develop behind the gaps, while deposition tails wrap around each building to somewhat downstream. Furthermore, upwind deposition peaks become separated in front of the buildings, and the outer deposition tails become shorter and almost the same size as the inner depositions.

The wind direction relative to the row of beach buildings determines the size and the location of the circulation regions in the vicinity of buildings. In case of vortices forming in the gap between buildings, the wind enters a narrow space through the gap as it is bounded by the outer edge of the vortices. Therefore, the funneling effect occurs creating sand depositions in the lee of the gaps.

Buildings at the beach could both limit or enhance the sediment transport to the dunes. It was found that, the average sediment transport flux reaching far downstream of the buildings is highest when $\theta_w = 20^\circ$.

Q3 What are the impacts of buildings pole height on airflow, duneward sediment transport and both the initial and further developed aeolian morphologic patterns?

In Chapter 4, we studied the influence of elevated buildings with poles on airflow and sed-

iment transport. As buildings are placed on poles, the approaching wind flows not only around and over the top of the building, but also below buildings. The wind entering the gap underneath the buildings is accelerated due to the funneling effect. The flow speed-up is slightly higher as it passes the gap between the poles, due to additional flow compression. Upon leaving the gap, the wind speed decreases considerably, causing sediment deposition just behind the buildings. For buildings placed directly on the beach surface, small recirculation regions with a pair of counter-rotating vortices occur in the lee of each building.

Elevated buildings on poles modify substantially the wind-induced bed shear stress (see Figure 4.9). The area of reduced bed shear stress in front of the elevated buildings slightly grows in spatial extent compared to the buildings placed directly on the bed. Conversely, the bed shear stress immediately upwind of the buildings increases as buildings are placed on poles. In addition to the high bed shear stress through the gaps between neighboring buildings, strongly elevated bed shear stress is formed below the buildings and just behind the buildings. Furthermore, the increased bed shear stress through the gaps between buildings continues far longer behind the gaps. The lowest bed shear stress values for buildings placed on the bed surface form immediately behind the buildings. However it is being pushed further downstream for elevated buildings.

Our study on duneward sediment supply for a wide range of tested pole heights showed that not all the pole heights enhance sediment transport to the dunes. When looking at just behind the row of buildings, those with pole height ratio, p_h/w (the ratio of the pole height to building width), up to 0.3 have minor influence on the duneward sediment transport. The pole height ratios between 0.3 to 1.0 show notably increased changes in duneward transport, the changes become milder for taller poles. Further downstream of the buildings, the net duneward sediment transport fluxes decrease and even show negative impacts on sediment supply to the dunes for some of the pole heights. The buildings on taller pole heights always provide higher sediment transport fluxes to the dunes, except for far downstream of the buildings where the flow is being recovered as it joins the undisturbed flow downstream of the buildings. This downstream location shows higher transports for shorter pole heights.

6.1.1. REFLECTION ON THE MAIN RESEARCH GOAL

THE main goal of this research was *to understand the influence of buildings on airflow patterns and wind-driven morphologic bedforms around buildings at the beach environment.* Numerical models were developed to study the airflow patterns, sediment trans-

port and associated erosion-deposition patterns around buildings. It revealed that beach buildings depending on their characteristics (dimensions and pole height), positioning (relative to each other) and the orientation (with respect to the dominant wind direction) determine the airflow structures and aeolian bedforms. In addition, our findings showed that buildings could largely affect the sand supply from the beach to the area downwind of the row of buildings. Hence, buildings might enhance the dune growth by steering more sediments to the dunes, or conversely slow down the process by trapping sediments in their upwind. In case of multiple buildings close to each other, distinct airflow patterns were found in the lee of buildings. We derived that there is a critical gap width that beyond which the airflow and sediment transport patterns develop independently from neighboring buildings. Through the influence of wind direction on flow structures around buildings, the wind direction changes the location, size and orientation of the recirculation vortices that form adjacent to buildings. We found that relations exist between the characteristics of these vortices and the sediment transport patterns (i.e. length and width of downwind deposition) around buildings.

6.2. RECOMMENDATIONS

6.2.1. MODELLING A ROW OF BUILDINGS IN FRONT OF THE DUNES

IN this thesis, we studied the influence of buildings characteristics and positioning on airflow and sediment transport patterns in their surrounding when they are placed close to each other and on the open beach surface. However in the actual beach, buildings are often placed at small distance in front of the dunes foot.

In Section 5.3.1, the OpenFOAM model was used to examine the airflow patterns when buildings are placed in front of dunes. The dune model was then further developed by Jonkheer (2022) to study the airflow and sediment transport over dunes alone with different slope angles and wind directions. We did not consider the sediment transport around the buildings and over the dunes in a combined beach-dune system yet. Placing buildings in front of the dunes notably changes the flow structures hence the sediment transport, especially in the area bounded by the row of buildings and the dunes foot. Therefore, studying the buildings in front of the dune systems increases insights on understanding the sediment transport in real beach cases.

6.2.2. INFLUENCE OF THE DISTANCE BETWEEN BUILDINGS ROW AND THE DUNES FOOT

TO provide initial insights on duneward sediment transport, we computed average sediment transport fluxes passing multiple lines at different locations downstream of the buildings row. The locations of these lines were chosen as indications for the dune foot positions in the lee of the buildings. However, the results presented in this thesis only include the implications for the building-induced effects on duneward transport. The more complicated airflow structures, hence the more complicated sediment transport patterns occur in the space between the lee face of the buildings and the dune foot compared to when buildings are placed in an open beach. Therefore, the examination of the influence of the distance between the buildings row and the dunes foot on sediment transport provides interesting insights into coastal management.

6.2.3. WIND DIRECTION WITH RESPECT TO THE INDIVIDUAL BUILDINGS

IN Chapter 3, we quantified the impact of varying wind direction relative to the row of buildings close to each other, when the longer face of the buildings is parallel to the cross-shore direction. However, buildings are sometimes placed at the beach in a manner that individual building rotates relative to the cross-shore direction. Understanding the influence of individual building orientation at the beach on bed topography around buildings and potential duneward sediment transport could be an interesting topic for future studies (Stevers, 2021; Hobeika, 2021).

6.2.4. INFLUENCE OF COUPLING INTERVAL BETWEEN OPENFOAM AND AEOLIS

THE new coupled model was developed to predict fully-developed morphologic patterns around buildings. The coupled model computes the detailed bed shear stress distribution using OpenFOAM model every ΔT seconds of estimating bed topography in AeoLiS. In our initial simulations with the coupled model, we updated the bed shear stress every 20 hours of estimating bed level changes. This updating interval still requires additional analysis. It can be reduced to a very small value, i.e. in the order of seconds or minutes. This might increase the precision of the bedform predictions, but also substantially increases the computational costs. On the other hand, the rate of growth in bedform patterns close to the buildings might not be so much fast to need a more frequent update of bed shear stress. In addition, the rate of change in bedforms might differ over time. Therefore, further investigations and sensitivity analysis need to be taken into account to find an optimum time

interval that satisfies the precision of the simulations, while reducing the computational costs.

6.2.5. CONSIDERATION OF THE SUPPLY LIMITED FACTORS

THE building-induced influences on the fully-developed bed morphology around buildings were simulated using the coupled OpenFOAM-AeoLiS model. In our simulations, the impacts of supply-limiting factors such as vegetation, surface moisture, beach slope, grain size and sorting, beach armouring, sea crusts and shells, non-erodible roughness elements, soluble salts and fetch length at the beach were ignored. However, AeoLiS is capable of modelling spatiotemporal changes in beach surface properties. By considering these supply-liming conditions the sediment availability at the beach for aeolian transport might be limited. Therefore, further research including the influence of supply-limiting factors provides more realistic predictions of the morphologic patterns around buildings.

6.2.6. SEASONALLY VERSUS PERMANENTLY PLACED BEACH BUILDINGS

VACATION buildings in actual beaches are often placed seasonally, e.g. during the summer. The current settings of the coupled OpenFOAM-AeoLiS model are capable of considering permanent buildings. To consider the implications on seasonally-placed buildings, further technical improvements in the model are needed to include buildings in tourism seasons and remove them when looking at morphologic patterns outside of the main tourism seasons. Furthermore, the coupled model could be further modified to consider the unsteady wind conditions. Then, the yearly-measured time series of the wind speed and direction could be implemented in the coupled model including the seasonally placed buildings at the beach to obtain more realistic evaluations of the duneward sediment supply over a year. Such a model could become computationally very expensive, if we run the OpenFOAM model for many different wind conditions. Different approaches might be used to make a more computationally efficient model. For example, an analytical formulation based on the results derived from OpenFOAM model can be generated that estimates the bed shear stress without running the OpenFOAM model.

6.2.7. DEVELOPMENT OF A GAME-BASED MODEL

THE insights obtained from this thesis could be applied in a game-based model that offers guidance to both the beach buildings owners and the coastal managers. This guidance could help local owners to place the buildings in front of the dunes in a manner to minimize the need for sand removal measures, while satisfying the coastal managers by

minimising the negative influences of the buildings on dunes or even enhancing the dunes growth hence their flood safety functioning.

The same approach was used by Den Haan et al. (2020) to develop a virtual river game that enables non-expert stakeholders to collaboratively explore the various river interventions and fosters the social learning.

List of References

Bagnold, R. A. (1936). The movement of desert sand. Proceedings of the Royal Society of London. *Series A-Mathematical and Physical Sciences*, *157*(892), 594–620. https://doi.org/10.1098/rspa.1936.0218

Bagnold, R. A. (1937). The transport of sand by wind. *The Geographical Journal*, *89*(5), 409–438. https://doi.org/10.2307/1786411

Bagnold, R. A. (1941). *The Physics of Blown Sand and Desert Dunes*. Methuen, London.

Bauer, B. O., & Davidson-Arnott, R. G. (2003). A general framework for modeling sediment supply to coastal dunes including wind angle, beach geometry, and fetch effects. *Geomorphology*, *49*(1-2), 89–108. https://doi.org/10.1016/S0169-555X(02)00165-4

Bauer, B. O., Davidson-Arnott, R. G. D., Hesp, P. A., Namikas, S. L., Ollerhead, J., & Walker, I. J. (2009). Aeolian sediment transport on a beach: Surface moisture, wind fetch, and mean transport. *Geomorphology*, *105*(1-2), 106–116. https://doi.org/10.1016/j.geomorph.2008.02.016

Bauer, B. O., Hesp, P. A., Walker, I. J., & Davidson-Arnott, R. G. (2015). Sediment transport (dis) continuity across a beach–dune profile during an offshore wind event. *Geomorphology*, *245*. https://doi.org/10.1016/j.geomorph.2015.05.004

Becker, S., Lienhart, H., & Durst, F. (2002). Flow around three-dimensional obstacles in boundary layers. *Journal of Wind Engineering and Industrial Aerodynamics*, *90*(4-5), 265–279. https://doi.org/10.1016/S0167-6105(01)00209-4

Beranek, W. J. (1984). Wind environment around single buildings of rectangular shape. *Heron*, *29*(1), 4–31.

Beyers, M., & Waechter, B. (2008). Modeling transient snowdrift development around complex three-dimensional structures. *Journal of Wind Engineering and Industrial Aerodynamics*, *96*(10-11), 1603–1615. https://doi.org/10.1016/j.jweia.2008.02.032

Bitsuamlak, G. T., Stathopoulos, T., & Bedard, C. (2004). Numerical evaluation of wind flow over complex terrain. *Journal of aerospace engineering*, *17*(4), 135–145. https://doi.org/10.1061/(ASCE)0893-1321(2004)17:4(135)

Blocken, B., Stathopoulos, T., & Carmeliet, J. (2007). CFD simulation of the atmospheric boundary layer: wall function problems. *Atmospheric environment*, *41*(2), 238–252. https://doi.org/10.1016/j.atmosenv.2006.08.019

Blocken, B., Stathopoulos, T., Carmeliet, J., & Hensen, J. L. (2011). Application of computational fluid dynamics in building performance simulation for the outdoor environment: an overview. *Journal of building performance simulation*, *4*(2), 157–184. https://doi.org/10.1080/19401493.2010.513740

Bochev-Van der Burgh, L. M., Wijnberg, K. M., & Hulscher, S. J. (2011). Decadal-scale morphologic variability of managed coastal dunes. *Coastal engineering*, *58*(9), 927–936. https://doi.org/10.1016/j.coastaleng.2011.05.013

Boulghobra, N. (2016). Climatic data and satellite imagery for assessing the aeolian sand deposit and barchan migration, as a major risk sources in the region of In-Salah (Central Algerian Sahara). *Arabian Journal of Geosciences*, *9*. https://doi.org/10.1007/s12517-016-2491-x

Bredberg, J. (2000). On the wall boundary condition for turbulence models. *Internal Report 00/4, Chalmers University of Technology, Department of Thermo and Fluid Dynamics*, 8–16.

Bruno, L., & Fransos, D. (2015). Sand transverse dune aerodynamics: 3D coherent flow structures from a computational study. *Journal of Wind Engineering and Industrial Aerodynamics*, *147*, 291–301. https://doi.org/10.1016/j.jweia.2015.07.014

Bruno, L., Horvat, M., & Raffaele, L. (2018). Windblown sand along railway infrastructures: A review of challenges and mitigation measures. *Journal of Wind Engineering and Industrial Aerodynamics*, *177*. https://doi.org/10.1016/j.jweia.2018.04.021

Caretto, L. S., Gosman, A. D., Patankar, S. V., & Spalding, D. B. (1973). Two calculation procedures for steady, three-dimensional flows with recirculation. *In: Proceedings of the third international conference on numerical methods in fluid mechanics. Springer, Berlin, Heidelberg*, *19*, 60–68. https://doi.org/10.1007/BFb0112677

Chou, J. H., & Chao, S. Y. (2000). Branching of a horseshoe vortex around surface-mounted rectangular cylinders. *Experiments in fluids*, *28*(5), 394–402. https://doi.org/10.1007/s003480050399

Coceal, O., Thomas, T. G., Castro, I. P., & Belcher, S. E. (2006). Mean flow and turbulence statistics over groups of urban-like cubical obstacles. *Boundary-Layer Meteorology*, *121*(3), 491–519. https://doi.org/10.1007/s10546-006-9076-2

Cooke, R. U., Warren, A., & Goudie, A. S. (1993). *Desert geomorphology*. CRC Press.

Cornelis, W. M., & Gabriels, D. (2003). The effect of surface moisture on the entrainment of dune sand by wind: an evaluation of selected models. *Sedimentology*, *50*(4), 771–790. https://doi.org/10.1046/j.1365-3091.2003.00577.x

Davidson-Arnott, R. G., MacQuarrie, K., & Aagaard, T. (2005). The effect of wind gusts, moisture content and fetch length on sand transport on a beach. *Geomorphology*, *68*(1-2), 115–129. https://doi.org/10.1016/j.geomorph.2004.04.008

De Vries, S., de Vries, J. V. T., Van Rijn, L. C., Arens, S. M., & Ranasinghe, R. W. M. R. J. B. (2014). Aeolian sediment transport in supply limited situations. *Aeolian Research*, *12*. https://doi.org/10.1016/j.aeolia.2013.11.005

De Vries, S., Southgate, H. N., Kanning, W., & Ranasinghe, R. W. M. R. J. B. (2012). Dune behavior and aeolian transport on decadal timescales. *Coastal engineering*, *67*, 41–53. https://doi.org/10.1016/j.coastaleng.2012.04.002

Delgado-Fernandez, I. (2010). A review of the application of the fetch effect to modelling sand supply to coastal foredunes. *Aeolian Research*, *2*(2-3), 61–70. https://doi.org/10.1016/j.aeolia.2010.04.001

Delgado-Fernandez, I., & Davidson-Arnott, R. (2011). Meso-scale aeolian sediment input to coastal dunes: The nature of aeolian transport events. *Geomorphology*, *126*(1-2), 217–232. https://doi.org/10.1016/j.geomorph.2010.11.005

Den Haan, R. J., van der Voort, M. C., Baart, F., Berends, K. D., van den Berg, M. C., Straatsma, M. W., Geenen, A. J. P., & Hulscher, S. J. M. H. (2020). The Virtual River Game: Gaming using models to collaboratively explore river management complexity. *Environmental modelling software*, *134*. https://doi.org/10.1016/j.envsoft.2020.104855

Enteria, N. A. (2016). CFD evaluation of Philippine detached structure with different roofing designs. *Infrastructures*, *1*(1), 3. https://doi.org/10.3390/infrastructures1010003

Fackrell, J. E. (1984). Parameters characterising dispersion in the near wake of buildings. *Journal of Wind Engineering and Industrial Aerodynamics*, *16*(1), 97–118. https://doi.org/10.1016/0167-6105(84)90051-5

Ferziger, J. H., & Peric, M. (2002). *Computational methods for fluid dynamics, third edition*. Springer, Berlin.

Fluent, A. (2013). *ANSYS fluent theory guide 15.0*. Canonsburg, PA.

Gao, Y., & Chow, W. K. (2005). Numerical studies on air flow around a cube. *Journal of Wind Engineering and Industrial Aerodynamics*, *93*(2), 115–135. https://doi.org/10.1016/j.jweia.2004.11.001

García-Romero, L., Hernández-Cordero, A. I., Fernández-Cabrera, E., Peña-Alonso, C., Hernández-Calvento, L., & Pérez-Chacón, E. (2016). Urban-touristic impacts on the aeolian sedimentary systems of the Canary Islands: conflict between development and conservation. *Island Studies Journal*, *11*(1).

Greeley, R., & Iversen, J. D. (1985). *Wind as a geological process: on Earth, Mars, Venus and Titan*. Cambridge University Press, New York.

Hallin, C., Huisman, B. J., Larson, M., Walstra, D. J. R., & Hanson, H. (2019). Impact of sediment supply on decadal-scale dune evolution—Analysis and modelling of the Kennemer dunes in the Netherlands. *Geomorphology*, *337*, 94–110. https://doi.org/10.1016/j.geomorph.2019.04.003

Hardisty, J., & Whitehouse, R. J. S. (1988). Evidence for a new sand transport process from experiments on Saharan dunes. *Nature, 332*(6164), 532–534. https://doi.org/10.1038/332532a0

He, W., Huang, N., Xu, B., & Wang, W. (2018). Numerical simulation of wind-sand movement in the reversed flow region of a sand dune with a bridge built downstream. *The European Physical Journal E, 41*. https://doi.org/10.1140/epje/i2018-11660-5

Hesp, P. A., & Smyth, T. A. (2021). CFD flow dynamics over model scarps and slopes. *Physical Geography, 42*(1), 1–24. https://doi.org/10.1080/02723646.2019.1706215

Hobeika, N. (2021). *CFD, sensitivity analysis and optimisation to promote the formation of dunes*. MSc thesis, Delft University of Technology.

Hoonhout, B. M., & De Vries, S. (2016). A process-based model for aeolian sediment transport and spatiotemporal varying sediment availability. *Journal of Geophysical Research: Earth Surface, 121*(8), 1555–1575. https://doi.org/10.1002/2015JF003692

Hoonhout, B. M., & De Vries, S. (2019). Simulating spatiotemporal aeolian sediment supply at a mega nourishment. *Coastal engineering, 145*, 21–35. https://doi.org/10.1016/j.coastaleng.2018.12.007

Horikawa, K., Hotta, S., & Kraus, N. C. (1986). Literature review of sand transport by wind on a dry sand surface. *Coastal Engineering, 9*(6), 503–526. https://doi.org/10.1016/0378-3839(86)90001-3

Horikawa, K., Hotta, S., Kubota, S., & Katori, S. (1983). On the sand transport rate by wind on a beach. *Coastal Engineering in Japan, 26*(1), 101–120. https://doi.org/10.1080/05785634.1983.11924362

Hsu, S. A. (1971). Wind stress criteria in eolian sand transport. *Journal of Geophysical Research, 76*(36), 8684–8686. https://doi.org/10.1029/JC076i036p08684

Hunt, J. C. R. (1971). The effect of single buildings and structures. *Philosophical Transactions of the Royal Society of London. Series A, Mathematical and Physical Sciences, 269*(1199), 457–467. https://doi.org/10.1098/rsta.1971.0044

Hunt, J. C. R., Abell, C. J., Peterka, J. A., & Woo, H. (1978). Kinematical studies of the flows around free or surface-mounted obstacles; applying topology to flow visualization. *Journal of Fluid Mechanics, 86*(1), 179–200. https://doi.org/10.1017/S0022112078001068

Iaccarino, G., Ooi, A., Durbin, P. A., & Behnia, M. (2003). Reynolds averaged simulation of unsteady separated flow. *International Journal of Heat and Fluid Flow, 24*(2), 147–156. https://doi.org/10.1016/S0142-727X(02)00210-2

Iversen, J. D., Greeley, R., White, B. R., & Pollack, J. B. (1976). The effect of vertical distortion in the modeling of sedimentation phenomena: Martian crater wake streaks. *Journal of Geophysical Research, 81*(26), 4846–4856. https://doi.org/10.1029/JB081i026p04846

Iversen, J. D., Wang, W. P., Rasmussen, K. R., Mikkelsen, H. E., Hasiuk, J. F., & Leach, R. N. (1990). The effect of a roughness element on local saltation transport. *Journal of Wind Engineering and Industrial Aerodynamics, 36*, 845–854. https://doi.org/10.1016/0167-6105(90)90081-M

Iversen, J. D., Wang, W. P., Rasmussen, K. R., Mikkelsen, H. E., & Leach, R. N. (1991). Roughness element effect on local and universal saltation transport. *Acta Mechanica Supplementum, 2*, 65–75. https://doi.org/10.1007/978-3-7091-6703-8_5

Jackson, Beyers, J. H. M., Lynch, K., Cooper, J. A. G., Baas, A. C. W., & Delgado-Fernandez, I. (2011). Investigation of three-dimensional wind flow behaviour over coastal dune morphology under offshore winds using computational fluid dynamics (CFD) and ultrasonic anemometry. *Earth Surface Processes and Landforms, 36*(8), 1113–1124. https://doi.org/10.1002/esp.2139

Jackson, D. W., Beyers, M., Delgado-Fernandez, I., Baas, A. C., Cooper, A. J., & Lynch, K. (2013). Airflow reversal and alternating corkscrew vortices in foredune wake zones during perpendicular and oblique offshore winds. *Geomorphology, 187*, 86–93. https://doi.org/10.1016/j.geomorph.2012.12.037

Jackson & Nordstrom. (2011). Aeolian sediment transport and landforms in managed coastal systems: a review. *Aeolian research, 3*(2), 181–196. https://doi.org/10.1016/j.aeolia.2011.03.011

Jonkheer, A. J. (2022). *Assessment of the influence of incident wind angle and dune slope inclination on sediment transport patterns in coastal dunes*. MSc thesis, University of Twente.

Joubert, E. C., Harms, T. M., Muller, A., Hipondoka, M., & Henschel, J. R. (2012). A CFD study of wind patterns over a desert dune and the effect on seed dispersion. *Environmental fluid mechanics, 12*(1), 23–44. https://doi.org/10.1007/s10652-011-9230-3

Kawamura, R. (1951). Study on sand movement by wind. *Reports of Physical Sciences Research Institute of Tokyo University, 5*(3-4), 95–112.

King, J., Nickling, W. G., & Gillies, J. A. (2005). Representation of vegetation and other nonerodible elements in aeolian shear stress partitioning models for predicting transport threshold. *Journal of Geophysical Research: Earth Surface, 110*(F4). https://doi.org/10.1029/2004JF000281

King, M. F., Gough, H. L., Halios, C., Barlow, J. F., Robertson, A., Hoxey, R., & Noakes, C. J. (2017). Investigating the influence of neighbouring structures on natural ventilation potential of a full-scale cubical building using time-dependent CFD. *Journal of Wind Engineering and Industrial Aerodynamics, 169*, 265–279. https://doi.org/10.1016/j.jweia.2017.07.020

Kroy, K., Sauermann, G., & Herrmann, H. J. (2002). Minimal model for aeolian sand dunes. *Physical Review E, 66*(3).

Lakehal, D., & Rodi, W. (1997). Calculation of the flow past a surface-mounted cube with two-layer turbulence models. *Journal of Wind Engineering and Industrial Aerodynamics*, *67*, 65–78. https://doi.org/10.1016/S0167-6105(97)00063-9

Launder, B. E., & Sharma, B. I. (1974). Application of the energy-dissipation model of turbulence to the calculation of flow near a spinning disc. *Letters in heat and mass transfer*, *1*(2), 131–138.

Launder, B. E., & Spalding, D. B. (1974). The numerical computation of turbulent flows. *Computer Methods in Applied Mechanics and Engineering*, *3*, 269–289. https://doi.org/10.1016/B978-0-08-030937-8.50016-7

Lazarus, E. D., Ellis, M. A., Murray, A. B., & Hall, D. M. (2016). An evolving research agenda for human–coastal systems. *Geomorphology*, *256*. https://doi.org/10.1016/j.geomorph.2015.07.043

Lefebvre, A. (2019). Three-dimensional flow above river bedforms: Insights from numerical modeling of a natural dune field (Río Paraná, Argentina). *Journal of Geophysical Research: Earth Surface*, *124*(8), 2241–2264. https://doi.org/10.1029/2018JF004928

Leitl, B., & Schatzmann, M. (2010). Cedval at Hamburg University. https://mi-pub.cen.uni-hamburg.de/index.php?id=433

Lettau, K., & Lettau, H. (1977). Experimental and micrometeorological field studies of dune migration. *In: Lettau, K. and Lettau, H. (Eds.), Exploring the World's Driest Climate. IES Report, vol. 101. University of Wisconsin Press, Madison, WI*, pp. 110–147.

Liu, F. (2016). A thorough description of how wall functions are implemented in OpenFOAM. *Proceedings of CFD with OpenSource Software*, 1–33.

Liu, Zhang, Q., Fan, F., & Shen, S. (2018). Experiments on natural snow distribution around simplified building models based on open air snow-wind combined experimental facility. *Journal of Wind Engineering and Industrial Aerodynamics*, *173*. https://doi.org/10.1016/j.jweia.2017.12.010

Liu, Zhang, W., Qu, J., Zhang, K., & Han, Q. (2011). Controlling windblown sand problems by an artificial gravel surface: a case study over the gobi surface of the Mogao Grottoes. *Geomorphology*, *134*(3-4). https://doi.org/10.1016/j.geomorph.2011.07.028

Livingstone, I., & Warren, A. (1996). *Aeolian geomorphology: an introduction*. Addison Wesley Longman Ltd.

Logie, M. (1982). Influence of roughness elements and soil moisture of sand to wind erosion. *Catena Supplement*, *1*, 161–173.

Lokin, L. R., Warmink, J. J., Bomers, A., & Hulscher, S. J. M. H. (2022). River dune dynamics during low flows. *Geophysical research letters*, *49*(8), e2021GL097127. https://doi.org/10.1029/2021GL097127

Luo, W., Dong, Z., Qian, G., & Lu, J. (2012). Wind tunnel simulation of the three-dimensional airflow patterns behind cuboid obstacles at different angles of wind incidence, and

their significance for the formation of sand shadows. *Geomorphology*, *139*, 258–270. https://doi.org/10.1016/j.geomorph.2011.10.027

Luo, W., Dong, Z., Qian, G., & Lu, J. (2014). Near-wake flow patterns in the lee of adjacent obstacles and their implications for the formation of sand drifts: a wind tunnel simulation of the effects of gap spacing. *Geomorphology*, *213*, 190–200. https://doi.org/10.1016/j.geomorph.2014.01.008

Luo, W., Lu, J., Qian, G., & Dong, Z. (2016). Influence of the gap ratio on variations in the surface shear stress and on sand accumulation in the lee of two side-by-side obstacles. *Environmental Earth Sciences*, *75*(9), 1–12. https://doi.org/10.1007/s12665-016-5588-3

Maegley, W. J. (1976). Saltation and Martian sandstorms. *Reviews of Geophysics*, *14*(1), 135–142. https://doi.org/10.1029/RG014i001p00135

Marsh, G. P. (1874). *The earth as modified by human action: a new edition of man and nature*. Scribner, Armstrong Company, New York.

Martínez, M. L., Hesp, P. A., & Gallego-Fernández, J. B. (2013). *Coastal dunes: human impact and need for restoration*. In: Martínez, M.L., Gallego-Fernández, J.B., Hesp, P.A. (Eds.), Restoration of Coastal Dunes. Springer Berlin Heidelberg. https://doi.org/10.1007/978-3-642-33445-0_1

Martinuzzi, R., & Tropea, C. (1993). The flow around surface-mounted, prismatic obstacles placed in a fully developed channel flow. *Journal of Fluids Engineering*, *115*(1), 85–92. https://doi.org/10.1115/1.2910118

McKenna Neuman, C., & Bédard, O. (2015). A wind tunnel study of flow structure adjustment on deformable sand beds containing a surface-mounted obstacle. *Journal of Geophysical Research: Earth Surface*, *120*(9), 1824–1840. https://doi.org/10.1002/2015JF003475

McKenna Neuman, C., Li, B., & Nash, D. (2012). Micro-topographic analysis of shell pavements formed by aeolian transport in a wind tunnel simulation. *Journal of Geophysical Research: Earth Surface*, *117*(F4). https://doi.org/10.1029/2012JF002381

McKenna Neuman, C., Sanderson, R. S., & Sutton, S. (2013). Vortex shedding and morphodynamic response of bed surfaces containing non-erodible roughness elements. *Geomorphology*, *198*, 45–56. https://doi.org/10.1016/j.geomorph.2013.05.011

Meinders, E. R., Hanjalic, K., & Martinuzzi, R. J. (1999). Experimental study of the local convection heat transfer from a wall-mounted cube in turbulent channel flow. *Trans. ASME: J. Heat Transfer*, *121*(3), 564–573. https://doi.org/10.1115/1.2826017

Meroney, R. N. (1982). Turbulent diffusion near buildings, Engineering Meteorology. *E. J. Plate, Ed., Elsevier Scientific*, 481–525.

Mestoul, D., Bensalem, R., & Adolphe, L. (2017). Modeling of urban form against sand accumulation in the city of Gourara in southern Algeria. *Energy Procedia*, *122*. https://doi.org/10.1016/j.egypro.2017.07.405

Middleton, N. J., & Sternberg, T. (2013). Climate hazards in drylands: A review. *Earth-Science Reviews*, *126*. https://doi.org/10.1016/j.earscirev.2013.07.008

Moukalled, F., Mangani, L., & Darwish, M. (2016). The Finite Volume Method. In: The Finite Volume Method in Computational Fluid Dynamics. Fluid Mechanics and Its Applications. *Springer, Cham*, *113*. https://doi.org/10.1007/978-3-319-16874-6_5

Nickling, W. G., & Davidson-Arnott, R. G. D. (1990). Aeolian sediment transport on beaches and coastal sand dunes. *Proceedings of the Symposium on Coastal Sand Dunes. National Research Council of Canada*, pp 1–35.

Nickling, W. G., & Ecclestone, M. (1981). The effects of soluble salts on the threshold shear velocity of fine sand. *Sedimentology*, *28*(4), 505–510. https://doi.org/10.1111/j.1365-3091.1981.tb01698.x

Nickling, W. G., & Neuman, C. M. (2009). Aeolian sediment transport. *In Geomorphology of desert environments, Springer, Dordrecht*, 517–555. https://doi.org/10.1007/978-1-4020-5719-9_17

Nolet, C., Poortinga, A., Roosjen, P., Bartholomeus, H., & Ruessink, G. (2014). Measuring and modeling the effect of surface moisture on the spectral reflectance of coastal beach sand. *PLoS One*, *9*(11), e112151. https://doi.org/10.1371/journal.pone.0112151

Nordstrom, K. F. (1994). Beaches and dunes of human-altered coasts. *Progress in physical Geography*, *18*(4), 497–516. https://doi.org/10.1177/030913339401800402

Nordstrom, K. F. (2000). *Beaches and dunes of developed coasts*. Cambridge University Press.

Nordstrom, K. F., & Jackson, N. L. (1992). Effect of source width and tidal elevation changes on aeolian transport on an estuarine beach. *Sedimentology*, *39*(5), 769–778. https://doi.org/10.1111/j.1365-3091.1992.tb02152.x

Nordstrom, K. F., & Jackson, N. L. (1993). The role of wind direction in eolian transport on a narrow sandy beach. *Earth Surface Processes and Landforms*, *18*(8), 675–685. https://doi.org/10.1002/esp.3290180803

Nordstrom, K. F., & Jackson, N. L. (1998). Effects of a high rise building on wind flow and beach characteristics at Atlantic City, NJ, USA. *Ocean coastal management*, *39*(3), 245–263. https://doi.org/10.1016/S0964-5691(97)00036-7

Nordstrom, K. F., Lampe, R., & Vandemark, L. M. (2000). Reestablishing naturally functioning dunes on developed coasts. *Environmental management*, *25*(1), 37–51. https://doi.org/10.1007/s002679910004

Nordstrom, K. F., & McCluskey, J. M. (1984). Considerations for control of house construction in coastal dunes. *Coastal Management*, *12*(4), 385–402. https://doi.org/10.1080/08920758409361972

Nordstrom, K. F., & McCluskey, J. M. (1985). The effects of houses and sand fences on the eolian sediment budget at Fire Island, New York. *Journal of Coastal Research, 1*(1), 39–46. http://www.jstor.org/stable/4297009

Nordstrom, K. F., McCluskey, J. M., & Rosen, P. S. (1986). Aeolian processes and dune characteristics of a developed shoreline: Westhampton Beach, New York. *Aeolian Geomorphology*, 131–147.

O'brien, M. P., & Rindlaub, B. D. (1936). The transportation of sand by wind. *Civil Engineering, 6*(5), 325–327.

Okafor, C. V., Ezeokonkwo, U. J., Obodoh, D. A., & Ogunoh, P. (2018). Atmospheric boundary layer simulation using wall function approach in openfoam CFD software. *European Journal of Engineering and Technology Research, 3*(2), 1–6. https://doi.org/10.24018/ejeng.2018.3.2.597

Oke, T. R., Mills, G., Christen, A., & Voogt, J. A. (2017). *Urban climates*. Cambridge University Press.

Owen, P. R. (1964). Saltation of uniform grains in air. *Journal of Fluid Mechanics, 20*(2), 225–242. https://doi.org/10.1017/S0022112064001173

Paarlberg, A. J., Dohmen-Janssen, C. M., Hulscher, S. J., & Termes, P. (2007). A parameterization of flow separation over subaqueous dunes. *Water Resources Research, 43*(12). https://doi.org/10.1029/2006WR005425

Paola, C., & Voller, V. R. (2005). A generalized Exner equation for sediment mass balance. *Journal of Geophysical Research: Earth Surface, 110*(F4). https://doi.org/10.1029/2004JF000274

Peterka, J. A., Meroney, R. N., & Kothari, K. M. (1985). Wind flow patterns about buildings. *Journal of Wind Engineering and Industrial Aerodynamics, 21*(1), 21–38. https://doi.org/10.1016/0167-6105(85)90031-5

Poppema, D. W. (2022). *Morphological effects of buildings in a sandy beach environment* (Doctoral dissertation). University of Twente. https://doi.org/10.3990/1.9789036553520

Poppema, D. W., Baas, A. C., Hulscher, S. J., & Wijnberg, K. M. (2022a). Cellular automaton modelling of the effects of buildings on aeolian bedform dynamics. *Aeolian Research, 59*, 100840. https://doi.org/10.1016/j.aeolia.2022.100840

Poppema, D. W., Wijnberg, K. M., Mulder, J. P., & Hulscher, S. J. (2022b). Deposition patterns around buildings at the beach: Effects of building spacing and orientation. *Geomorphology, 401*, 108114. https://doi.org/10.1016/j.geomorph.2022.108114

Poppema, D. W., Wijnberg, K. M., Mulder, J. P., Vos, S. E., & Hulscher, S. J. (2021). The effect of building geometry on the size of aeolian deposition patterns: Scale model experiments at the beach. *Coastal engineering, 168*, 103866. https://doi.org/10.1016/j.coastaleng.2021.103866

Pourteimouri, P., Campmans, G. H. P., Wijnberg, K. M., & Hulscher, S. J. M. H. (2022). A Numerical Study on the Impact of Building Dimensions on Airflow Patterns and Bed Morphology around Buildings at the Beach. *Journal of marine science and engineering*, *10*(1), 13. https://doi.org/10.3390/jmse10010013

Pourteimouri, P., Campmans, G. H. P., Wijnberg, K. M., & Hulscher, S. J. M. H. (2023). How wind direction and building spacing influences airflow patterns and sediment transport patterns around a row of beach buildings: A numerical study. *Aeolian Research*, *61*, 100867. https://doi.org/10.1016/j.aeolia.2023.100867

Pye, K., & Tsoar, H. (2008). *Aeolian sand and sand dunes*. Springer Science Business Media.

Qian, G., Dong, Z., Luo, W., & Lu, J. (2011). Mean airflow patterns upwind of topographic obstacles and their implications for the formation of echo dunes: A wind tunnel simulation of the effects of windward slope. *Journal of Geophysical Research: Earth Surface*, *116*(F4). https://doi.org/10.1029/2011JF002020

Raffaele, L., & Bruno, L. (2019). Windblown sand action on civil structures: Definition and probabilistic modelling. *Engineering Structures*, *178*. https://doi.org/10.1016/j.engstruct.2018.10.017

Richards, P. J., & Hoxey, R. P. (1993). Appropriate boundary conditions for computational wind engineering models using the $k-\varepsilon$ turbulence model. *Journal of wind engineering and industrial aerodynamics*, *46*, 145–153. https://doi.org/10.1016/0167-6105(93)90124-7

Richards, P. J., & Hoxey, R. P. (2012). Pressures on a cubic building—Part 1: Full-scale results. *Journal of Wind Engineering and Industrial Aerodynamics*, *102*, 72–86. https://doi.org/10.1016/j.jweia.2011.11.004

Salman, A. B., Howari, F. M., El-Sankary, M. M., Wali, A. M., & Saleh, M. M. (2010). Environmental impact and natural hazards on Kharga Oasis monumental sites, Western Desert of Egypt. *Journal of African Earth Sciences*, *58*(2). https://doi.org/10.1016/j.jafrearsci.2010.03.011

Sauermann, G., Kroy, K., & Herrmann, H. J. (2001). Continuum saltation model for sand dunes. *Physical Review E*, *64*(3). https://doi.org/10.1103/PhysRevE.64.031305

Schlichting, J., H. Kestin. (1961). *Boundary Layer Theory, Vol. 121*. Springer.

Shah, K. B., & Ferziger, J. H. (1997). A fluid mechanicians view of wind engineering: Large eddy simulation of flow past a cubic obstacle. *Journal of wind engineering and industrial aerodynamics*, *67*, 211–224. https://doi.org/10.1016/S0167-6105(97)00074-3

Shapiro, A. H. (1953). The Dynamics and Thermodynamics of Compressible Fluid Flow. *The Ronald Press Company, New York*, *1*.

Sherman, D. J., Jackson, D. W., Namikas, S. L., & Wang, J. (1998). Wind-blown sand on beaches: an evaluation of models. *Geomorphology*, *22*(2), 113–133. https://doi.org/10.1016/S0169-555X(97)00062-7

Sherman, D. J., & Li, B. (2012). Predicting aeolian sand transport rates: A reevaluation of models. *Aeolian Research*, *3*(4), 371–378. https://doi.org/10.1016/j.aeolia.2011.06.002

Silva, F. G., Wijnberg, K. M., de Groot, A. V., & Hulscher, S. J. (2018). The influence of groundwater depth on coastal dune development at sand flats close to inlets. *Ocean dynamics*, *68*. https://doi.org/10.1007/s10236-018-1162-8

Smith, A. B., Jackson, D. W., Cooper, J. A. G., & Hernández-Calvento, L. (2017). Quantifying the role of urbanization on airflow perturbations and dunefield evolution. *Earth's Future*, *5*(5). https://doi.org/10.1002/2016EF000524

Smyth, T. A. (2016). A review of Computational Fluid Dynamics (CFD) airflow modelling over aeolian landforms. *Aeolian research*, *22*, 153–164. https://doi.org/10.1016/j.aeolia.2016.07.003

Smyth, T. A., & Hesp, P. A. (2015). Aeolian dynamics of beach scraped ridge and dyke structures. *Coastal Engineering*, *99*, 38–45. https://doi.org/10.1016/j.coastaleng.2015.02.011

Stevers, V. (2021). *The effects of beach house configurations on dune-ward sediment transport*. MSc thesis, Delft University of Technology.

Sutton, S. L. F., & McKenna Neuman, C. (2008). Sediment entrainment to the lee of roughness elements: Effects of vortical structures. *Journal of Geophysical Research: Earth Surface*, *113*(F2). https://doi.org/10.1029/2007JF000783

Tennekes, H., & Lumley, J. L. (1972). *A first course in turbulence*. MIT Press, Cambridge.

Thiis, T. K. (2003). Large scale studies of development of snowdrifts around buildings. *Journal of Wind Engineering and Industrial Aerodynamics*, *91*(6). https://doi.org/10.1016/S0167-6105(02)00474-9

Thiis, T. K., & Gjessing, Y. (1999). Large-scale measurements of snowdrifts around flat-roofed and single-pitch-roofed buildings. *Cold regions science and technology*, *30*(1-3). https://doi.org/10.1016/S0165-232X(99)00021-X

Tominaga, Y. (2018). Computational fluid dynamics simulation of snowdrift around buildings: Past achievements and future perspectives. *Cold Regions Science and Technology*, *150*. https://doi.org/10.1016/j.coldregions.2017.05.004

Tominaga, Y., Okaze, T., & Mochida, A. (2018). Wind tunnel experiment and CFD analysis of sand erosion/deposition due to wind around an obstacle. *Journal of Wind Engineering and Industrial Aerodynamics*, *182*, 262–271. https://doi.org/10.1016/j.jweia.2018.09.008

Tsoar, H. (1983). Wind tunnel modeling of echo and climbing dunes. *In Developments in Sedimentology, 38*, 247–259. https://doi.org/10.1016/S0070-4571(08)70798-2

Unnikrishnan, S., Ogunremi, A., & Sumner, D. (2017). The effect of incidence angle on the mean wake of surface-mounted finite-height square prisms. *International Journal of Heat and Fluid Flow, 66*, 137–156. https://doi.org/10.1016/j.ijheatfluidflow.2017.05.012

Van der Meulen, F., & Salman, A. H. P. M. (1996). Management of Mediterranean coastal dunes. *Ocean and Coastal Management, 30*(2-3), 177–195. https://doi.org/10.1016/0964-5691(95)00060-7

Van der Wal, D. (1998). Effects of fetch and surface texture on aeolian sand transport on two nourished beaches. *Journal of Arid Environments, 39*(3), 533–547. https://doi.org/10.1006/jare.1997.0364

Versteeg, H. K., & Malalasekera, W. (1995). *An introduction to computational fluid dynamics: the finite volume method*. Prentice Hall, New Jersey.

Vos, S., Anders, K., Kuschnerus, M., Lindenbergh, R., Höfle, B., Aarninkhof, S., & de Vries, S. (2022). A high-resolution 4D terrestrial laser scan dataset of the Kijkduin beach-dune system, The Netherlands. *Scientific Data, 9*(1), 1–11. https://doi.org/10.1038/s41597-022-01291-9

Walker, Davidson-Arnott, R. G., Bauer, B. O., Hesp, P. A., Delgado-Fernandez, I., Ollerhead, J., & Smyth, T. A. (2017). Scale-dependent perspectives on the geomorphology and evolution of beach-dune systems. *Earth-Science Reviews, 171*, 220–253. https://doi.org/10.1016/j.earscirev.2017.04.011

Walker, H. J. (1984). Man's impact on shorelines and nearshore environments: a geomorphological perspective. *Geoforum, 15*(3), 395–417. https://doi.org/10.1016/0016-7185(84)90047-2

Walker & Nickling. (2002). Dynamics of secondary airflow and sediment transport over and in the lee of transverse dunes. *Progress in Physical Geography, 26*(1), 47–75. https://doi.org/10.1191/0309133302pp325ra

Weng, W. S., Hunt, J. C. R., Carruthers, D. J., Warren, A., Wiggs, G. F. S., Livingstone, I., & Castro, I. (1991). Air flow and sand transport over sand-dunes. *In Aeolian grain transport: The erosional environment, Springer, Vienna*. https://doi.org/10.1007/978-3-7091-6703-8_1

White, B. R. (1979). Soil transport by winds on Mars. *Journal of Geophysical Research: Solid Earth, 84*(B9), 4643–4651. https://doi.org/10.1029/JB084iB09p04643

White, F. M. (1991). *Viscous fluid flow*. Mac Graw-Hill International Editions, New York.

Yakhot, A., Liu, H., & Nikitin, N. (2006). Turbulent flow around a wall-mounted cube: A direct numerical simulation. *International journal of heat and fluid flow, 27*(6), 994–1009. https://doi.org/10.1016/j.ijheatfluidflow.2006.02.026

Yen, S. C., & Liu, C. T. (2011). Gap-flow patterns behind twin-cylinders at low Reynolds number. *Journal of mechanical science and technology*, *25*(11). https://doi.org/10.1016/j.geomorph.2015.05.004

Zhang, C. L., Zou, X. Y., Cheng, H., Yang, S., Pan, X. H., Liu, Y. Z., & Dong, G. R. (2007). Engineering measures to control windblown sand in Shiquanhe Town, Tibet. *Journal of wind engineering and industrial aerodynamics*, *95*(1). https://doi.org/10.1016/j.jweia.2006.05.006

Zhao, Y., Li, R., Feng, L., Wu, Y., Niu, J., & Gao, N. (2022). Boundary layer wind tunnel tests of outdoor airflow field around urban buildings: A review of methods and status. *Renewable and Sustainable Energy Reviews*, *167*, 112717. https://doi.org/10.1016/j.rser.2022.112717

Zingg, A. (1953). Wind tunnel studies of movement of sedimentary material. *Proceedings of the fifth Hydraulic Conference Bulletin*, *34*, 111–134.

LIST OF PUBLICATIONS

PEER-REVIEWED JOURNAL PAPERS

1. **Pourteimouri, P.**, Campmans, G. H. P., Wijnberg, K. M., Hulscher, S. J. M. H. (2023). Modelling the influence of beach building pole heights on aeolian morphology and downwind sediment transport. *Geomorphology* (Accepted, in publishing process)

2. **Pourteimouri, P.**, Campmans, G. H. P., Wijnberg, K. M., Hulscher, S. J. M. H. (2023). How wind direction and building spacing influences airflow patterns and sediment transport patterns around a row of beach buildings: A numerical study. *Aeolian Research*, 61, 100867. https://doi.org/10.1016/j.aeolia.2023.100867

3. **Pourteimouri, P.**, Campmans, G. H. P., Wijnberg, K. M., Hulscher, S. J. M. H. (2021). A Numerical Study on the Impact of Building Dimensions on Airflow Patterns and Bed Morphology around Buildings at the Beach. *Journal of Marine Science and Engineering*, 10(1), 13. https://doi.org/10.3390/jmse10010013

4. **Pourteimouri, P.**, Hejazi, K. (2020). Development of an integrated numerical model for simulating wave interaction with permeable submerged breakwaters using extended Navier–Stokes equations. *Journal of Marine Science and Engineering*, 8(2), 87. https://doi.org/10.3390/jmse8020087

BOOK CHAPTERS

1. Wijnberg, K. M., Poppema, D. W., Mulder, J. P. M., Van Bergen, J., Campmans, G. H. P., Galiforni-Silva, F., Hulscher, S. J. M. H., **Pourteimouri, P.** (2021). Beach-dune modelling in support of Building with Nature for an integrated spatial design of urbanized sandy shores. *Building with Nature perspectives: Cross-disciplinary BwN approaches in coastal regions*, 241-260. https://doi.org/10.47982/rius.7.136

CONFERENCE PAPERS AND ABSTRACTS

1. **Pourteimouri, P.**, Campmans, G. H. P., Wijnberg, K. M., Hulscher, S. J. M. H. (2022). Beach buildings on poles and their implications for duneward sediment transport: A numerical study. *37th International Conference on Coastal Engineering (ICCE)*, Sydney, Australia.

2. **Pourteimouri, P.**, Campmans, G. H. P., Wijnberg, K. M., Hulscher, S. J. M. H. (2022). The Impact of Spacing Between Beach Buildings on Aeolian Erosion and Deposition Patterns: A Numerical Study. *39th IAHR World Congress*, Granada, Spain.

3. **Pourteimouri, P.**, Campmans, G. H. P., Wijnberg, K. M., Hulscher, S. J. M. H. (2022). CFD evaluation of airflow patterns around beach houses with different wind facing sides. *13th International ERCOFTAC symposium (ETMM)*, Rhodes, Greece, Online Event.

4. **Pourteimouri, P.**, Campmans, G. H. P., Wijnberg, K. M., Hulscher, S. J. M. H. (2021). How erosion and deposition patterns around a row of holiday cottages at the beach can be influenced by wind direction: A numerical study. *NCK Days 2021*, the Netherlands, Online Event.

5. **Pourteimouri, P.**, Campmans, G. H. P., Wijnberg, K. M., Hulscher, S. J. M. H. (2021). Quantitative impact of wind direction on airflow patterns and bed morphology around buildings at the beach. *Coastal Dynamics*, the Netherlands, Online Event.

6. **Pourteimouri, P.**, Campmans, G. H. P., Wijnberg, K. M., Hulscher, S. J. M. H. (2021). The impact of buildings' characteristics on airflow patterns and bed morphology at beaches, using CFD modelling. *Coastal Engineering Proceedings (vICCE2020)*, (36v), 4-4, Online Event. https://doi.org/10.9753/icce.v36v.sediment.4

7. **Pourteimouri, P.**, Campmans, G. H. P., Wijnberg, K. M., Hulscher, S. J. M. H. (2019). CFD modeling of airflow over urbanized beaches and the impact of built environment on aeolian sediment transport. *NCK Days 2019*, Enkhuizen, the Netherlands.

8. **Pourteimouri, P.**, Hejazi, K. (2017). Integrated Numerical Modeling of Wave-Porous Structure by Finite Volume Method (FVM). *37th IAHR World Congress*, Kuala Lumpur, Malaysia.

OTHER CONTRIBUTIONS

1. **Pourteimouri, P.** (2020). The impact of buildings at beaches on airflow and aeolian sediment transport patterns across beach-dune topography, using CFD modelling: literature report. CE&M Research Report 2020R-002/WEM-002. University of Twente, Enschede, The Netherlands.

About the author

Paran Pourteimouri was born on October 31st, 1991 in Babol, a city situated in the Mazandaran province of Iran. In 2009, she began her BSc in Civil Engineering at Babol Noshirvani University of Technology, where she successfully earned her degree in 2013. Subsequently, she relocated to Tehran in 2014 to pursue her MSc in Water and Hydraulic Structures at Khajeh Nasir Toosi University of Technology. Paran's MSc research centered on modelling seepage through porous breakwaters using computational fluid dynamics (CFD). In 2017, Paran completed her Master's program as the top-ranked student in her class. In November 2018, Paran relocated to the Netherlands to commence her PhD study in the Water Engineering and Management group at the University of Twente. Her PhD research, which was part of the ShoreScape project, focused on modelling airflow and aeolian sediment transport patterns around buildings with various characteristics, orientation, and positioning at the beach. During her PhD, she made significant contributions to her field, publishing her work in peer-reviewed journals and presenting it at various conferences in the Netherlands, Spain, Sydney, and other online conferences during the COVID pandemic. Additionally, Paran was actively involved in education, mentoring BSc students, supervising MSc students, and leading tutorials and practicals for courses such as fluid mechanics, measurements in fluid mechanics, and hydraulic engineering. Paran is scheduled to defend her thesis on May 26th, 2023. Also, she began working as a Postdoctoral researcher in the SaltiSolutions project, a joint project between the University of Twente and Deltares from May 1st, 2023.